PERIDYNAMIC MODELING AND IMPACT TESTING OF DYNAMIC DAMAGE, FRACTURE, AND FAILURE PROCESS IN FIBER-REINFORCED COMPOSITE MATERIALS

By

Wu Zhou

A DISSERTATION

Submitted to
Michigan State University
in partial fulfillment of the requirements
for the degree of

Mechanical Engineering - Doctor of Philosophy

2018

ABSTRACT

PERIDYNAMIC MODELING AND IMPACT TESTING OF DYNAMIC DAMAGE, FRACTURE, AND FAILURE PROCESS IN FIBER-REINFORCED COMPOSITE MATERIALS

By

Wu Zhou

This study focuses on developing a peridynamics (PD) theory based model for the prediction of impact-induced fracture and failure process in laminated composites, and the impact testing of damage evolution in composites.

First, the 2D bond-based PD method was evaluated for the dynamic fracture process in polymethyl-methacrylate (PMMA) simply supported beams. PMMA Single Edge Notched Bending (SENB) specimens were impacted with a drop-weight machine. The impact fracture process was recorded with a high-speed camera and the images were analyzed with the digital image correlation (DIC) method. The fracture path and crack velocities simulated with PD basically match the experimental results. However, as the peak crack velocity increases, the ratio of the simulated peak velocity over the experimental one also increases. This deviation was confined with the fitted failure criteria for impact fracture in composites with higher peak velocities in the next chapter.

To capture the impact fracture process more accurately and apply it to composites, two major developments have been made to the PD theory-based models. Firstly, a bond-based mesoscale peridynamic model has been developed for orthotropic composite materials. The model defines a continuous in-plane material constant C_θ for orthotropic materials as the mesoscale off-axis modulus in the laminated composite theory. The C_θ

changes continuously from the fiber direction to the transverse direction with an effective orthotropy. This treatment differs from the existing PD composite models which define a micro-modulus C_f for fibers and C_m for matrix. It is more efficient in simulations of large volume of materials. The mesoscale model was calibrated and employed to simulate the in-plane impact-induced fracture patterns in the unidirectional fiber composite beams. Secondly, the simultaneous crack-velocity-related dynamic strain energy release rate was introduced into the PD failure criteria. Besides the final failure of the composites, the fracture process and crack velocity can be predicted more accurately by using the fitted PD model. The simulation was validated with the comparison to the experimental results.

The mesoscale PD model has been extended into three-dimensional for laminated composites. In the model, both the intralayer and interlayer material constants and critical bonds stretch were defined for laminated composites. The PD model was then employed to study the impact damage of the laminated composite plates subjected to out-of-plane impact loading. The matrix and intralayer damage, and the interlayer delamination have been simulated in the composite laminates with different fiber layouts.

To improve the impact resistance, novel composite structures with reinforcement in the through-thickness direction were explored. A previously developed quasi-three-dimensional (Q3D) braiding method was examined. In this work, the Q3D $[0/\pm 60]_4$ carbon fiber composite plates were fabricated. The in-plane tensile and the out-of-plane impact experiments were performed. The results showed that the Q3D composite limited the intra-layer damage and the inter-layer delamination while keeping the competitive in-plane stiffness and strength.

ACKNOWLEDGEMENTS

I would like to thank:

--- My advisor Professor Dahsin Liu for his persistent support, guidance, and advice throughout my Ph.D. research work and life at MSU.

--- My committee members Professor Xinran Xiao, Professor Ronald Averill, and Professor Zhengfang Zhou for all their advice, help, and encouragement during my Ph.D. research.

--- Dr. Danielle Zeng for the funding support from Ford Motors. Thank Dr. Chian-Fong Yen for the funding support from US Army Research Laboratory. Thank ME Department, College of Engineering, and Graduate School MSU for the funding support and their help.

--- My labmates and friends for their help and support in my PD modeling work. They are Miao Wang, Wei Zhang, Yile Hu, Kurt Lundeen, Fang Hou, Danghe Shi, Yi Sun.

--- My labmates and friends for their help and support in my experimental testing, they are: Shutian Yan, Hoa Nguyen, Lingxuan Su, Anthony Wente, Xinyu Mao, Andy VanderKlok, Ben Swanson, Erik Stitt, Suhas, Dr. Tekalur, Todd, Dr. Craig Gunn, Dr. Guojing Li, Daniel Schleh, and Professor Yang Guo.

--- My parents, families, and friends for all their support and encouragement, and thanks as well to everyone else who helped complete this research work.

TABLE OF CONTENTS

LIST OF TABLES

LIST OF FIGURES

KEY TO SYMBOLS

ρ	material density
$\boldsymbol{u}$	displacement
δ	horizon
$\boldsymbol{f}$	pairwise bond force
$\boldsymbol{b}$	body force
$\boldsymbol{\xi}$	relative position between material points
$\boldsymbol{\eta}$	relative displacement
G_{ic}	critical energy release rate
C	micromodulus (material constant) of bonds
C_f	micromodulus (material constant) in fiber direction
C_m	micromodulus (material constant) in all other directions
C_θ	the homogenized continuous material constant
C_1	material constant in the longitudinal (fiber) direction
C_2	material constant in the transverse direction
s	stretch of bonds
s_t	stretch of bonds in a lamina

s_{1t} critical stretch of bonds in fiber direction in a lamina

s_{2t} critical stretch of bonds in the transverse direction in a lamina

s_c compression of bonds in a lamina

s_{1c} critical compression of bonds fiber direction in a lamina

s_{2c} critical compression of bonds in the transverse direction in a lamina

ω micropotential

W strain energy density

W^{PD} strain energy density in peridynamics

W^{CL} strain energy density in continuum mechanics

$\mathrm{d}t$ time step

dV volume of material point

$f_z(t)$ time-dependent body force (loading) added to material point

i index of the current material point

j index of any other material points within the horizon

Chapter 1. Introduction

Fiber-reinforced polymer matrix composite materials are widely used in advanced aircraft and automotive structures due to their excellent mechanical properties, such as high strength to weight ratio, high stiffness to weight ratio, and high fatigue resistance. The composite materials are made by combining light-weight polymeric resin with stiff and strong reinforcing fibers, such as carbon fibers and glass fibers. By combining the two components together, the composite materials can be strong, stiff, and lightweight [1]. In this proposal, the composite materials of interest are laminated fiber-reinforced composite materials. The laminae can be a unidirectional ply or woven fabric ply.

1.1 Fiber-Reinforced Composite Materials

1.1.1 Basic characteristics

The most common form of fiber-reinforced composites for structural applications is the laminated composite [2]. A composite laminate is made by stacking several laminas together while a lamina is a thin ply of made with reinforced fibers and matrix materials. The fibers generally can be unidirectional alignment or woven. The matrix can be ceramics, metal, or polymers. For example, epoxy resins, the commonly used polymer matrix material. The fiber orientation of each lamina and the sequence of different laminas contribute to various functional or structural properties of the laminated composites. Therefore, specific laminated composites can be designed by using different fiber or matrix materials, by fabricating laminates with different orientations of lamina plies [1].

1.1.2 Failure of composites

In this study, we will focus on the dynamic behaviors and failure analysis of laminated composites. Complicated deformation and failure processes occur in composites when they are applied as structural components due to the complex materials constructions of composites. The main failure modes can be divided as follows [3].

1) Delamination -- One of the most common structural failures of laminated composites is delamination. Laminated composites are more of structures than materials. When subjected to out-of-plane loading, due to the bending and transverse shearing, delamination can occur. [4–6].
2) Matrix Failure -- Direct matrix tensile failure occurs when composites are subjected to critical tensile loading [7]. The commonly referred matrix compression failure is associated with the matrix shear failure, which occurs at an angle such as 45° with respect to the compression loading direction.
3) Fiber Failure -- Catastrophic composite failure occurs with a large amount of energy release due to the fiber tensile failure in composites [8]. For compression, when subjected to critical compression loading, fiber kink and buckling can occur in composites [9,10], owing to microfiber bulking and fiber misalignment.
4) Other Failures -- For composites under static loading, matrix creep can occur due to its viscoelastic property [11]. Fatigue damage initiation and fatigue failure can occur when composites are loaded with cyclic forces [12].

1.2 Peridynamic theory

Damage and fracture of composites have been studied experimentally as well as numerically, such as with Finite Element (FE) methods [13–15]. However, the FE method has its limitation in dealing with problems of discontinuity which occurs commonly during damage process because the equation of motion is in a partial differential form of displacement fields. Re-meshing with a prior knowledge of the damage path may be needed for the FE method to study fracture and damage processes [16,17]. Peridynamics (PD), a nonlocal form of continuum mechanics, has been proposed by Silling from Sandia National Lab [18–20]. It is formulated with an integration approach rather than the derivation approach used in continuum mechanics. The PD method can avoid the difficulty of discontinuity when used to study fracture problems.

1.2.1 Bond based peridynamics

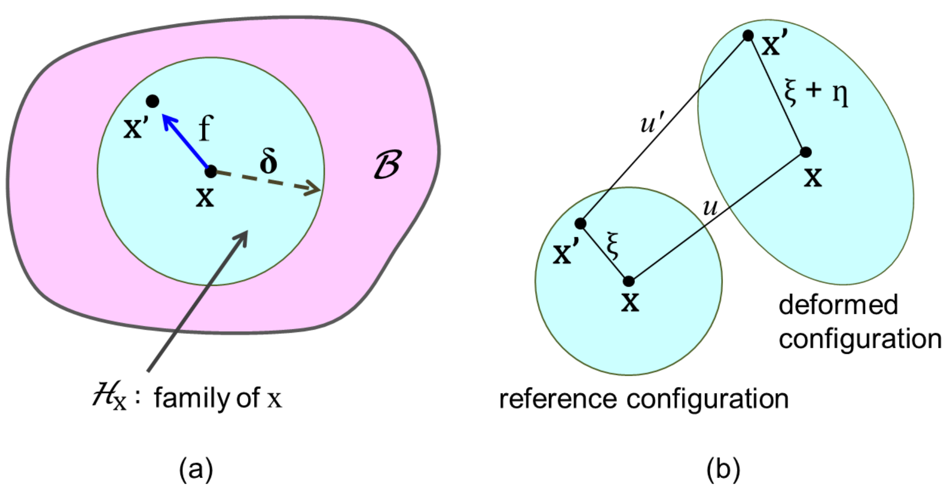

Figure 1.1 Schematic of interaction in peridynamics. (a) Horizon and family. (b) Configuration deformation.

Peridynamic theory defines that in a reference configuration *B*, each material point ***x*** has a subdomain $\mathcal{H}$ with a radius of δ, which is called the material horizon, as shown in Figure 1.1(a). Point ***x*** interacts with all the points ***x'*** in its horizon through the pairwise force ***f***, which has a unit as force per volume squared.

The equation of motion at any time *t* for material point ***x*** can be expressed as shown in Eq. 1-1, where ρ is the density and ***u*** is the displacement. The force density for point ***x*** in peridynamics is an integration of all pairwise forces between ***x*** and ***x'*** in its horizon, which is different from the differentiation in continuum theory. ***b*** is the body force.

$$\rho(\mathbf{x})\ddot{\mathbf{u}}(\mathbf{x},t) = \int_H f(\mathbf{u}(\mathbf{x}',t) - \mathbf{u}(\mathbf{x},t), \mathbf{x}' - \mathbf{x})dV' + \mathbf{b}(\mathbf{x},t) \tag{1-1}$$

The relative position between point ***x*** and ***x'*** is $\boldsymbol{\xi}$, and the relative displacement is $\boldsymbol{\eta}$.

$$\boldsymbol{\eta} = \mathbf{u}' - \mathbf{u} \tag{1-2}$$

$$\begin{aligned} \boldsymbol{\xi} &= \mathbf{x}' - \mathbf{x} \\ \xi &= |\boldsymbol{\xi}| \end{aligned} \tag{1-3}$$

For each bond, the relative elongation is presented as the stretch *s*.

$$s = \frac{|\boldsymbol{\xi} + \boldsymbol{\eta}| - |\boldsymbol{\xi}|}{|\boldsymbol{\xi}|} \tag{1-4}$$

The pairwise force can be defined as

$$\begin{aligned} &\mathbf{f} = \frac{\boldsymbol{\xi} + \boldsymbol{\eta}}{|\boldsymbol{\xi} + \boldsymbol{\eta}|} c \cdot s \\ &|\boldsymbol{\xi}| > \delta \Rightarrow \mathbf{f}(\boldsymbol{\eta}, \boldsymbol{\xi}) = 0, \ \forall \boldsymbol{\eta} \end{aligned} \tag{1-5}$$

where c is the peridynamic micromodulus (material constant) of bonds. For any material point outside the horizon of material point $\boldsymbol{x}$, the pairwise force is zero. The material is defined to be micro elastic if the pairwise force can be derived from a micropotential ω as in Eq. (1-6) below.

$$\mathbf{f}(\boldsymbol{\eta}, \boldsymbol{\xi}) = \frac{\partial \omega(\boldsymbol{\eta}, \boldsymbol{\xi})}{\partial \boldsymbol{\eta}} \tag{1-6}$$

$$\omega(\boldsymbol{\eta}, \xi) = \frac{c\boldsymbol{\eta}^2}{2\xi} = cs^2 \xi / 2 \tag{1-7}$$

$$W = \frac{1}{2} \int \omega(\boldsymbol{\eta}, \xi)\, dV \tag{1-8}$$

Then the micropotential can be further expressed with the formulation containing micromodulus, stretch and relative displacement as shown in Eq. (1-7). The strain energy density in peridynamics can be calculated with integration, as shown in Eq. (1-8). Micromodulus *C* can then be calculated by equating the strain energy density in PD and that from continuum theory.

1.2.2 Damage criteria

Material point ***x*** connects with any other point ***x'*** in its horizon with a PD bond. The bond breaks when bond stretch *s* is over the critical stretch s_0. To describe the connection of a bond, a history-dependent scalar function μ is defined as shown in Eq. (1-9). It equals one when the bond stretch is smaller than the critical stretch, which means the bond still works. Otherwise, the bond is broken and the corresponding bond force becomes zero. Critical stretch can be determined experimentally or theoretically [19].

$$\mu(\boldsymbol{\xi}, s, t) = \begin{cases} 1 & \text{if } s(\boldsymbol{\xi}, t') < s_0 \\ 0 & \text{otherwise} \end{cases} \quad t' \in [0, t] \tag{1-9}$$

$$\phi(\mathbf{x}, t) = 1 - \frac{\int_H \mu(\boldsymbol{\xi}, t) dV'}{\int_H dV'} \tag{1-10}$$

The damage of material point *x* is defined as the function ϕ in Eq. (1-10). If there is no bond broken for point *x* within its horizon, the damage value ϕ equals 0. And when all bonds originally connected to a point are broken, the damage value of the material point is 1, which corresponds to the whole material point being peeled off. A crack is considered to occur when the damage function reaches a value close to 0.5.

1.2.3 Numerical algorithm

In peridynamics, the reference region is uniformly discretized into finite points (material points). Each point has a certain volume in the configuration, as shown in 0.

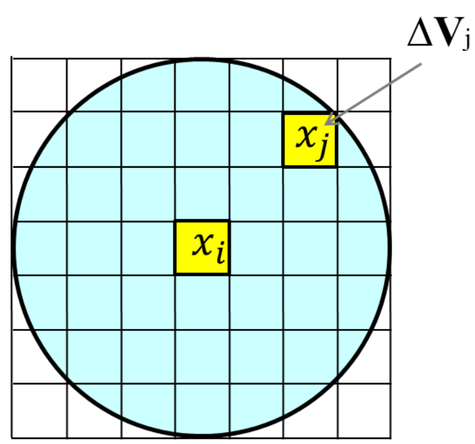

Figure 1.2 Discretization of the horizon for material point x_i.

Then for material point *i*, the equation of motion can be discretized numerically as

$$\rho(\mathbf{x}_i)\ddot{\mathbf{u}}^n(\mathbf{x}_i,t) = \sum_{j=1}^{N} \mathbf{f}(\mathbf{u}^n(\mathbf{x}_j,t) - \mathbf{u}^n(\mathbf{x}_i,t), \mathbf{x}_j - \mathbf{x}_i) dV_j + \mathbf{b}^n(\mathbf{x}_i,t) \tag{1-11}$$

where the subscript *i* is the current point number, *j* is the nonlocal point number within its horizon, and *n* is the integration step number. V_j is the volume of point x_j and is represented by a square lattice area dx^2 for 2D problems when the model is discretized as orthogonal uniform grids. u_i^n is the displacement for point i at the time step n. The displacement for the next time step can be obtained explicitly from the central difference formulations:

$$\ddot{\mathbf{u}}_i^n = \frac{\mathbf{u}_i^{n+1} - 2\mathbf{u}_i^n + \mathbf{u}_i^{n-1}}{\Delta t^2} \tag{1-12}$$

$$\mathbf{u}_i^{n+1} = \frac{\Delta t^2}{\rho}\left(\sum_j \mu_i c_i s_i V_i + \mathbf{b}_i^n\right) + 2\mathbf{u}_i^n - \mathbf{u}_i^{n-1} \tag{1-13}$$

1.3 Scopes of the dissertation

In this work, dynamic damage, fracture, and failure process will be investigated experimentally with impact testing, and numerically with PD modeling and simulation.

The main challenges of this study are:

1) Adjust experimental conditions to simulate specific dynamic conditions of composites encountered in real life. Such as the in-plane impact fracture, and the out-of-plane impact damage in composites structures.
2) Develop an effective constitutive PD model for composites and verify it. Details include building and testing the continuous PD meso-scale material constants for

the lamina, defining the bonds failure criteria in the model, adjusting the numerical integration and its stability etc.

3) Add specific criteria to the PD modeling to capture the dynamic fracture and failure process. For example, the application of instantaneous fracture toughness to the critical bond failure criteria in PD.
4) Extend the lamina PD model to laminated composites PD model. Details include defining the intralaminar and the interlaminar PD material constants and failure criteria for laminates, adjusting the numerical efficiency etc.
5) Design the composite materials with novel fiber layout and woven structures, to explore the composites with high stiffness, high strength, and impact resistance for vehicle light-weighting applications.

1.4 Outline of the dissertation

The dissertation is organized as follows:

Chapter 1 introduces the problem and defines the scope of work.

Chapter 2 provides a literature review on current research about fiber-reinforced composite materials and peridynamics, including the impact damage and failure of laminated composites, the peridynamic modeling of fracture and damage in composites.

Chapter 3 presents a study of the impact loading/energy's influence on the fracture process in the PMMA simply supported beams, analyzes the limitation of the traditional 2D bond-based PD method to capture the dynamic fracture process by simulating the impact fracture. The limination will be confined with the fitted failure criteria for impact fracture in composites with higher peak velocities in the following chapter.

Chapter 4 develops a bond-based mesoscale peridynamic model for orthotropic composite materials. The model defines a continuous in-plane material constant C_θ for orthotropic materials as the mesoscale off-axis modulus in the laminated composite theory. The C_θ changes continuously from the fiber direction to the transverse direction with an effective orthotropy. This model differs from the other PD composite models which define a micro-modulus C_f for fibers and C_m for matrix. It is eligible for simulations of large volume of materials. By implementing the crack-velocity-related strain energy release rate into the failure criteria, the dynamic fracture propagation process and crack velocities can be captured more accurately with the model besides the final failure in the unidirectional fiber composite beams.

Chapter 5 extends the mesoscale model into three-dimensional, introduces the intra-layer and the inter-layer material bonds failure criteria. With the impact loading added to the laminated composite, the lamina damage and the delamination process will be simulated with the PD model.

Chapter 6 investigated previously developed quasi-three-dimensional (Q3D) braiding method. Three composite structures were fabricated and tested in comparison. They are the Q3D $\underline{[0/\pm60]}_4$ carbon fiber composite plates, the $[0/\pm60]_4$ laminates made of unidirectional plies (UDL), and the two-dimensional triaxial braided plies $[\underline{0/\pm60}]_4$ (2D3A). The in-plane tensile and the out-of-plane impact experiments were performed combining 3D DIC method. The in-plane properties and the out-of-plane impact-induced intra-layer damage and the inter-layer delamination will be discussed.

Chapter 7 presents the conclusions, contributions of the dissertation and the future work.

Chapter 2. Literature Review

The reliability study and failure prediction of composites are critical issues during their applications, especially under dynamic loading conditions such as impact. The studies of dynamic failure of composites will be reviewed in this chapter. They include in-plane fracture propagation, delamination due to in-plane compression, and delamination resulting from out-of-plane impact.

2.1 In-plane Fracture Propagation

One of the typical failure modes of the composites during the structural application is the in-plane dynamic fracture, which has been widely studied experimentally and numerically.

2.1.1 Experimental Study

The experimental setup of the in-plane dynamic fracture studies is usually designed by adding the uniaxial impact loading to a central or edge notched plate, or by adding an in-plane three-point bending impact on an edge notched laminated beam [21]. The dynamic failure process is dependent not only on the critical strain energy release rate (toughness) of the material but also on the loading rate added and the crack velocity in the specimen.

Shokrieh [22,23] studied the effects of strain rates on properties and fracture of unidirectional glass fiber epoxy composites in the range of 0.001–100 s^{-1} by using a servo-hydraulic testing apparatus. The experimental results show a significant increase in the tensile strength and shear strength by increasing the strain rate. Both unidirectional and quasi-isotropic laminates were investigated with an increasing strength with the loading strain rate.

Another experimental setup to study the dynamic fracture is the there-point-bending impact, besides the uniaxial dynamic loading. Lee and Tippur studied the dynamic fracture propagation in unidirectional graphite/epoxy composites T800/3900-2 [24,25], PETI-5 and IM7/PETI-5 [26,27]. Rectangular composite plate samples with a single-edged notch are loaded with the impact at the center of the top surface, as shown in Figure 2.1. Mode-I or mixed-mode (mode-I and -II) dynamic fractures were observed with the fiber in a different orientation. The deformation fields and the rapid crack growth in fiber-reinforced composites were recorded by using the digital image correlation method and high-speed camera photography. The dynamic fracture toughness values with fiber orientation angles were extracted. There is a good experimental correlation between dynamic toughness and crack-tip velocity histories for samples with fiber orientations in 0°, 15°, and 30°, which means the dynamic toughness is crack-velocity-related in dynamic situations.

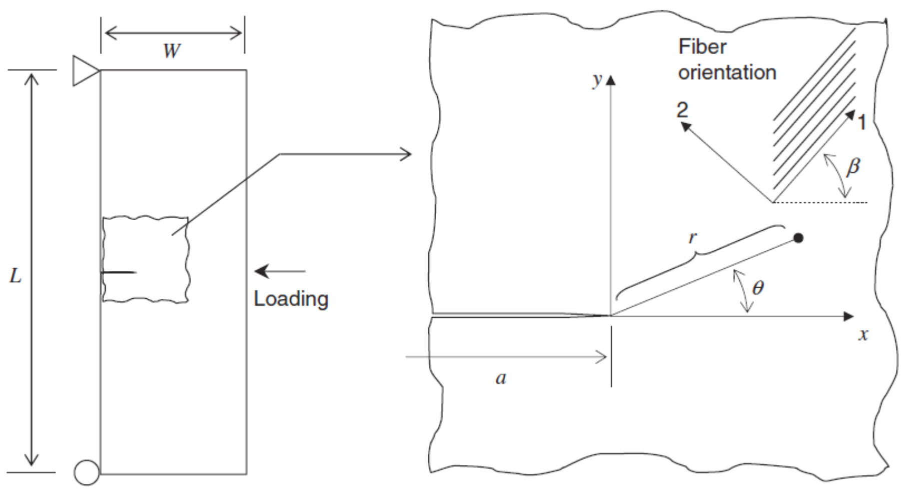

Figure 2.1 Experimental setup of the three-point bending impact [24].

2.1.2 Numerical Modeling and Simulation

FEM and PD methods have been employed to study the in-plane fracture of composites numerically [28,29]. Cahill [30] studied the crack propagation in the linear elastic unidirectional fiber reinforced composites with an enriched finite element method. The results show that the material orientation is the driving factor of crack propagation in the composites, the crack will predominantly propagate along the fiber direction, regardless of the specimen geometry, loading conditions or presence of voids. Pineda and Waas [31] proposed a thermodynamically-based work potential theory for modeling intralaminar progressive damage in laminated composites. The theory was implemented into a FEM for simulating the damage. The method assumes that the material fracture initiates and propagates from the matrix microdamage. By studying the uniaxial tension on the T800/3900-2 panels with a central notch and different fiber orientation and stacking sequences, the very good correlation was achieved quantitatively for global load versus displacement.

Recently peridynamics has been employed for progressive damage in composite materials due to the advantage of the method. Kilic and Madenci [32] investigated a PD model with fiber and matrix in separated material particles and predicted the matrix damage in laminated composites accounting for the inhomogeneous distinct properties of the fiber and matrix. Oterkus et al. [33,34] built the PD model for composites with four material constants in a lamina and predicted the deformation and damage in laminates. Hu and Bobaru [35] proposed a PD model to study dynamic crack propagation by applying the J-integral into PD. However, the application of dynamic fracture toughness into the PD failure criteria has not been investigated yet, which will be investigated in this thesis.

To study the impact compression of laminates under low and high strain rate, constitutive and failure models should firstly be developed [8]. Sun [36,37] developed a rate-dependent nonlinear constitutive model and a dynamic compressive strength model (fiber micro-buckling model) for the unidirectional carbon fiber composite. The model was established based on the low strain rate off-axis test data and it can predict the failure and micro-buckling of the composites in different compression strain rate. An analytical model was developed by Kutlu [38] for simulating the compression response, from initial loading to the final collapse of laminated composites containing multiple through-the-width delaminations. The model is comprised of three parts: a stress analysis, a failure analysis, and a contact analysis. Also, it was inputted into a nonlinear finite element code to simulate the compression on the graphite/epoxy composites. Good agreements were obtained between the predictions and the test data from the initial loading to the final collapse of the specimens. Other FEM modeling and simulations are summarized in the literature [39], the relatively limited and future needed FEM research on laminated composites modeling are summarized as [39]:

1) Material nonlinearity effects on the structural behavior of composite laminates.
2) Failure and damage analysis under viscoelastic effects such as thermal and creep effects.
3) Failure and damage analysis under cyclic loading.
4) Micromechanical approach for damage analysis.
5) Analysis of the damage evolution in composite laminates.

6) Multiscale modeling of crack initiation, propagation, and overall structural failure.

Modeling and simulation of the compressive failure and structure buckling have also been studied limitedly with peridynamics [40–44]. Bond based PD was used by Kilic [40] to investigate the elastic stability of simple structures to determine the buckling characteristics of the peridynamic theory. Also, the bond based PD theory was used to simulate basic compression damage of concrete materials [41,42]. Extended non-ordinary state-based peridynamics was developed with the maximum tensile stress criterion and the Mohr-Coulomb criterion by Wang [43]. The PD model was then used to simulate the crack initiation, propagation, and coalescence in the rocks subjected to compressive loads. For composite materials, only Hu [44] used the developed bond based PD model to simulate the compression behavior.

2.2 Out-of-plane Impact Induced Delamination and Plane Failure

One of the major weaknesses of the composites is the limited transverse strength when subjected to the out-of-plane impact loading such as the bird strike, ballistic impact etc. Complicated deformation and failure occur in composites when subjected to impact loading, especially under different impact energy. The impact force and energy can be very different depending on the impactor's mass, velocity, geometry and loading directions [45,46] etc.

2.2.1 Experimental Study

The experimental studies of the impact on composite materials are usually conducted with the drop-weight and Dynatup machines as shown in Figure 2.2. Different material deformation and failures modes occur when the laminated composites are loaded with different energy of impacts. Under low-velocity impact, plane damage initiates and propagates until delamination happens. The basic damage mechanism resulting from line-loading impact can be summarized as shown in Figure 2.3 by Chang [47,48]:

1) Intra-ply matrix cracks (referred to as the shear or bending matrix cracks) are the initial damage mode.
2) Delamination initiates from these matrix cracks which propagate into the nearby interface with the dissimilar materials.
3) Extensive multiple micro-matrix cracks will be generated along with the delamination propagation.
4) A shear matrix crack located in the inner plies of the laminates will generate a substantial delamination along the bottom interface and a small, confined delamination along the upper interface of the cracked ply.
5) A bending matrix crack located at the surface ply of the laminates will generate a delamination along the first interface of the cracked ply (Figure 2.3).

Topac [49] investigated the damage initiation and growth process during low-velocity impact on $[0_7/90_4]$s and $[90_7/0_4]$s cross-ply CFRP laminates. The two-dimensional damage progression and dynamic strain fields during impact were tracked and recorded by using an ultra-high speed camera and DIC technique.

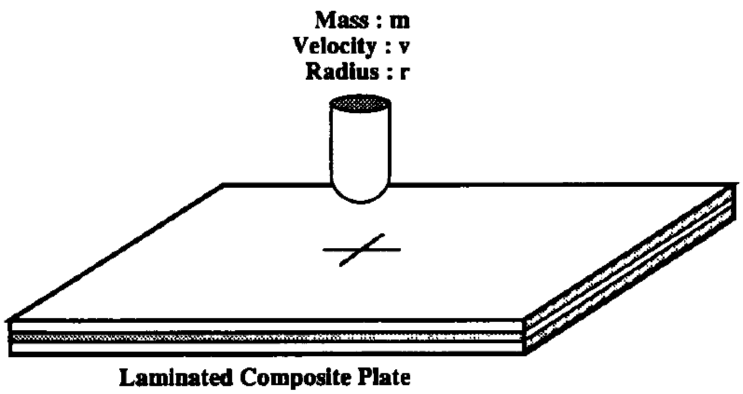

Figure 2.2 A laminated composite panel subjected to transverse impact by a low-velocity impactor [47].

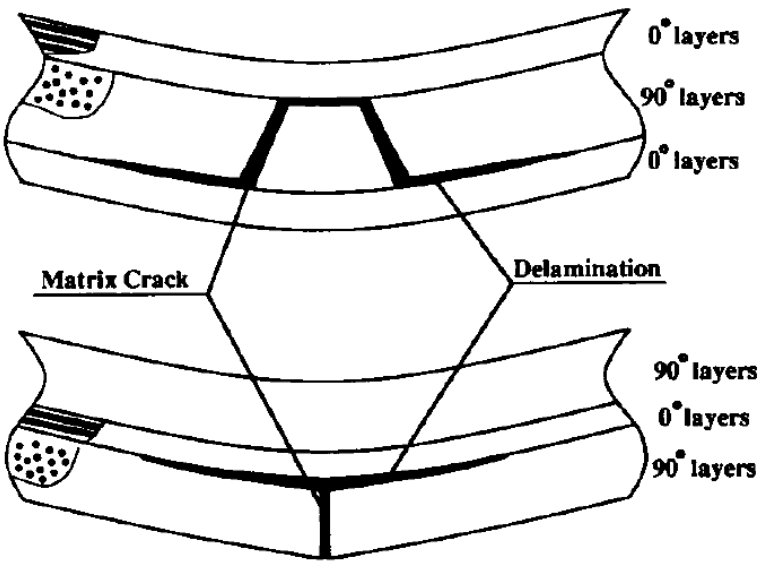

Figure 2.3 A schematic description of two basic Impact damage growth mechanisms of laminated composites. [47]

Three-dimensional studies of the delamination for laminated composites are also investigated experimentally [50–54]. Delamination results from the intra-plane damage propagation or the directly inter-plane shear or open loading [55]. The characterization of three-dimensional delamination can be conducted with the CT scan technique.

2.2.2 Numerical Modeling and Simulation

FEM methods have been employed to study the deformation and failure of composites due to out of impact loading [51,52,56–60]. To simulate the impact failure and delamination with FEM, limitations are summarized as [58]:

1) An interface element is necessary to simulate matrix cracks and delamination.
2) A coupling between the intra and inter-ply damages is needed and information must be exchanged between the interfaces elements of the matrix cracks and delamination.

Peridynamics has been applied to investigate the impact delamination of composites due to the advantage of simultaneous fracture mechanism of the method itself. Xu [61] firstly studied the impact delamination of laminates with PD. The inter-lamina bonds were set the same as the matrix bonds and only stretch bond failure was investigated. The development of proper interlaminar bonds is significant for PD modeling of impact delamination of laminated composites.

Chapter 3. Analyzing the Dynamic Fracture Process in Polymethyl-methacrylate (PMMA) Beams with Three-point-bending Impact Testing and Peridynamic Simulation

3.1 Introduction

Dynamic fracture process in polymethyl-methacrylate (PMMA) beams have been investigated during the three-point-bending impact tests at different impact velocities, conducted in a drop-weight impact tower instrument. The impact-induced crack initiation and propagation have been recorded with a high-speed camera, to determine the instantaneous fracture length and crack velocity during the impact process. The beam deformation and displacement fields were extracted and analyzed by using the digital image correlation (DIC) technique during the impact. The impact loading history has been recorded with a load cell attached to the dropping weight. The whole experimental study is a suitable technique to determine the influence of the impact velocities (impact energy) on the dynamic fracture initiation and propagation at different crack speeds.

Dynamic fracture in structural materials is a significant issue because it concerns the failure of structural materials in their dynamic service. The impact is one of the most common dynamic loading forms but complicated since the material properties and failure behaviors are complex in a dynamic situation. The dynamic fracture problems have been studied experimentally [1–3] and numerically [4,5]. Joudon [1] studied the dynamic stress intensity factor by using a strain gauge method associated with high-speed cinematography on a three-point-bending test with specimens made of M21 epoxy resins. Cramer [2] conducted dynamic fracture experiments using boron-doped silicon single crystals followed by cleavage fracture with the propagation of a faceted crack front with amorphous materials. Owen [3] studied the critical dynamic stress over a range of loading rates of 2024-T3 aluminum sheets ranging in thickness from 1.63-2.54 mm. The dynamic fracture process in three-point-bending beams made with an isotropic polymer [4] and orthotropic composite materials [5] have been numerically simulated with peridynamics.

Fracture in PMMA has also been studied. Takahashi [6] investigated multiple dynamic fracture parameters such as the dynamic stress intensity at the crack tip as well as crack velocity and acceleration. They analyzed the initiation and propagation behavior of the crack of thin PMMA sheet under tensile load. Lataillade [7] studied the mechanical behavior of PMMA under various loading rates as well as the properties of the polymer at high rates of strain. Their research identified the relationship between Young's modulus, yield stress and fracture toughness of PMMA and tensile loading rates. On the other hand, Loya [8] performed a quasi-static three-point bending test on PMMA beams and recorded the crack-front propagation process throughout the specimen thickness. The crack-length and the average steady crack propagation were extracted and studied. In a more recent study, Huang [9] adopted a different technique, dynamic semicircular bend testing, and performed fracture testing on PMMA specimen with a split Hopkinson pressure bar. Their study determined the fracture velocity under different loading rates as well as surface fracture toughness and its relationship with fracture energy.

However, the impact-induced dynamic fracture process in PMMA with a precise record of crack propagation and speed has rarely been studied before, especially the fracture caused by impact with different velocities. In the former studies, the recording time step period is relatively long. For example, only the average crack velocity for the whole fracture can be obtained. To better understand more detail dynamic fracture process, including the beam deformation and crack propagation, the more precise experimental investigation in more precise time steps is essential.

In this chapter, the impact-induced dynamic fracture process in PMMA beams has been investigated. The experiment was conducted with drop-weight tower instruments. During the impact test, the impact loading history has been recorded by a load cell attached to the bottom of the dropping weight. The impact process was recorded with a high-speed camera at the time resolution of about 15 microseconds. The impact-induced crack initiation and propagation have been extracted from the images recorded with the high-speed camera, to determine the instantaneous fracture length and crack velocity during the impact process. The beam deformation and displacement fields were calculated and extracted by using the digital image correlation (DIC) technique. The fracture in beams subjected to different impact velocities has been compared and analyzed.

3.2 Experimental Testing of the Impact Fracture in PMMA Beam

3.2.1 Impact experiment setup

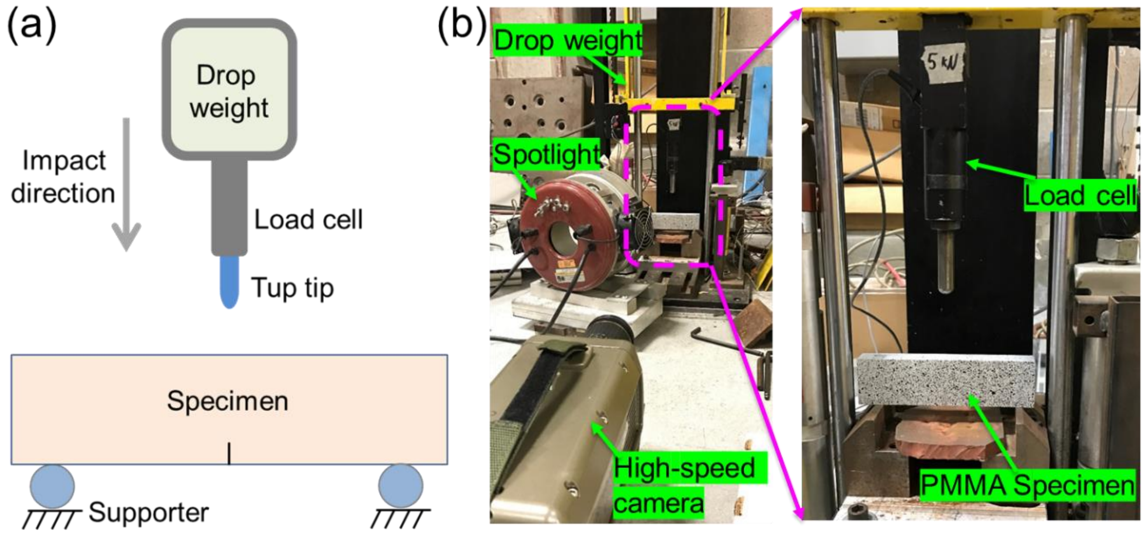

Figure 3.1 Drop weight impact experimental setup. (a) schematic diagram, (b) lab setup.

The experiment was conducted by performing a three-point-bending impact testing on a single-edge-notched PMMA beam specimen by using a drop-weight impact tower as shown in Figure 3.1. Figure 3.1(a) is the schematic diagram of the impact setup, Figure 3.1(b) is the setup in the lab. The drop weight was located above the PMMA sample and set free to drop and impact at the center of the specimen top surface. Two different impact velocities (2 m/s and 3 m/s) were achieved by dropping the weight/impactor from different heights. To monitor the impact force applied to the PMMA beam, a load cell was attached to the bottom of the drop weight to record the loading signals during the impact process. The signals from the load cell were then amplified by an amplifier, displayed and recorded with an electronic oscilloscope provided by National Instruments.

A high-speed camera was placed perpendicular to the vertical surface of the specimen to record the beam deformation and the fracture initiation and propagation during the impact process, as shown in Figure 3.1. The recorded images were used to extract the crack propagation details and the corresponding displacement field contours with the DIC method at different time steps.

The sample beam is made with PMMA (purchased from McMaster-Carr) and prepared with the length of 140 mm, the width of 38 mm, and height of 25.4 mm. A notch of 16 mm was initially cut in the center of the bottom edge of the plate as shown in Figure 3.2. The notch tip was then further scratched with the thinner knife to prepare the original micro crack tip.

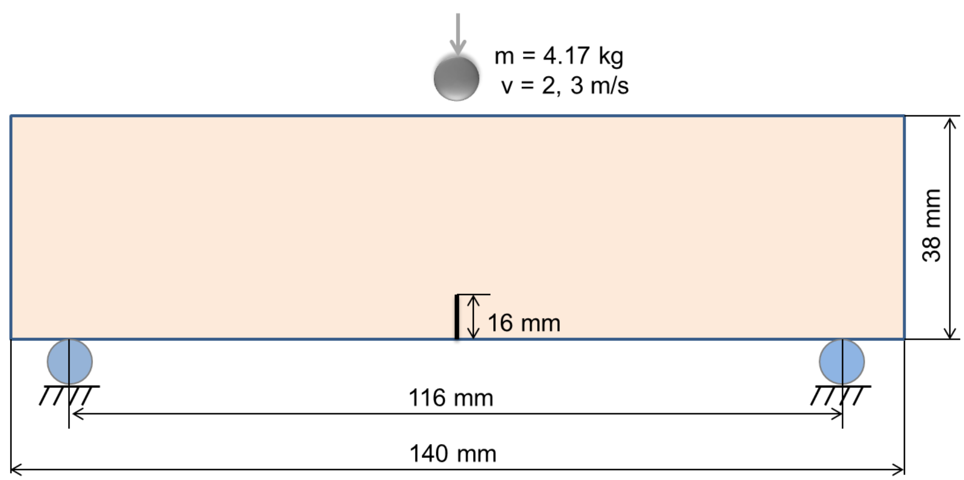

Figure 3.2 Drop weight impact experimental setup.

3.2.2 Impact force on PMMA beam

The impact loadings were extracted from the signals recorded with the load cell. The loading recording resolution was set as 10 μs. The loading history curves of the impact processes with different impact velocities (v = 2, 3 m/s) are presented in Figure 3.3. The loading/force curves initiate from zero before the moment when the impactor (loadcell) contact the top surface of the PMMA specimen. After reaching the peak value, the force then drops suddenly till even negative values, which indicate the loadcell recording of the reflection of the impact stress/strain wave. The peak values of the impact force at different impact velocities are different. The peak force for impact at 3 m/s is larger than that at 2 m/s.

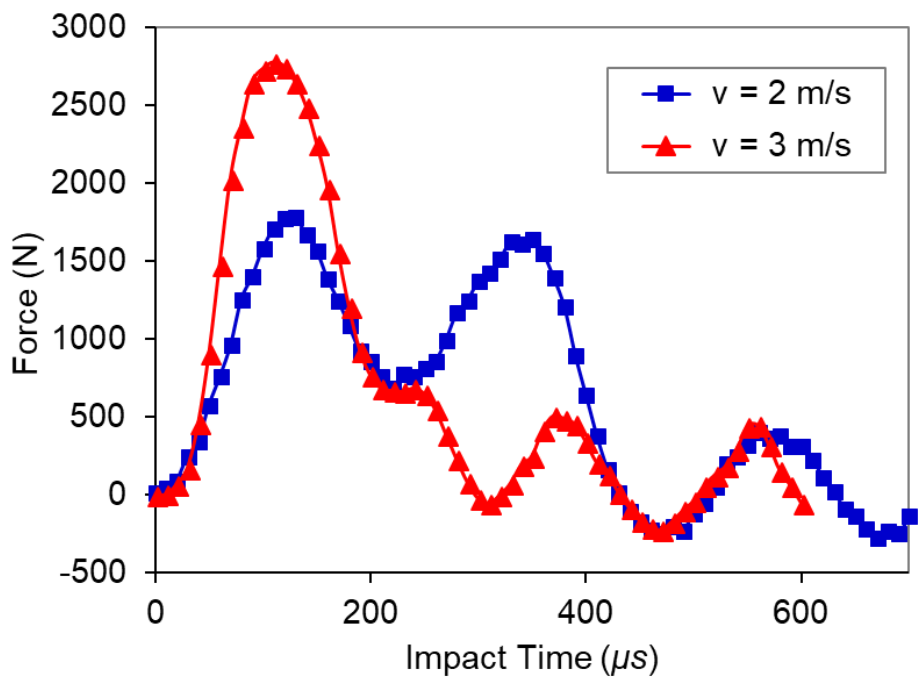

Figure 3.3 Impact Loading history with the impact velocities of 2 m/s and 3 m/s.

3.2.3 Digital image correlation (DIC) analysis setup

The DIC method is an optical method of experimental mechanics that can be used to measure and calculate the displacement, deformation, and strain fields of the specimen surface in mechanical testing [62–64]. The DIC testing preparation steps were set as follows: Firstly, the specimen surface was cleaned and polished to keep smooth. Then the white background painting with evenly located black speckles painting was sprayed on the surface of the specimens. The size of the black painting speckles and the appropriate distances between each speckle can be determined by the suggestions in [65]. A prepared specimen surface is shown in Figure 3.4. The high-speed camera was then set to focus on the crack propagation region on the specimen. The resolution of the camera was 256 x 256 pixels, which correlated to the square area at the center of the specimen. A sequence of images was extracted from the video recorded with the camera, with the time increment of 15 milliseconds. The images were then imported into the software GOM Correlate for the DIC analysis of displacement, deformation fields, and the crack propagation process.

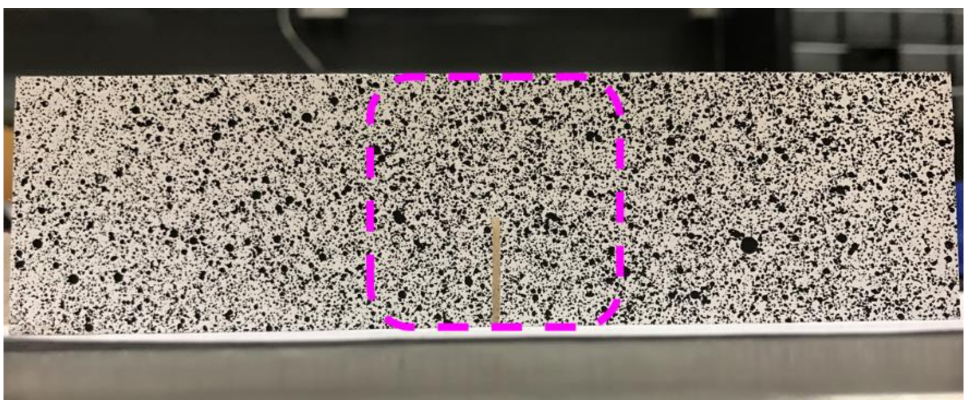

Figure 3.4 PMMA beam surface preparation for DIC

For the DIC analysis with GOM Correlate software, a surface component was created at first. Emphasizing the granularity of the sample, a surface component of 37 pixels was chosen, with a facet offset of 18 pixels. The area of interest was selected by using the Select/Deselect Polygon tool to include the crack propagation region. The original notch tip and the crack tip at each time step can be located in the images with GOM, the absolute crack propagation distances were directly extracted with GOM.

3.2.4 Impact fracture process with displacements fields from DIC analysis

The impact fracture process in PMMA beam with the corresponding displacement fields has been presented in Figure 3.5 and Figure 3.6, with the impact velocities at 2 m/s and 3 m/s respectively.

Figure 3.5 shows the fracture process in PMMA beam with the impact at a velocity of 2 m/s. The fracture initiates at 285 μs after the dropping weight contacts the top surface of the PMMA beam. During that time, the dropping weight subject impact loading at the middle of the top surface of the beam, which causes the beam bending with the increase of the stress concentration at the crack top. The crack propagates from the initiation to 60 μs, till 150 μs, with the crack tip marked with the white arrows. During the fracture process, as the crack length increases, both displacements in x and y directions increase correspondingly. The detail displacement field contour with a color bar is shown in Figure 3.5. Displacements fields are symmetric to the vertical line of the original notch. The change of the color in the displacement contour indicates the deformation process of the beam during the impact process, which lasts during the time period as short as about 150 μs.

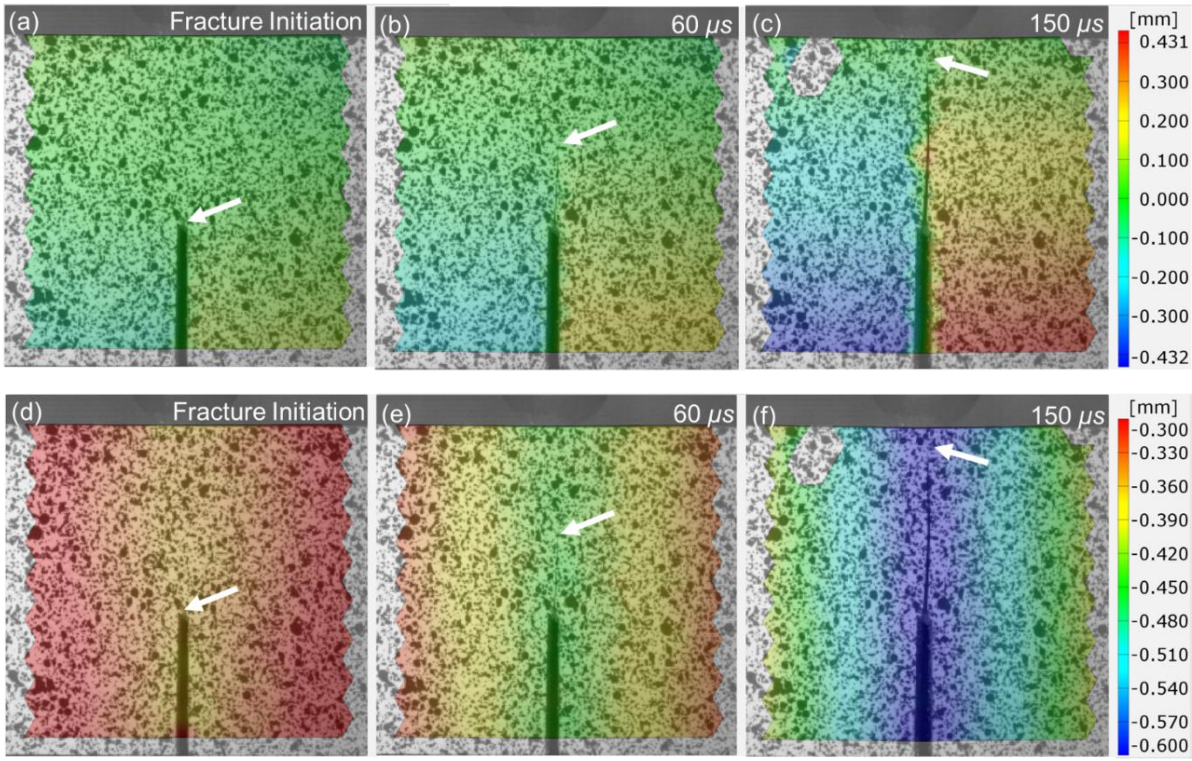

Figure 3.5 Crack initiation and propagation at different time steps, with the corresponding displacement fields (displacements in x-direction: (a), (b), and (c); displacements in y direciton (d),(e), and (f)) in the PMMA beam after the impact at the velocity of 2 m/s. (The crack tips are marked with the white arrows)

Once the dropping weight reaches the top surface of the beam, the beam is subjected to an impact loading and starts to bend due to the simply supported boundary conditions at the bottom surface. During the impact bending process, the tensile stress concentration increases at the tip of the original notch. The crack initiates to propagate once the stress intensity factor reaches the critical value (fracture toughness).

Figure 3.6 shows the fracture process in the PMMA beam with the impact at a velocity of 3 m/s. The fracture initiates at 110 μs after the dropping weight contacts the top surface of the PMMA beam. The crack propagations from the initiation, to 60 μs, till 150 μs, with the crack tip marked with the arrows. Similarly, during the fracture process, the crack length increases, and both the displacements in x and y directions increase correspondingly. The detail displacement field contour with color bars can be found in Figure 3.6. Displacements fields are also symmetric to the vertical line of the original notch. The displacements contours indicate the deformation process of the beam during the impact process, which lasts during the time period as short as round 150 μs too.

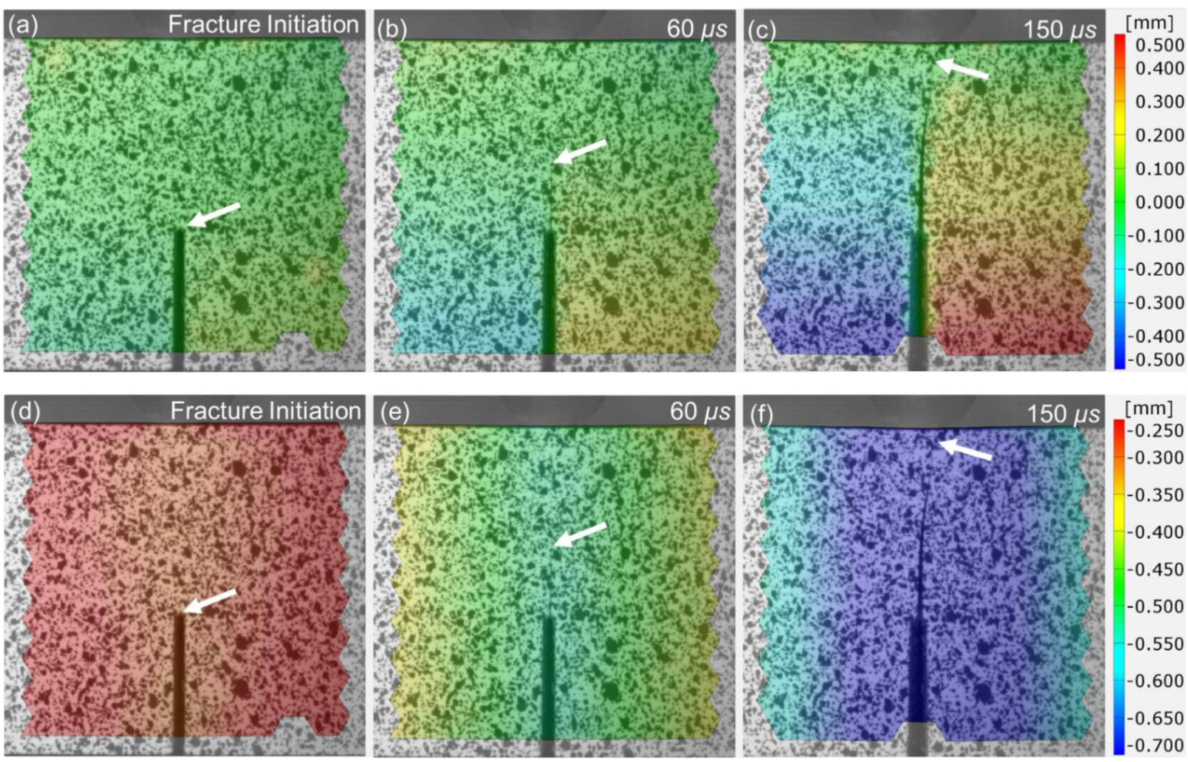

Figure 3.6 Crack initiation and propagation at different time steps, with the corresponding displacement fields (displacements in x-direction: (a), (b), and (c); displacements in y direciton (d),(e), and (f)) in the PMMA beam after the impact at the velocity of 3 m/s. (The crack tips are marked with the white arrows)

The crack initiation and propagation length history in PMMA beams subjected to impact at different impact velocities are shown in Figure 3.7. During the impact process, the time step when the dropping weight contacts the surface of the beam is set as 0. The crack initiation time for PMMA beam subjected to impact at velocities of 2 m/s and 3 m/s are 265 μs and 110 μs, respectively. Obviously, the loading time before the crack initiates is much longer for higher impact velocity, shorter for lower impact velocity. The cracks propagate to 20 *mm* within about 150 μs, but with a different slope of the length curves, which means the crack velocities are different, as shown in Figure 3.8.

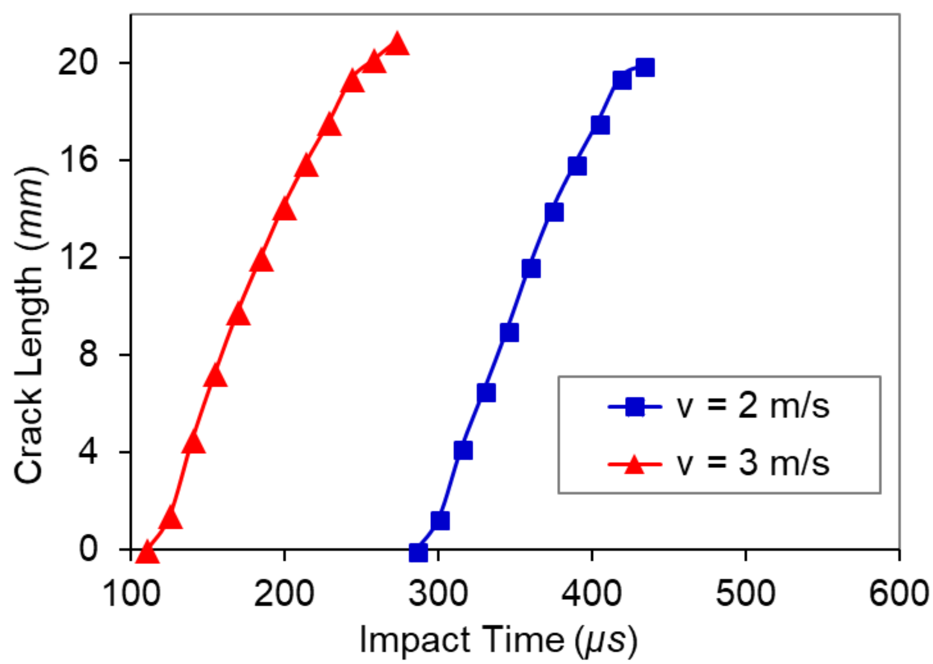

Figure 3.7 Crack initiation and propagation length history in PMMA beams subjected to impact with different impact velocities.

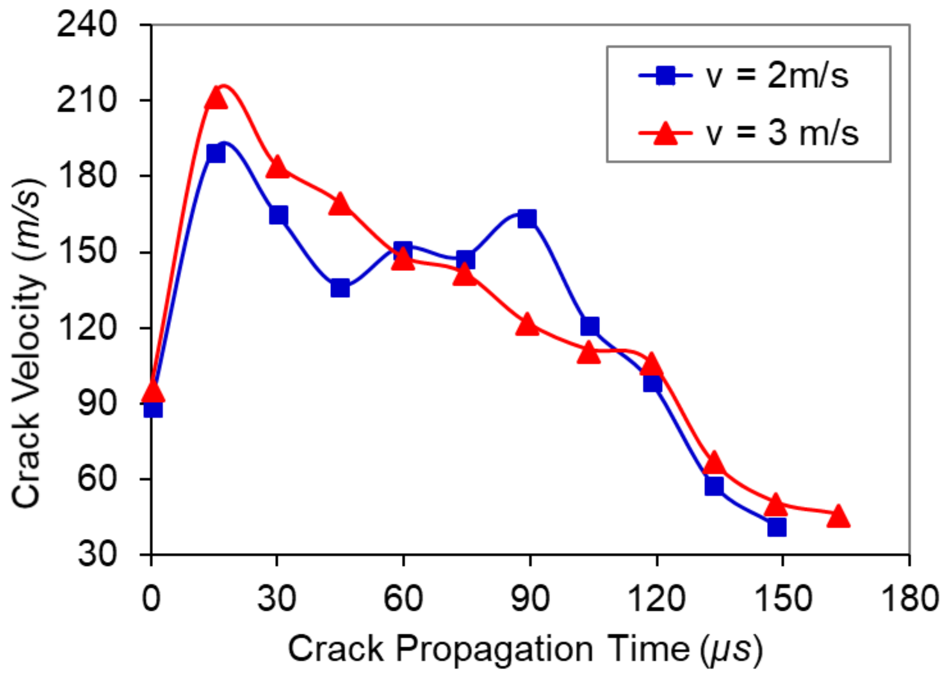

Figure 3.8 Crack speeds after crack initiation in the PMMA beams subjected to impact with different impact velocities.

The crack propagation speeds after crack initiation in PMMA beams subjected to impact with different impact velocities are shown in Figure 3.8, in which the time is set as 0 at the crack initiation point. The crack velocities in beams subjected to different impact loading have the similar trend. Crack velocities start from a relatively lower value around 100 m/s, rise to the peak value around 200 m/s, then decrease till the fracture. The peak crack velocities for fracture in beams subjected to different impact are different. For fracture in the beam under the impact of 3 m/s, the peak crack velocity is highest as 212 m/s. The peak crack velocities in the beam under the impact of 2 m/s are as low as 195 m/s.

To numerically study the impact-induced fracture propagation, peridynamics was employed. The peridynamic simulation of the fracture propagation caused by the different impact energy/velocity is discussed in the coming sections.

3.3 Peridynamic Simulation of the Impact Fracture in the PMMA Beam

The three-point-bending impact-induced fracture process was simulated with the two-dimensional PD method. The experimental results of crack length and crack basically were compared with the PD simulation.

3.3.1 Peridynamic simulation settings

The details about the peridynamics method derivation and the material damage definition have been stated in the introduction in chapter 1. The PD simulation used for simulating the impact on PMMA beam was the two-dimensional PD method. The 2D material constants *C* and the critical stretch *s* of the material bonds are shown as the equations below [66].

$$\mathrm{C} = \frac{6\mathrm{E}}{\pi\delta^3(1-\upsilon)} \tag{3-1}$$

$$s = \sqrt{\frac{4\pi G_{ic}}{9E\delta}} \tag{3-2}$$

The PMMA beam/plate is discretized into the 280*76 orthogonal PD grids, with a square unit length size of dx = 0.5 *mm*. In the PD simulation, each material point has a certain horizon with the size of δ = 3.2*dx as suggested by Hu [67] and Silling [19]. The time increment (time step) for the explicit integration is specified as dt = 1 x 10^{-7} *s*, which is effective for the simulation in this case. The PMMA beam/plate is simply supported as the boundary conditions. In PD settings, the supported point and the family points in its horizon were set with the displacement and velocity in the *y*-direction with the value 0. The setting of the impact algorithm in PD is stated in the Appendix B. The definition of the original crack/notch and the explicit impact algorithm in this study are described in Appendix C.

3.3.2 Peridynamic simulation results and discussion

The PD simulated crack propagation length changing according to time overall matches well with that recorded from the impact experiments, as shown in Figure 3.9. The comparison of the crack propagation in a beam under the impact at 2 m/s is shown in Figure 3.9(a). For the crack propagation before about 12 mm, the PD simulated curve has the slope as large as that of the experimental curve. After 12 mm, the PD simulated crack curve increases slower (lower crack velocity) than that of the experimental curve. The comparison of the crack propagation in a beam under the impact at 3 m/s is shown in Figure 3.9(b). The comparison of the simulation and the experimental curves are different. For the crack propagation before about 10 mm, the PD simulated curve has the larger slope than that of the experimental curve. After 10 mm, the PD simulated crack curve increases at a similar pace with that of the experimental curve. More details about the crack propagation velocity are discussed in the following sections.

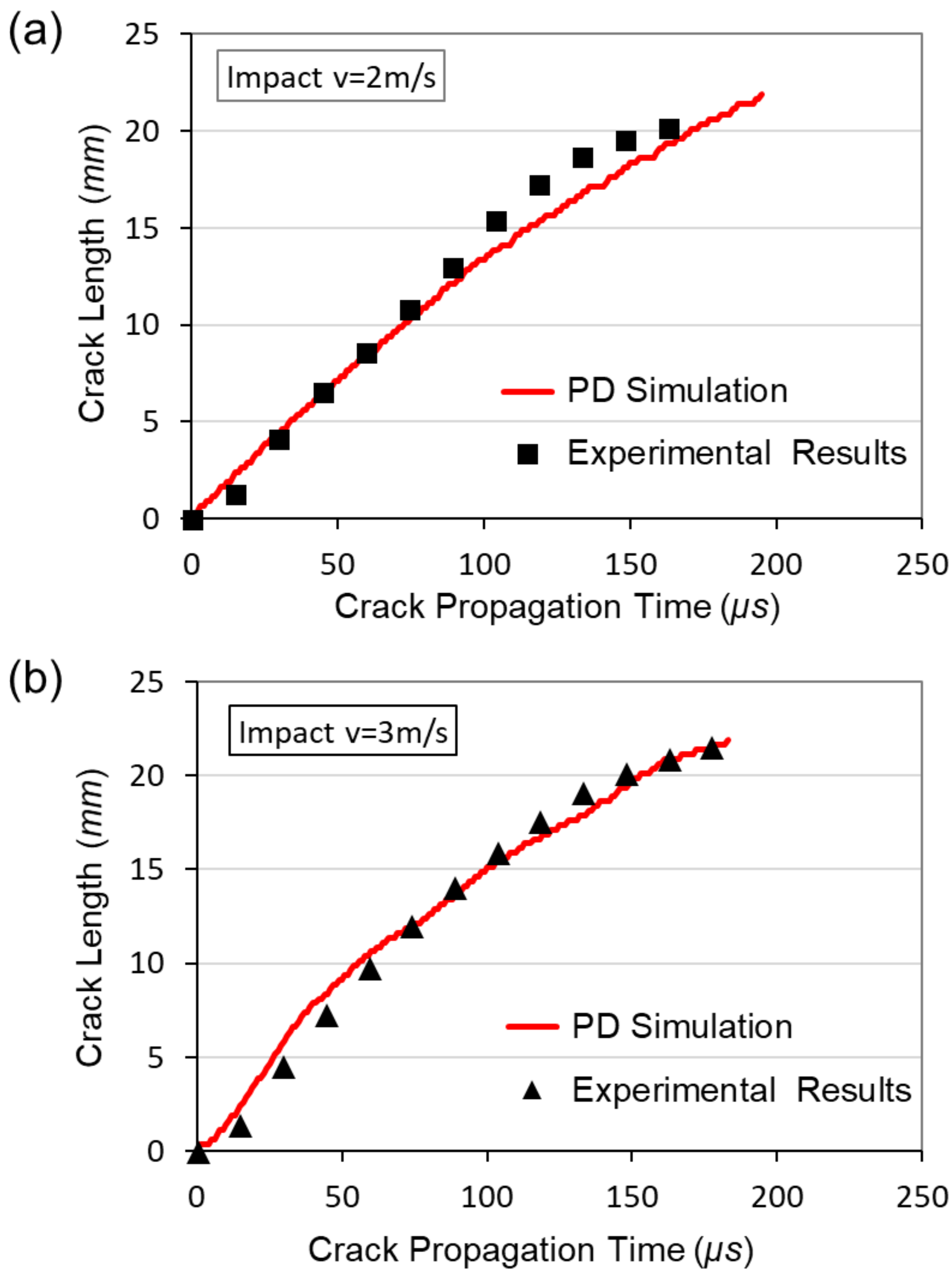

Figure 3.9 Verification of the peridynamic simulation of the crack propagation path.

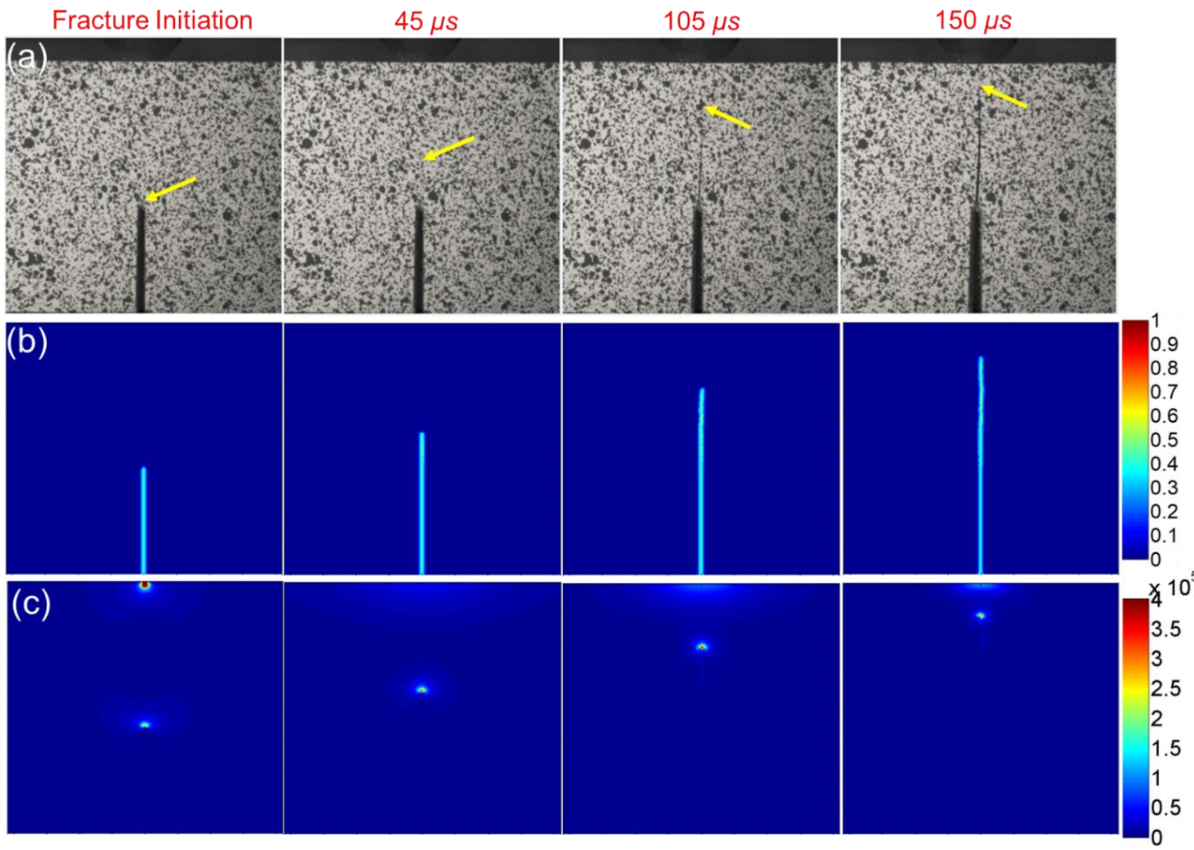

Figure 3.10 Comparison of (a) the experimental observation and (b) the peridynamic simulation of the crack initiation and propagation at different time steps, with (c) the corresponding strain energy density, in the PMMA beam after the impact at the velocity of 2 m/s.

The PD simulation of the fracture propagation processes is shown in the Figure 3.10 and Figure 3.11, which includes: The experimental observation of the impact fracture at the time steps from the fracture initiation, to 45 μs, 105 μs, and 150 μs, (first row), the material damage contours from PD simulation at the corresponding dynamic fracture time steps (second row), and the corresponding PD-simulated strain energy density contours (third row).

The PD simulation of material damage (crack propagation) contours describes the consistent crack propagation process in each beam specimen. The material damage is illustrated as the azure color line in the contours, which has a damage ratio value around 0.4 according to the color bar description. The PD simulation of the crack length matches well with the experimental observation at each time step as shown in the Figure 3.10 and Figure 3.11.

The strain energy density contours demonstrate the corresponding energy distribution status during the crack propagation process. The strain energy density contours are symmetrical due to the symmetrical beam deformation by the crack propagation in the vertical direction. The much higher strain energy density accumulated at the front side of the crack tip, which is considered as the 'driving force' of the crack propagation. In the crack initiation stage, the strain energy density is severely concentrated at both the crack tip and loading areas. As the crack propagates, the less distribution of the energy contour explains that as the crack propagates, the newly generated fracture surface dissipated the strain energy in the sample.

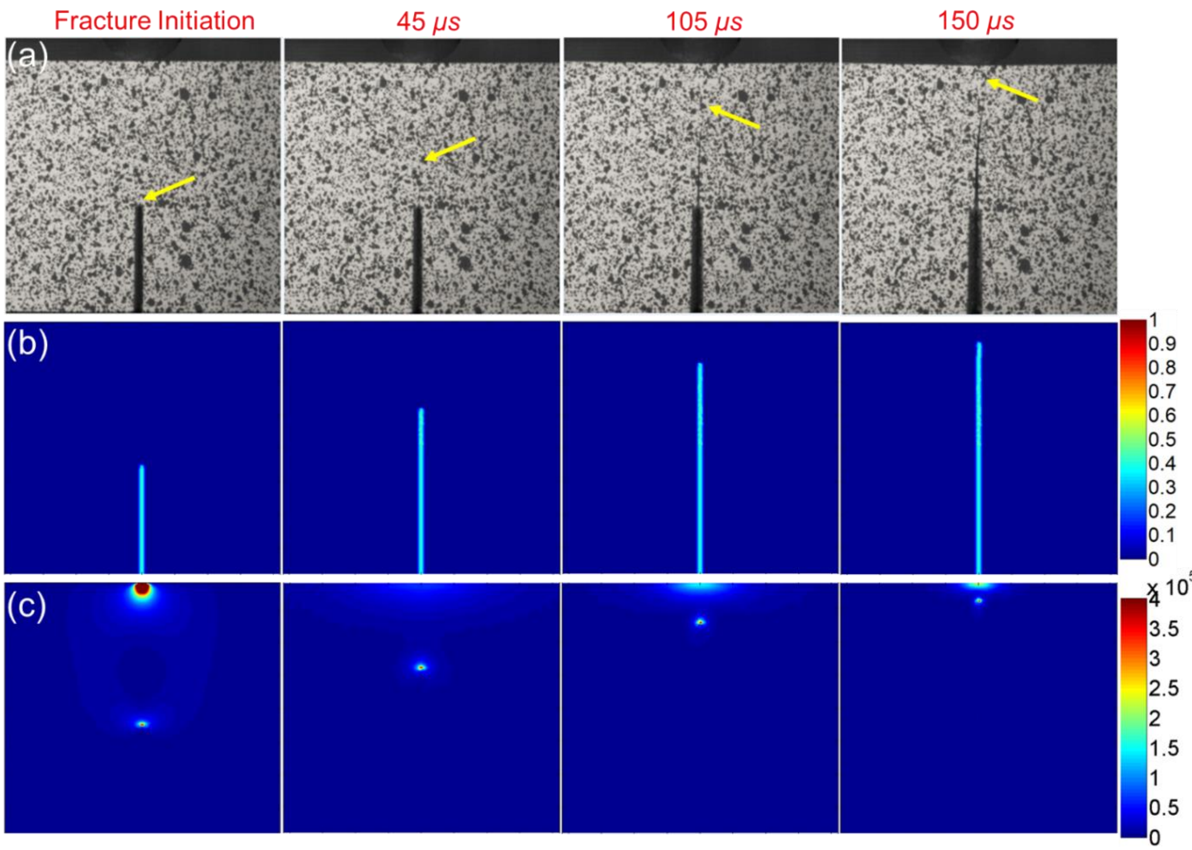

Figure 3.11 Comparison of (a) the experimental observation and (b) the peridynamic simulation of the crack initiation and propagation at different time steps, with (c) the corresponding strain energy density, in the PMMA beam after the impact at the velocity of 3 m/s.

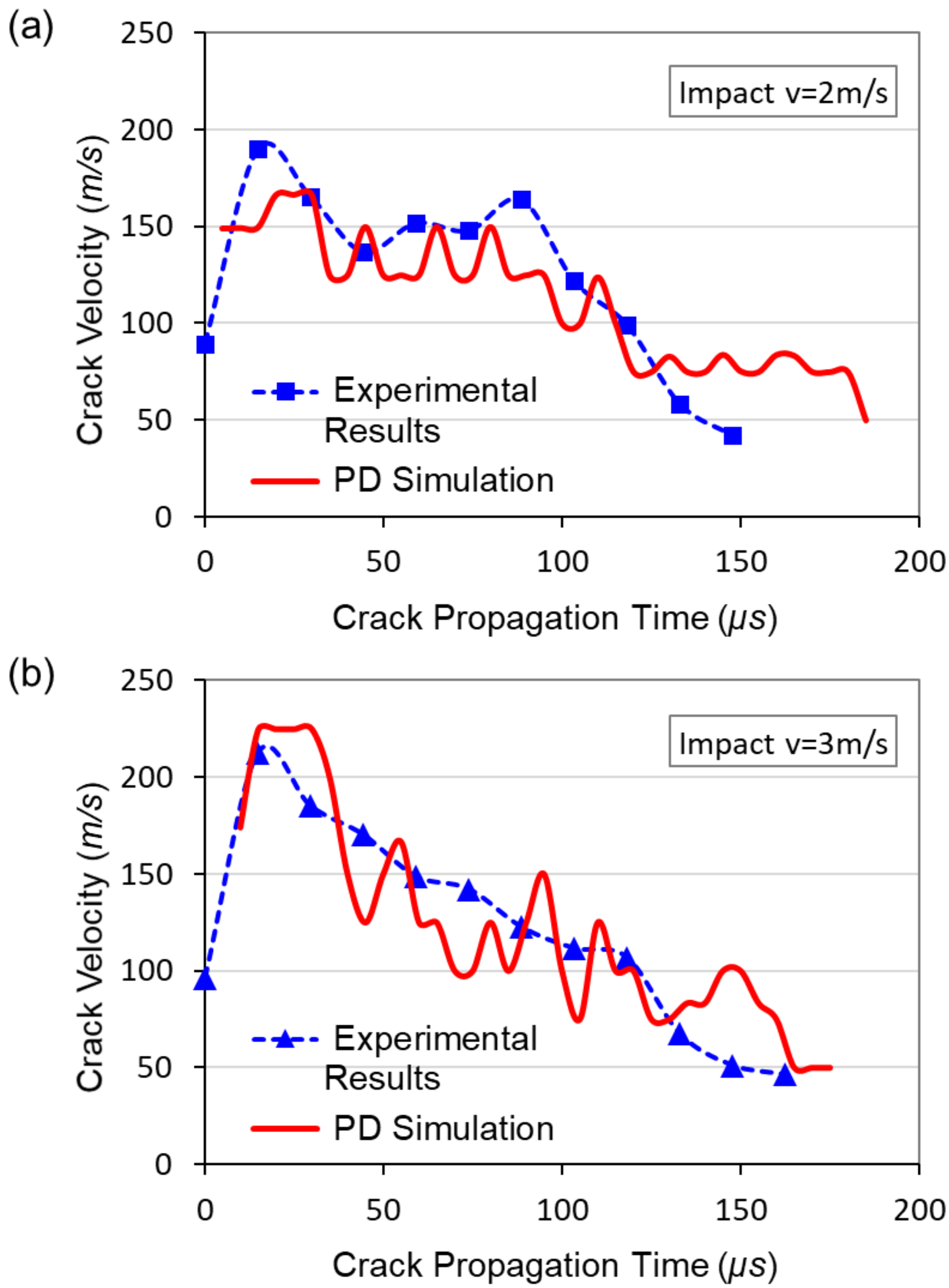

Figure 3.12 Comparison of the experimental observation and the peridynamic simulation of the crack propagation velocity, in the PMMA beam after the impact at the velocity of 2 m/s and 3 m/s.

The comparison of the experimental crack propagation velocity and the PD simulation crack velocity is shown in the Figure 3.12. The PD simulation results match well with the impact experimental results overall. The Figure 3.12(a) describes the fracture in the PMMA beam subjected to the impact at 2 m/s. The figure shows that the PD simulated crack velocity curve has a lower peak value than the experimental crack velocity curve, while the crack velocity changing trends are consistent. The Figure 3.12(b) describes the fracture in the PMMA beam subjected to the impact at 3 m/s. The figure illustrates that the PD simulated crack velocity curve has a slightly higher peak value than the experimental results, and the crack velocity changing trends are the same. The PD simulation of the crack velocity in the PMMA beam under impact at 3 m/s matches better with the experimental results than that for the impact at 2 m/s.

A V_{maxPD} is defined as the peak crack velocity simulated with the bond-based PD method. The V_{maxExp} is defined as the peak crack velocity in the beam measured from the impact experiment. The comparison of the two crack velocity curves indicates that the ratio of V_{maxPD} / V_{maxExp} increases as the V_{maxExp} increases. Both the PD simulated crack velocity curves decrease according to crack propagation time after the peak value. But the decreasing trend speed is different for the two crack velocity curves. The PD-simulated crack velocity curve for impact at 2 m/s decreases slower than that for the impact at 3 m/s. A trend can be concluded from the two crack propagations with different peak velocities: For the impact fracture with higher peak crack velocity, the PD simulated crack velocity curve has a higher ratio of V_{maxPD} / V_{maxExp}, and a bigger absolute curve decreasing slope. More comparable studies of the PD fracture simulation and the fracture experiments need to be conducted to determine whether the trend can be applied to all the impact fracture. For example, the impact fracture with higher peak crack velocity.

Chapter 4. A Peridynamic Model for Fiber-reinforced Composite Materials and Its Capturing the Dynamic Fracture Process in the Composite Beams

4.1 Introduction

To investigate orthotropic materials, two independent material constants have mostly been used to describe the micro-modulus in peridynamics [35,61]. They include C_f in the fiber direction and C_m in all other directions. Based on commonly used composite theories, stiffness/modulus changes continuously with the fiber angle in unidirectional laminae. Hu [67] investigated the quasi-static mechanical performance and damage of laminated composite materials with a peridynamic model. Gahjary [68] proposed a continuous model for orthotropic media with an eighth-ordered sinusoidal function and studied the failure modes of anisotropic materials.

In this Chapter, firstly, a new bond-based peridynamics model has been developed for orthotropic composite materials. The model has a homogenized continuous micromodulus C_θ. C_θ changes continuously from the fiber direction to the transverse direction with an effective orthotropy, compared to the change of Young's modulus in a lamina from the fiber direction to the transverse direction. Secondly, the impact dynamic fracture process has been investigated by inputting the simultaneous dynamic strain energy release rate into the proposed PD model, which has never been studied in former PD studies. The proposed peridynamic model has been employed to study the dynamic crack propagation in an orthotropic beam under impact induced three-point bending. Crack initiation and propagation velocities have been predicted and validated by being compared to the impact experimental results from literature [24].

4.2 Peridynamic model for orthotropic composites

4.2.1 Peridynamic micromodulus of bonds

A two-dimensional peridynamic model has been developed in this paper for a composite lamina. As shown in Figure 4.1(a), any material point i is connected with any other material point j within its horizon δ with a bond. The bond is in an arbitrary direction and has a unique material constant. In the fiber direction (direction 1 as shown in Figure 4.1(a)), bond micromodulus is defined as C_1, and in the transverse direction, the material constant is C_2. For any other bond with an angle θ to the fiber direction, the material constant is defined as a θ dependant C_θ. C_θ changes continuously for bonds orientate from the fiber direction (C_1) to the transverse direction (C_2).

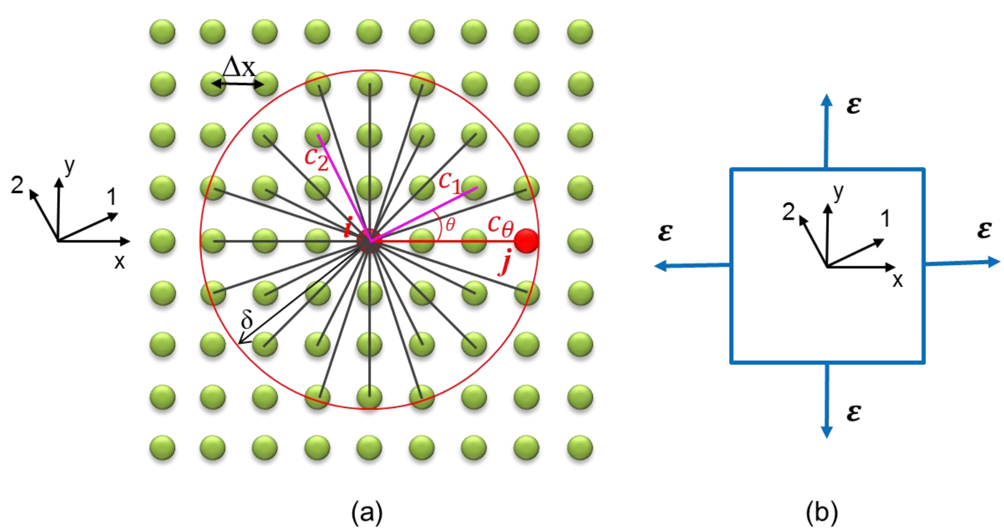

Figure 4.1 Peridynamic model of a lamina. (a) material constants for a lamina, and (b) biaxial loading state.

Two steps are used to calculate the micromodules for the material bond in any direction θ. Firstly, a continuous C_θ/C_2 ratio is defined with an effective orthotropy as a function of the angle θ to fiber orientation. Secondly, the strain energy density from continuum theory is equated with that calculated from PD by inputting the C_θ/C_2 ratio obtained.

When a two-dimensional isotropic media is loaded with biaxial strain ε as shown in Figure 4.1(b), the two-dimensional PD micromodulus can be calculated as described in papers [69,70]. Calculations of strain energy density from continuum theory and PD are shown in Eq. (4-1) and Eq. (4-2), respectively. Micromodulus C can be derived by equating them as shown in Eq. (4-3), where E is the Young's modulus and ν is the Poisson's ratio. In bond-based peridynamics, the material points interact only through a pair-potential, which results in a Poisson's ratio of 1/3 in 2D plane stress and 1/4 in 3D problems for isotropic and linear elastic material [19]. The material constant C is dependent with $E/(1-\nu)$ when being applied for isotropic materials with material properties E and ν. For example, for an isotropic media with Young's modulus E_i and Poisson's ratio ν_{ij}, the corresponsing material constant C_i is dependent with $E_i/\left(1-\nu_{ij}\right)$.

$$W^{CL}=\frac{1}{2}C_{ij}\varepsilon_i\varepsilon_j=\frac{1}{2}(\sigma_{rr}\varepsilon_{rr}+\sigma_{\theta\theta}\varepsilon_{\theta\theta})=\frac{Es^2}{1-\upsilon} \tag{4-1}$$

$$W^{PD}=\frac{1}{2}\int w_b dA=\frac{1}{2}\int_0^{2\pi}\int_0^{\delta}\left[\frac{cs^2\xi}{2}\right]\xi d\xi d\theta=\frac{\mathrm{c}\pi s^2\delta^3}{6} \tag{4-2}$$

$$C = \frac{6E}{\pi\delta^3(1-\upsilon)} \tag{4-3}$$

To present the orthotropy of C_θ in a unidirectional composite lamina, the spherical harmonic expansion of material constant C up to the eighth degree sinusoidal assumption has been used by Ghajary [68]. In this paper, a ratio assumption $R_\theta = C_\theta/C_2$ was directly defined as shown in Eq. (4-4) based on the dependency of PD material constant C and properties $E/(1-\nu)$ in continuum theory. In Eq. (4-4), E_x is the off-axis Young's modulus and ν_{xy} is the corresponding Poisson's ratio. The ratio C_θ/C_2 can be reduced to the constant 1 when bond angle θ is in the transverse to fiber direction, and $E_1(1-\nu_{21})/[E_2(1-\nu_{12})]$ for bonds in the fiber direction, which means C_θ can be directly reduced as C_2 in the transverse direction and it has an effective orthotropy as the direction changes from fiber direction to the tranverse direction. The ratio also indicates that material constant C_θ for bonds in arbitrary directions is dependent on C_2, E_x, and ν_{xy}.

$$\frac{C_\theta}{C_2} = \frac{E_x(1-\upsilon_{21})}{E_2(1-\upsilon_{xy})} \tag{4-4}$$

Different from other definitions of continuous PD material constants for composites [67,68], the material constant C_θ in this study was directly linked with the material propeties E_x and ν_{xy} in continuum mechanics of composite materials. The ratio assumption C_θ/C_2 can be applied to define the change of micromodulus according to different orientations in any materials with the material properties E_x and ν_{xy}, with a very effective material orthotropy. Once the material property distribution of a material is obtained, the ratio assumption C_θ/C_2 can be used to define the coresponding PD micromodulus distributions for further modeling of the material.

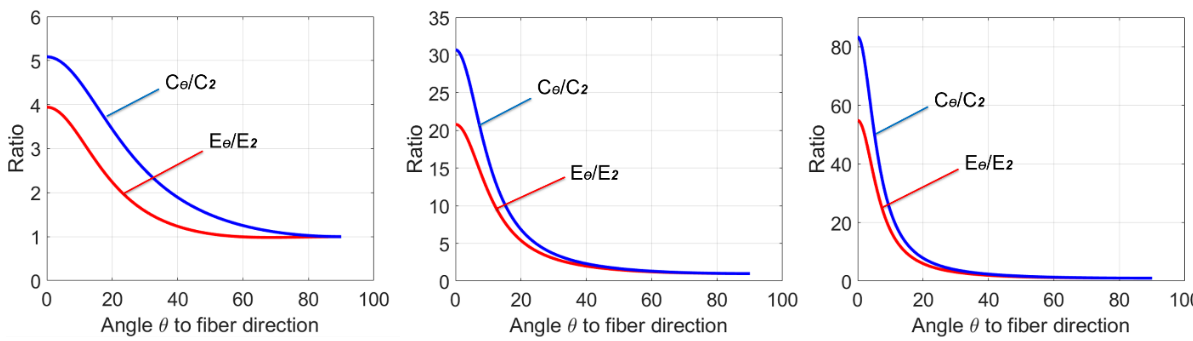

Figure 4.2 Continuous peridynamic constant C_θ has an effective orthotropy for different E_1/E_2 ratios.

The details of continuous micromodulus C_θ for orthotropic materials are described as shown in Figure 4.2. C_θ/C_2 changes continuously from the fiber direction to the transverse direction with a significant orthotropy as the change of off-axis Young's modulus in a lamina from the fiber direction to the transverse direction. Different ratios of off-axis micro modulus C_θ have been compared with the corresponding off-axis Young's modulus E_x/E_2 ranging from 4 to over 50, as shown in Figure 4.2. Moreover, when the model is applied to isotropic materials, the assumption ratio is equal to 1 for bonds in all directions. The corresponding calculated micromodulus can be automatically reduced to a constant C again. The corresponding reduced PD constant is the same as the one stated in the traditional bond-based peridynamics for isotropic materials [18,19].

In the modeling of the composite lamina, once the material constants ratio C_θ/C_2 and the material constant in the transverse direction C_2 is obtained, material constants in all other directions can be obtained by using the ratio in Eq. (4-4). To calculate C_2 and all other material constants, the approach introduced in paper [19] is employed. Suppose a square lamina is loaded with biaxial strain ε_0, the corresponding peridynamic bond stretch s then equals to ε_0. The PD strain energy density is calculated by using Eq. (4-5), where C_θ is described in Figure 4.2 and numerically inputted into the integration. The strain energy density can be calculated from continuum mechanics, as Eq. (4-6). C_2 can then be calculated by equating the strain energy density from peridynamics and continuum theory, as shown in Eq. (4-7), where R_θ is the ratio defined in Eq. (4-4). C_θ for all other bonds in the horizon can be calculated by multiplying the key ratio to C_2.

$$W^{PD} = \frac{1}{2}\int \frac{C_\theta s^2 \xi}{2} dA = \frac{1}{2}\int_0^{2\pi}\int_0^{\delta}\left[\frac{C_\theta s^2 \xi}{2}\right]\xi t \, d\xi \, d\theta \tag{4-5}$$

$$W^{CL} = \frac{1}{2} Q_{mn}\varepsilon_m \varepsilon_n \tag{4-6}$$

$$C_2 = \frac{\sum_{m=1}^{2}\sum_{n=1}^{2} Q_{mn}}{\int \frac{R_\theta \cdot \xi}{2} dA} \tag{4-7}$$

4.2.2 Elastic deformation verification

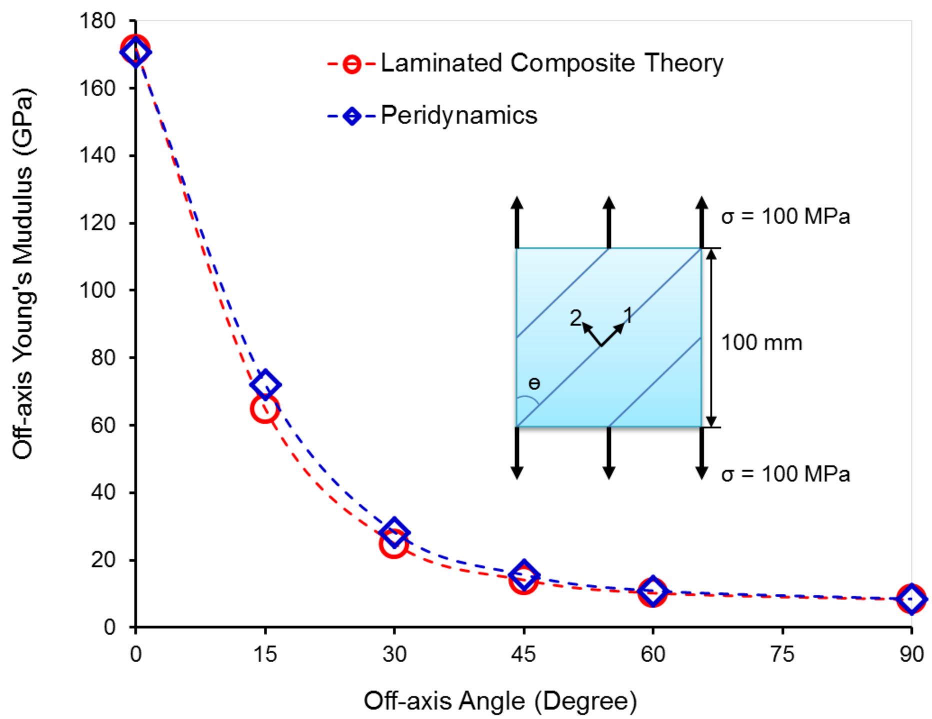

Figure 4.3 Comparison of the off-axis Young's modulus from the PD model and composites theory.

The model is verified by comparing the off-axis Young's modulus calculated from PD and the one from laminated composite theory [71]. A square unidirectional composite plate with fiber in direction θ is loaded with tensile stress on both ends, as shown in Figure 4.3. The plate is made of carbon fiber composite material T800/3900-2. The Young's modulus in the fiber direction and transverse direction are E_{11} = 171.6 *GPa*, E_{22} = 8.25 *GPa*. The shear modulus is G_{12} = 6.21 *GPa* and Poisson's ratio is ν_{12} = 0.344 [24]. The plate is meshed into square grids with a size of 0.5 *mm*, and a horizon δ = 3.2*dx is applied in PD simulation. Comparison of the off-axis Young's modulus calculated from the composite PD model and the one from laminated composite theory is demonstrated in Figure 4.3. The modulus in the fiber direction E_{11} is 170.71 GPa and in the transverse direction E_{22} is 8.46 GPa. The two are almost the same as the provided material properties values. The Young's modulus in other directions is also very close to the value calculated from composite theory as shown in Figure 4.3. The off-axis Young's modulus calculated from the PD model matches well with the one from laminated composite theory [25].

4.2.3 Failure criteria

For the two-dimensional (plane stress) problem, critical stretch can be calculated by equating the work needed to break all the bonds per unit fracture area in PD and the critical strain energy release rate of the material [66]. The 2D formulation [66] is used to calculate critical stretch in this study. For the homogenized peridynamic model of an orthotropic lamina, the bond's failure was defined as the fiber bond's failure and the matrix bond's failure, as shown in Figure 4.4(a) [61]. For bonds in the fiber direction, bonds break if they are stretched over the critical stretch s_1. For bonds in all other directions, the failure is simply set as a matrix material failure. Bonds are defined broken if they are stretched over the critical stretches s_2. The critical stretch s_1 is calculated by equating work required to break all the bonds per unit fracture area in a homogenized media with Young's modulus E_1 and the strain energy release rate G_{ICr}^1 (mode I strain energy release rate for fracture in transverse to fiber direction [31]) for a lamina. Critical stretch s_2 is calculated by equating the corresponding work and the strain energy release rate G_{ICr}^2 (mode I strain energy release rate for fracture in fiber direction [31]). Equations of s_1 and s_2 are presented in Eq. (4-8).

$$s_1 = \sqrt{\frac{4\pi G_{ICr}^1}{9E_1\delta}}, \; s_2 = \sqrt{\frac{4\pi G_{ICr}^2}{9E_2\delta}} \tag{4-8}$$

The damage of a material point in PD is defined as the ratio of broken bonds to all the original bonds of the point. As shown in Figure 4.4(b), material point *i* is connected with bonds to any point *j* in its horizon. Once there is a broken bond for point *i*, it means that material damage occurs. We can define a crack's presence at a material point when the ratio of broken bonds over all original bonds reaches 0.4 ~ 0.5. A crack propagates when the bonds keep breaking along a damaged path [7].

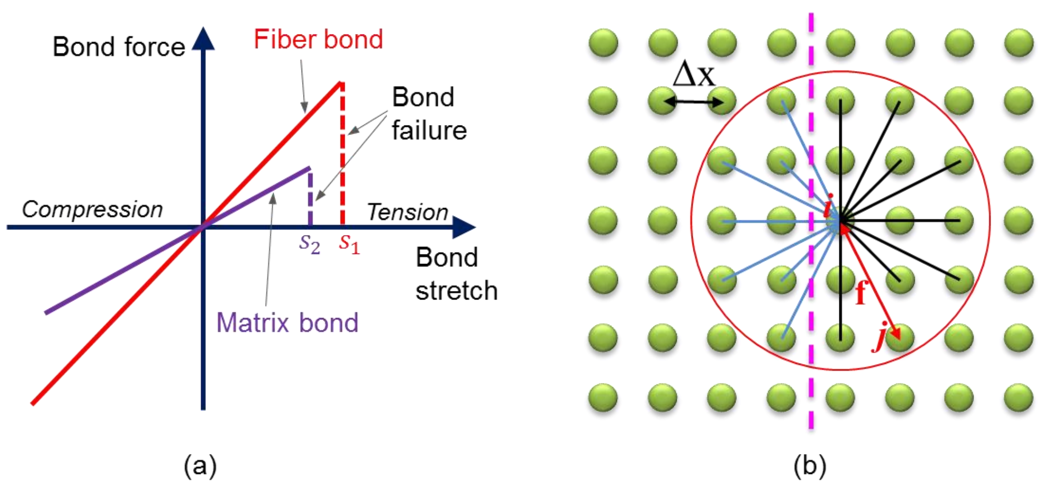

Figure 4.4 Peridynamic failure criteria. (a) Critical stretch of bonds in fiber direction and in matrix direction. (b) Schematic of damage for a material mode *i*.

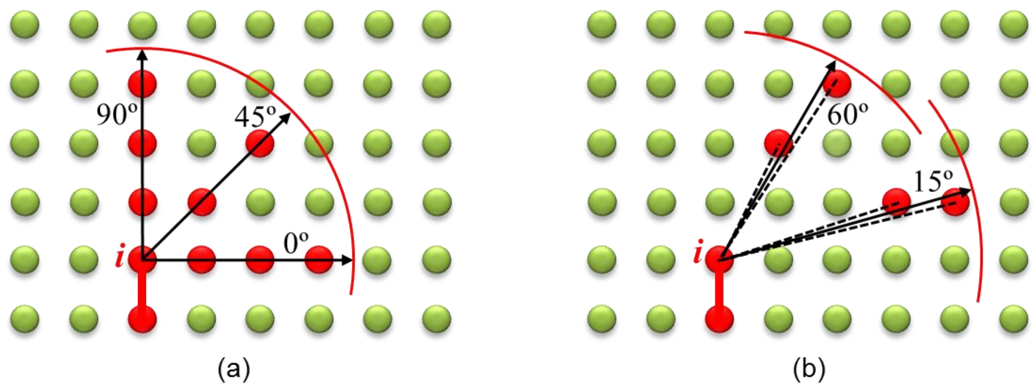

Figure 4.5 Fiber bonds directions in (a) grid-friendly 0º, 45º, and 90º and bonds close to (b) arbitrary directions like 15º and 60º.

For lamina with a fiber in 'grid-friendly' directions 0º, 45º, and 90º as shown in Figure 4.5(a), there are fiber bonds in exactly the fiber direction with the largest value of material constant C_1. During the crack propagation process, these bonds will be much more difficult to break than the bonds in other directions. For lamina with fiber directions in 15º, 30º, 60º and 75º as shown in Figure 4.5(b), not all fiber bonds are in the exact fiber direction. The bonds within a horizon on both sides of the fiber direction are set as fiber bonds. The material constant C_θ for these bonds has a value very close to C_1 because of the continuous micromodulus defined in this model. Therefore, no further defining of fiber bonds is needed once we set the fiber direction and material constant C_θ.

4.3 Problem setup

The developed peridynamic model is employed to study dynamic crack propagation in an orthotropic plate under impact induced three-point bending. The plate is made with carbon fiber composite material T800/3900-2. Its material properties are stated in the verification part in this paper and also in the literature [24]. The plate is 200 *mm* long and

50 *mm* high. It has a fiber orientation of θ (90º, 105º, 120º, and 135º) with respect to the plate length (correspondingly 0º, 15º, 30º, and 45º with respect to the opposite loading direction). A notch of 10 *mm* is initially assigned in the middle of the bottom edge of the plate as shown in Figure 4.6.

The plate is discretized into orthogonal PD grids with a square unit length size of 0.5 *mm*. Grids density among the plate is 100*400. Each material point has a certain horizon with the size of δ = 3.2*dx as suggested by Hu [67] and Silling [19]. The time increment (time step) for the explicit integration is specified as dt = 1 x 10^{-8} *s*, which is sufficiently small in all cases based on the stability conditions analysis in the paper [19]. The lamina plate is simply supported by hinges as shown in Figure 4.6. In PD boundary conditions, the supported point and its family points in its horizon were set with no displacement and velocity in the *y* direction.

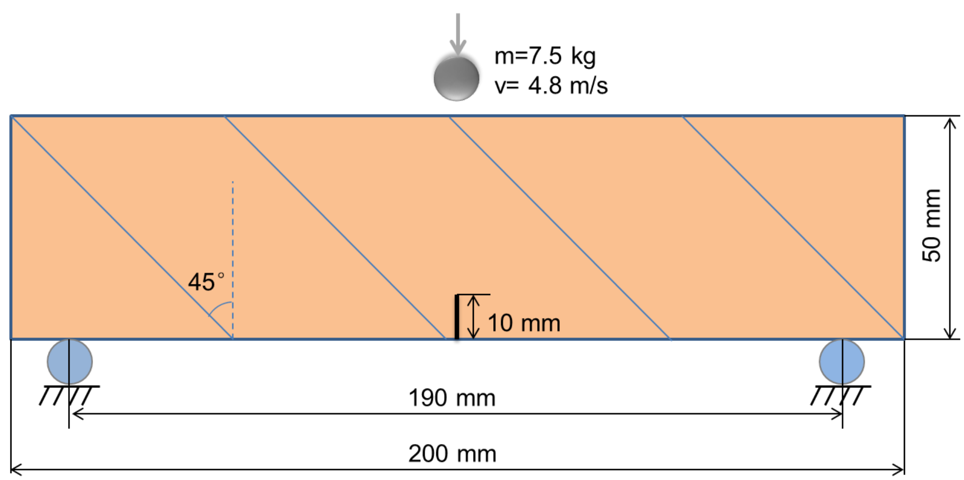

Figure 4.6 Impact experimental setup of SEN orthotropic beam.

The impact algorithm in this study is shown in the Figure B.1 and demonstrated in the Appendix B. Impact loading is added to the middle of the top surface as a boundary condition too. For the impact algorithm in PD simulation, we set a spherical projectile with the same size, mass and a velocity of 4.8 m/s toward the plate, as the setup in the experiments [24]. The impactor is defined as a rigid body due to the hardness disparity between the impactor material and the composite sample. As shown in Figure B.1(a), the impactor moves towards the sample in the beginning. Once the impactor contacts the sample, it penetrates inside and overlaps with the material points as shown in Figure B.1(b). To model the rigid impact, the points are forced to move to the surface of the impactor at the closest path Figure B.1(c). Thus, the contact surface is defined between the impactor and the sample at the current time step. Displacements of points at the sample surface area result in the corresponding bond forces, which interact with the impactor explicitly. Similar impact algorithm is used in the peridynamics as described by Madenci [34].

4.4 Simulation of the Impact Fracture Patterns in Composites with the Model

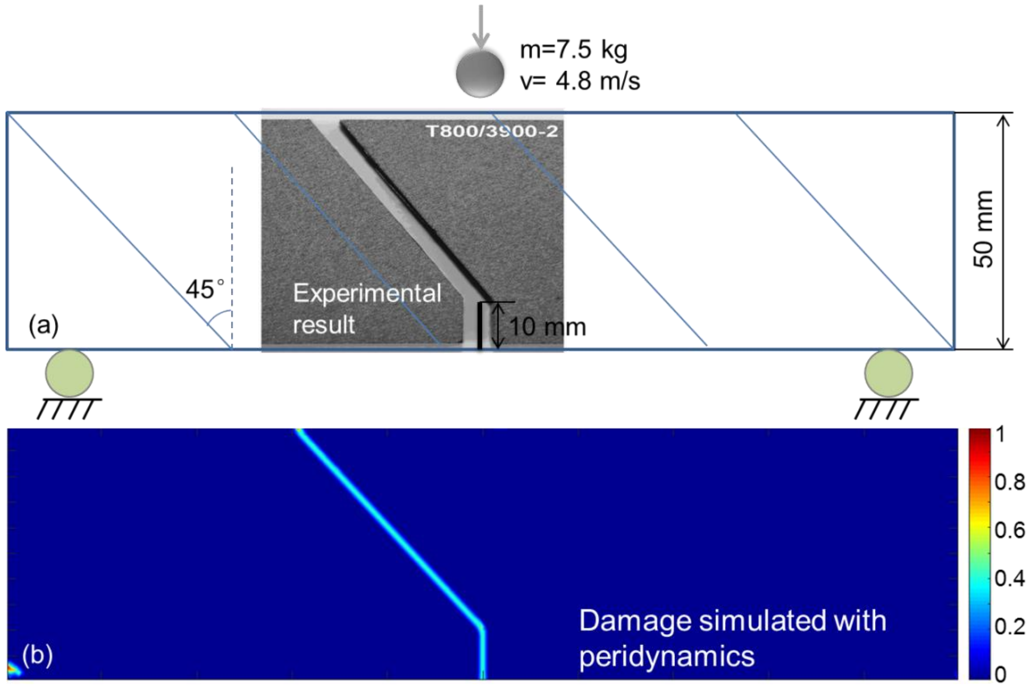

Figure 4.7 Comparison of impact fracture from (a) experimental result [26] and (b) PD computational results.

The impact-induced crack initiation and propagation are simulated by the PD model. For composite material T800/3900, the critical strain energy release rate in the fiber direction is 179.68 KJ/m^2 and in the transverse direction is 0.418 KJ/m^2 [22, 25]. Corresponding critical stretch in PD can then be calculated and applied to the fracture stimulation. The PD simulation result for the impact fracture on a lamina with fiber orientation in 45º is shown in Figure 4.7(b). The result shows that crack (PD material damage) propagates along the fiber direction until the final material failure. The corresponding impact fracture from the experimental results by Lee [26] is shown in Figure 4.7(a). The fracture is also in the fiber direction. The PD fracture simulation result matches well with the impact experimental result.

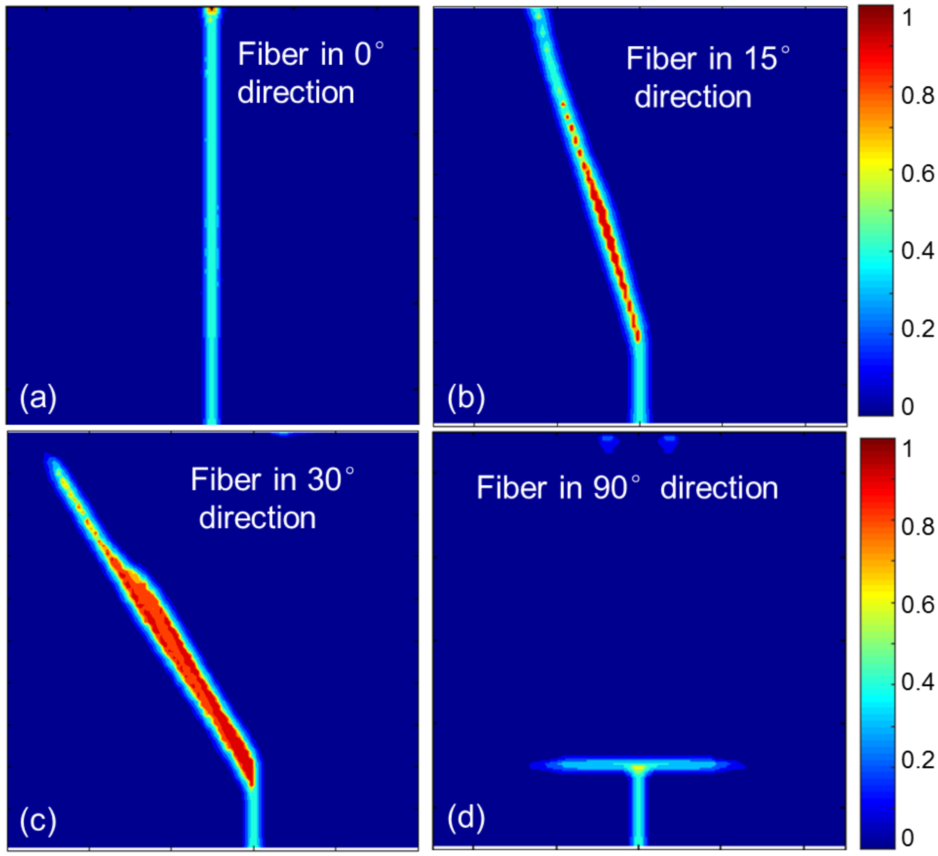

Figure 4.8 Prediction of impact damage in unidirectional lamina with fiber oriented in (a) 0º, (b) 15º, (c) 30º, and (d) 90º with respect to the impact loading direction.

The PD model with a continuous micromodulus has been further applied to simulate the impact fracture on lamina beams with fiber in directions of 0º, 15º, 30º, and 90º with respect to the impact loading direction. The PD fracture simulation results are shown in Figure 4.8. Fracture (material damage) initiates from the tip of the original notch and propagates straight along the fiber directions. The PD crack size depends on the discretized grid size due to the material point damage definition in PD method. But the fracture direction is mesh size independent as the crack propagates along fiber directions.

To obtain a stable result during the computation process, there is a horizon dependent limited maximum stable time step suggested by Silling and Askari [19]. Based on the suggestion, a stable time step dt = 1×10^{-8} *s* has been used in this study, which is suggested as sufficiently small for all PD simulations [19,70]. The surface correction factors [33,34] of a composite lamina can be added to the equation of motion (Eq. 11), resulting in more uniform distributed displacements fields at the boundary corner of the composite plate, but almost the same impact fracture patterns, which can be due to the strong material orthotropy of the unidirectional fiber composites.

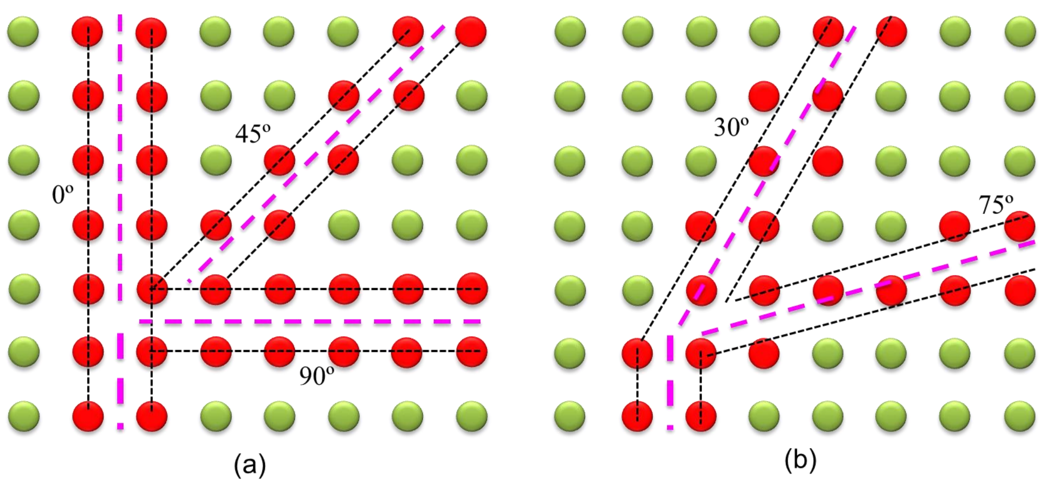

Figure 4.9 Crack propagation patterns in different directions: (a) grid-friendly 0º, 45º, and 90º. (b) Other directions such as 30º and 75º.

For lamina with fiber in 0º, 45º, and 90º directions, the PD fracture propagates straightly along the exact fiber directions. The damage ratio has a consistent value around 0.4 according to the damage contour color bar. However, for lamina with fiber in other arbitrary directions such as in 30º and 15º, the PD fracture path is wider and some of the material points even have a damage ratio value close to 1. This is due to the orthogonal grid pattern of material points that have been used in PD. As shown in Figure 4.9(a), there are cyclic sufficient points aligning in exact 0º, 45º and 90º directions. Once a crack propagates in these ‘grid-friendly’ directions, material points besides the crack have almost the same ratio of broken bonds crossing the crack, which is the damage ratio. However, in other directions like 30º and 75º as shown in Figure 4.9(b), not all material points line up in the exact directions. Points within a range of the fiber directions are defined as the points of fiber directions (Figure 4.9 (b)), which contributes to the wider fracture path pattern in PD in these directions. Moreover, the damage ratios of material points near the crack are not exactly the same. Some material points on the crack path can be almost totally extracted out from the sample after the fracture, which results in a damage value as high as close to 1.

To reduce the mesh grid dependency of the PD fracture pattern in a lamina with any arbitrary fiber direction, the orthogonal mesh grids can be rotated, till the ‘grid-friendly’ direction is aligned with the fiber direction. Therefore, a consistent PD simulated fracture pattern can be obtained for a lamina with arbitrary fiber direction. Or a bigger δ/dx (m ratio) can be used in PD simulation, which means there can be more material points within a horizon, and more possible points can be aligned in the fiber direction. While a bigger delta value brings a more expensive computation, the balance of accuracy and computational efficiency can be made according to specific problems and purpose. More details of reducing crack direction’s dependence on grid orientation by increasing the m-ratio with a uniform grid and further adaptive refinement are discussed in the paper [72].

4.5 PD modeling of the dynamic fracture process

4.5.1 Introducing the dynamic fracture criteria to fit the PD model

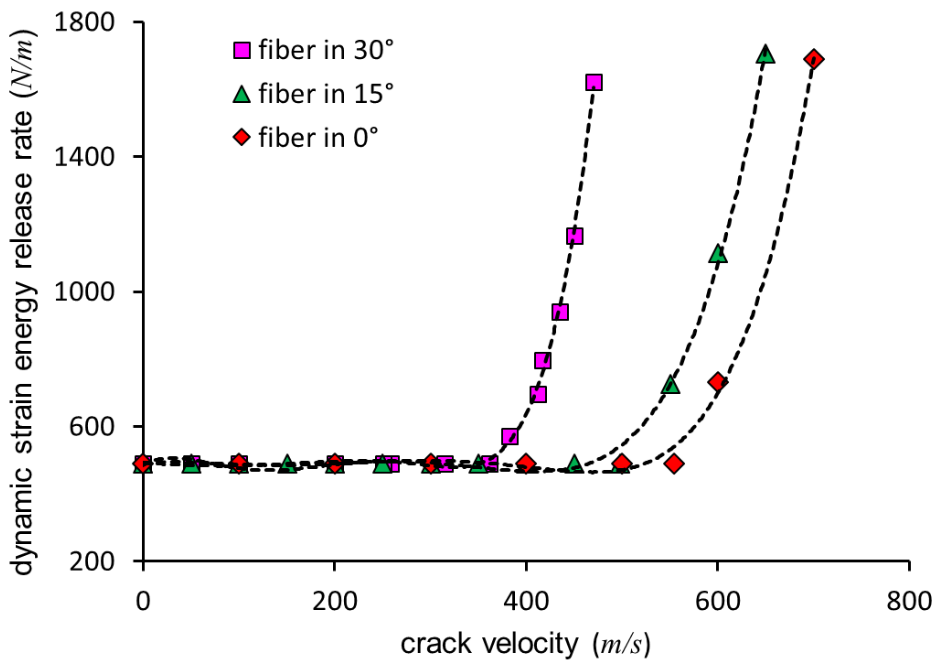

Figure 4.10 Instantaneous dynamics energy release rate versus crack velocity for cracks along fiber orientation in unidirectional composites.

For dynamic fracture problems, the fracture toughness (strain energy release rate) is not constant during the crack propagation process. Especially when the crack velocity reaches a certain high magnitude, the strain energy release rate will increase exponentially to any further increase of crack speed [73,74]. High-order polynomial functions can be extracted from experimental results to describe the instantaneous mode I dynamic strain energy release rate in relation to crack velocity in brittle polymers like PMMA and epoxy [73,74]. Therefore, to simulate the dynamic fracture process in peridynamics, a simultaneous crack velocity related strain energy density should be used rather than a constant one. For a unidirectional composite lamina as studied above, the simultaneous dynamic effective fracture energy [24] can be employed to simulate crack propagation.

To obtain the instantaneous mode I dynamic energy release rate in unidirectional composites with different fiber orientations, the experimental data of the drop weight impact on the unidirectional composite plate [24] can be extracted and extended as polynomial formulations for composites with fibers in different orientations. Based on the experimental results [24], the dynamic energy release rate data are extracted and fitted into polynomial velocity dependent functions as described in Figure 4.10 for lamina with fiber in 0º, 15º, and 30º directions. The strain energy release rate keeps almost constant (quasi-static critical energy release rate) during the relative lower crack velocity stage. As the crack velocity increases to certain critical value, the strain energy release rate increases sharply in accordance with the increasing crack velocity. This trend of dynamic strain energy release rate changing with crack velocity matches well with the experimental studies of isotropic and composite materials [74–76]. The corresponding polynomial functions of dynamic energy release rate for fibers in 0º, 15º, and 30º directions are described in Eq. (4-9, 4-10, and 4-11). Where y is the variable of the simultaneous dynamics fracture energy G_{IDyn}^{m} and x is the variable of crack velocity. The detail curves of these functions are shown in Figure 4.10.

$$y_{0^\circ} = 9.4970\times10^{-11}\cdot x^5 - 1.1164\times10^{-7}\cdot x^4 + 4.3949\times10^{-5}\cdot x^3 - 6.6118\times10^{-3}\cdot x^2 + 0.3000\cdot x + 490.27 \tag{4-9}$$

$$y_{15^\circ} = 8.1331\times10^{-11}\cdot x^5 - 6.7737\times10^{-8}\cdot x^4 + 1.4079\times10^{-5}\cdot x^3 + 3.4729\times10^{-4}\cdot x^2 - 0.2024\cdot x + 492.45 \tag{4-10}$$

$$y_{30^\circ} = 7.3859\times10^{-10}\cdot x^5 - 6.3172\times10^{-7}\cdot x^4 + 1.8708\times10^{-4}\cdot x^3 - 2.2150\times10^{-2}\cdot x^2 + 0.8462\cdot x + 489.75 \tag{4-11}$$

4.5.2 Simulation of the dynamic fracture process with the fitted PD model

The fitted formulations of the simultaneous dynamic strain energy release rate have been applied to PD to simulate the impact crack propagation in a lamina beam with fiber orientated in 0º, 15º, and 30º directions. Crack propagation status at 28 μs after its initiation has been studied by the dynamic PD simulation. The PD simulation results are compared to the experimental Digital Image Correlation (DIC) results [24] to describe the accuracy of the simultaneous PD fracture criteria. Fracture in the composites with fiber in 0º, 15º and 30º is shown in Figure 4.11.

Based on the experimental (DIC) results (first columns of Figure 4.11), crack length in lamina with fiber in 0º, 15º, and 30º are close to 15 *mm*, 12 *mm*, and 9 *mm* respectively. The corresponding PD damage is shown in the second columns of Figure 4.11, which matches the experimental results very well, especially for lamina with fiber in 0º and 15º directions. Based on the experimental dynamic stress intensity factor analysis [24], mode I dominates in the fracture for lamina with fiber in 0º and 15º direction. For lamina with fibers in 30º and 45º directions, the mode I and mode II mixture increases.

Strain energy density from PD simulation is described in the third column of Figure 4.11 correspondingly. For the lamina with fiber in 0º, strain energy is symmetric by the crack in the middle. On both sides of the crack far from the tip, the strain energy density is almost zero, which means the energy has already been released by the newly generated fracture surface. For the part around the crack tip, strain energy is tremendously higher, especially in front of the crack tip; the dark color in contour tells the highest value, which demonstrates there is a high concentration of strain energy density at the crack tip and the crack is driven to propagate at the energy concentration of the material.

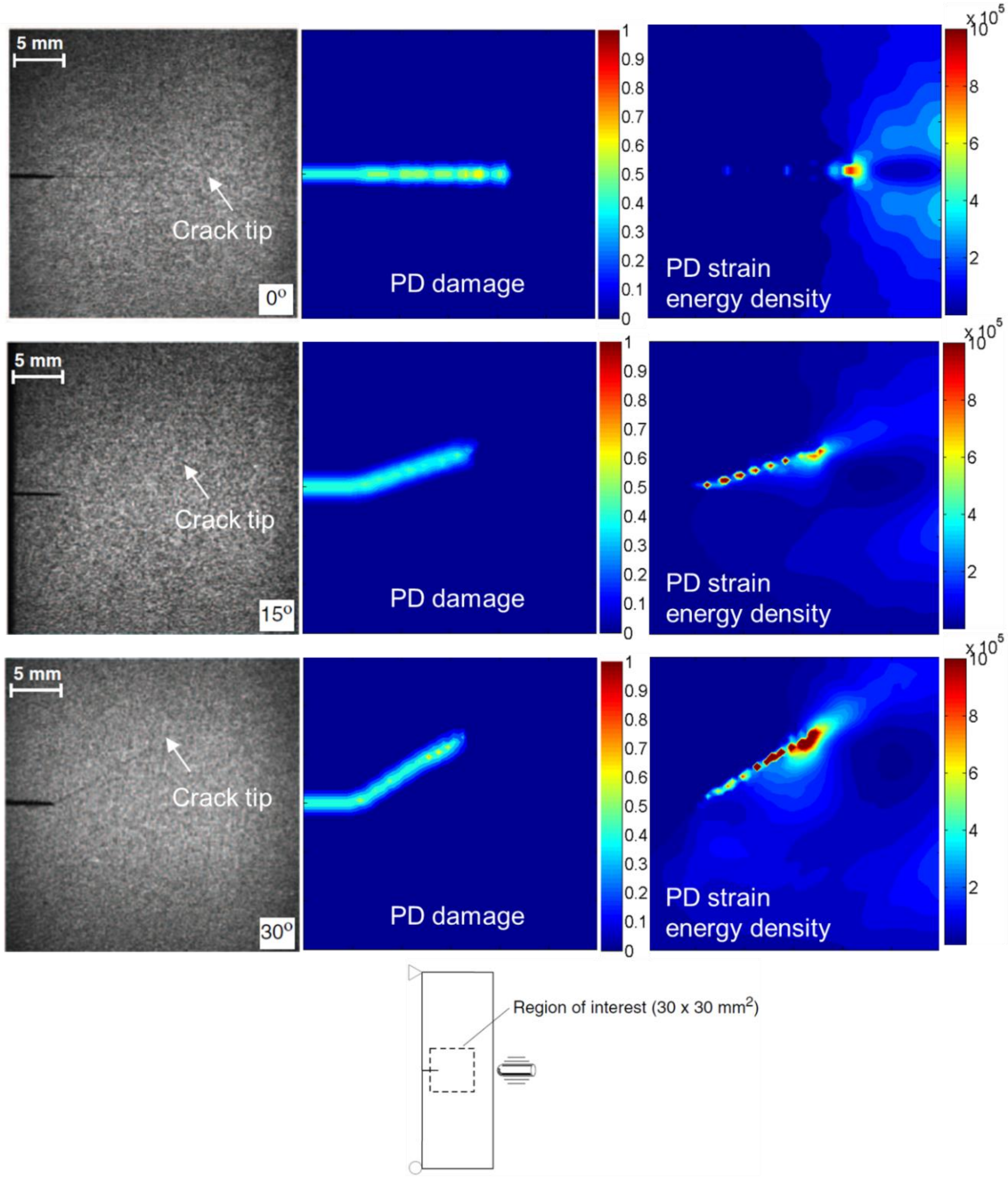

Figure 4.11 Crack in laminae with fibers oriented in 0º (first row), 15º (second row), and 30º (third row) orientations. First column: Experimental results [24]. Second column: The corresponding PD computational damage. Third column: The corresponding PD computational strain energy density.

The same energy concentration is also described in contour for the other three fiber directions. In contours of the lamina with fiber in 15º and 30º directions, the strain energy density on the lower right side of the crack has a higher value than on the up left side. This clearly describes the loading status of the whole beam during impact fracture: bending occurs on the outer side part and it bears almost all the loading from the impact, which causes higher strain energy on this side from the large bending deformation. While on the upper left side of the crack, it is almost a free boundary after the crack propagated, which makes the strain energy density much lower than that on the lower right side. Obviously, the PD simulation can accurately describe the crack propagation length at a certain time and the strain energy density distribution of the beam during the impact process.

Matrix damage in the dynamic fracture process (first row) and the corresponding strain energy density status (second row) in the sample are simulated by using the simultaneous dynamic PD fracture energy. The results are described in Figure 4.12, Figure 4.14 and Figure 4.16, correspondingly for lamina with fiber in 0º, 15º, and 30º directions. The contours accurately describe the consistent crack propagation along the fiber direction in each sample. Results for lamina with fiber in 0º directions is more meticulous than the one in 15º and 30º directions, which is because the PD discretization arrangement of material points is orthogonal. Finer PD mesh grid size or grid orientation can be studied for it.

Strain energy density contours demonstrate the corresponding energy distribution status during the crack propagation process. The extremely high strain energy density at the front of the crack tip is shown clearly in the contours, which describes the ‘driving force’ at the crack tip for the crack propagation. In the crack initiation and early propagation stage, strain energy is highly concentrated and tremendously distributed around both the crack tip and loading areas. As the crack propagates, strain energy distributes less and less all over the sample, which explains that as the crack propagates, more generated new surface from the fracture dissipated the strain energy in the sample. Therefore, the PD strain energy contours can explain the fracture mechanism consistently with fracture mechanics theory.

A comparison of the experimental crack velocities [24] and those calculated from PD is described in Figure 4.13, Figure 4.15, and Figure 4.17, correspondingly for lamina with fiber in 0º, 15º, and 30º with respect to the impact loading direction. For 0º fiber lamina, the velocity calculated from the simultaneous dynamic fracture energy criteria matches the experimental results better than the one calculated from constant fracture energy. The velocity from constant fracture energy is much higher than the experimental velocity starting from the crack initiation, especially at the velocity peak value. However, the velocity from the simultaneous PD fracture energy brings down the higher value and matches with the experimental result very well, especially the big difference at the peak value. Therefore, the simultaneous dynamic fracture criteria is more accurate and effective to simulate the dynamic crack velocity in the impact case than the one using the constant fracture energy criteria in PD. Similar results can be observed in the Figure 4.15 and Figure 4.17 for lamina with fiber in 15º and 30º directions. To investigate the dynamic mixed-mode fracture, further experimental study and the corresponding PD modeling will be conducted.

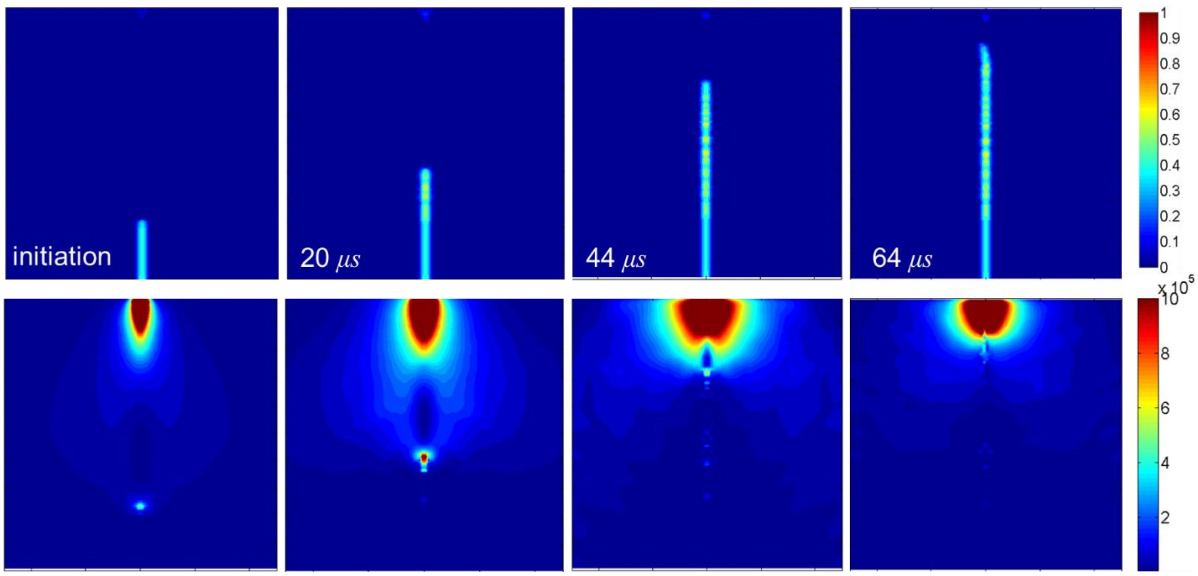

Figure 4.12 Crack propagation process (First row) in the composite beam with fiber in 0º with respect to the loading direction and the corresponding strain energy density (Second row).

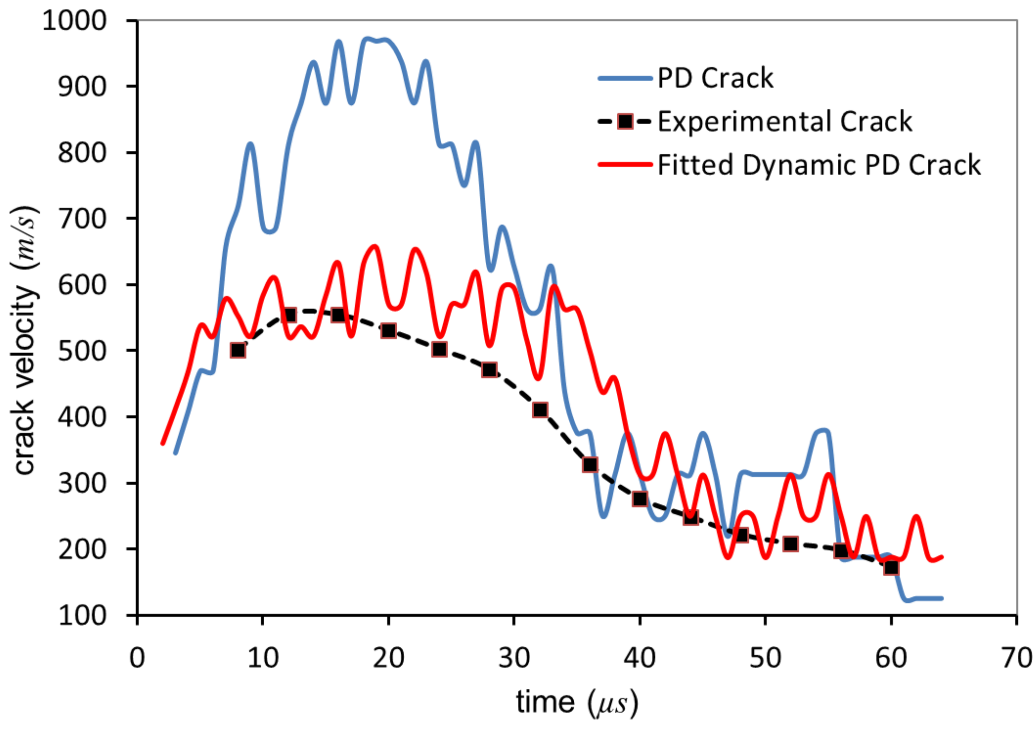

Figure 4.13 Crack velocities in a lamina with fibers in 0º orientation. Comparison of the experimental result [24], PD simulations with ordinary fracture energy and the fitted simultaneous dynamic fracture energy.

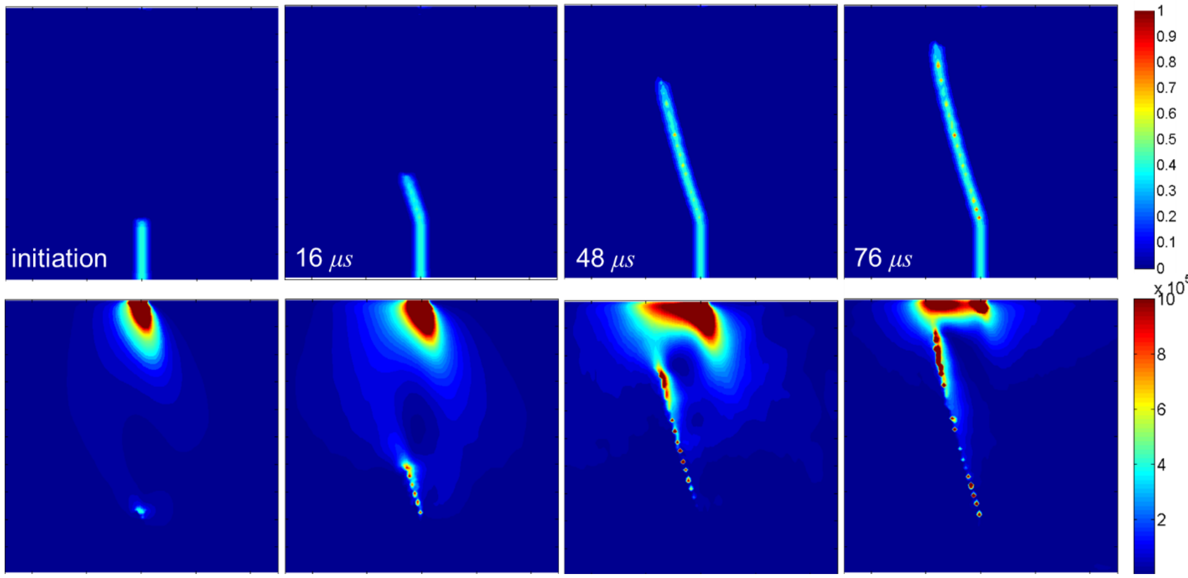

Figure 4.14 Crack propagation process (First row) in the composite beam with fiber in 15º with respect to the loading direction and the corresponding strain energy density (Second row).

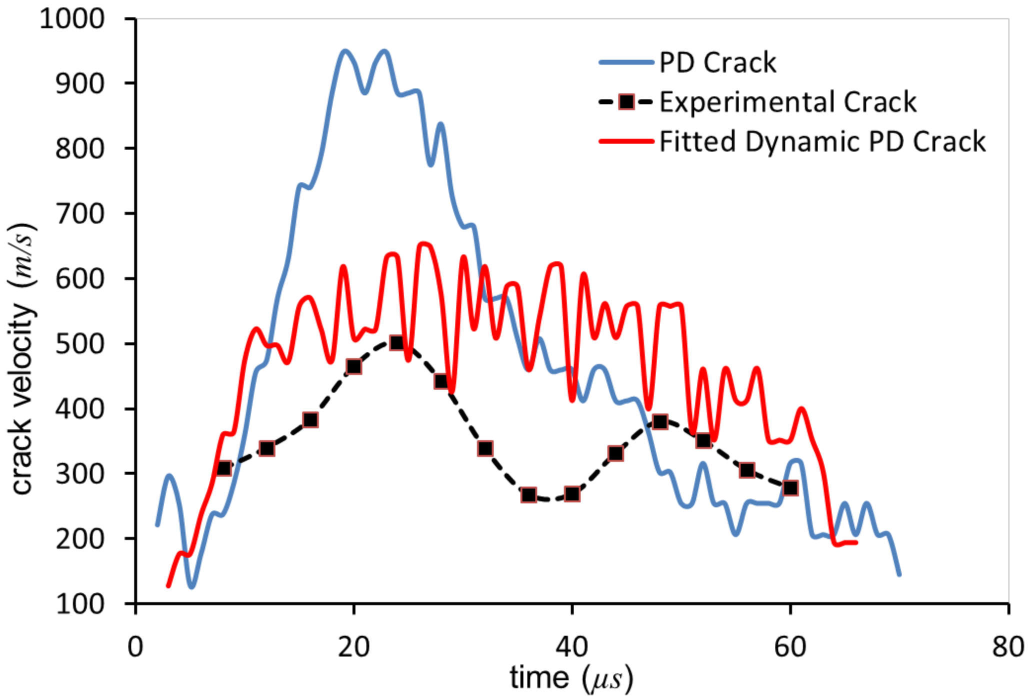

Figure 4.15 Crack velocities in a lamina with fibers in 15º orientation. Comparison of the experimental result [24], PD simulations with ordinary fracture energy and the fitted simultaneous dynamic fracture energy.

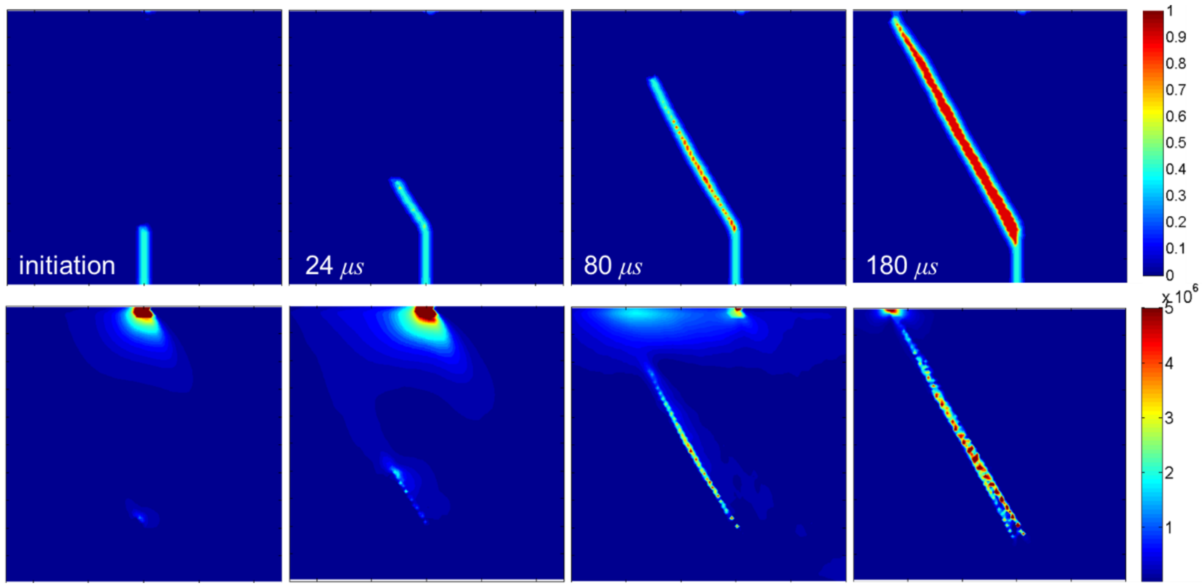

Figure 4.16 Crack propagation process (First row) in the composite beam with fiber in 30º with respect to the loading direction and the corresponding strain energy density (Second row).

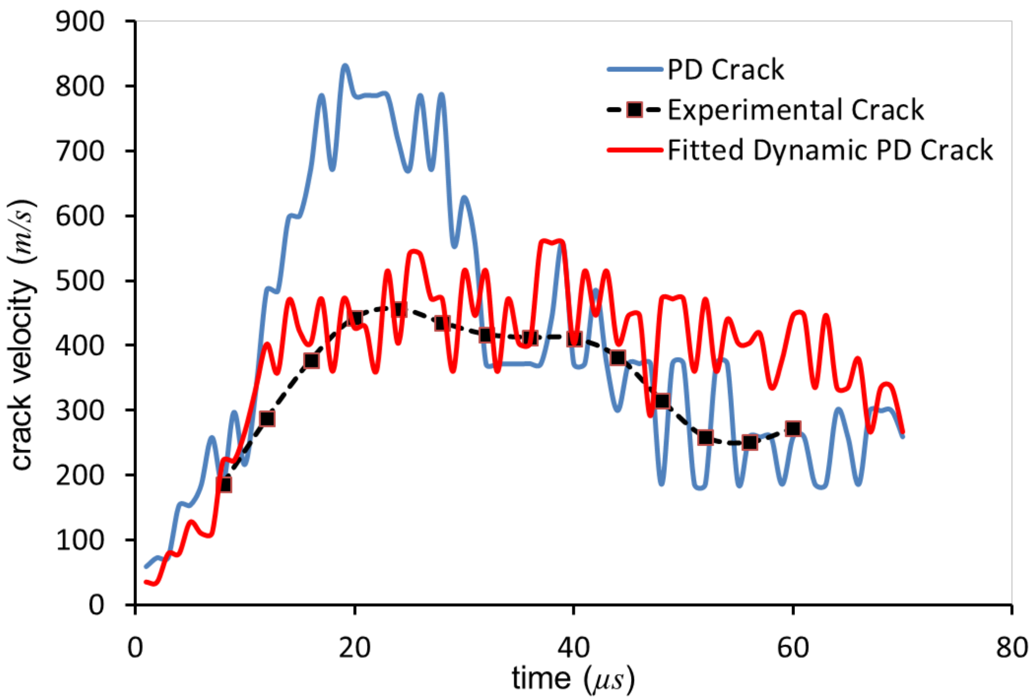

Figure 4.17 Crack velocities in a lamina with fibers in 30º orientation. Comparison of the experimental result [24], PD simulations with ordinary fracture energy and the fitted simultaneous dynamic fracture energy.

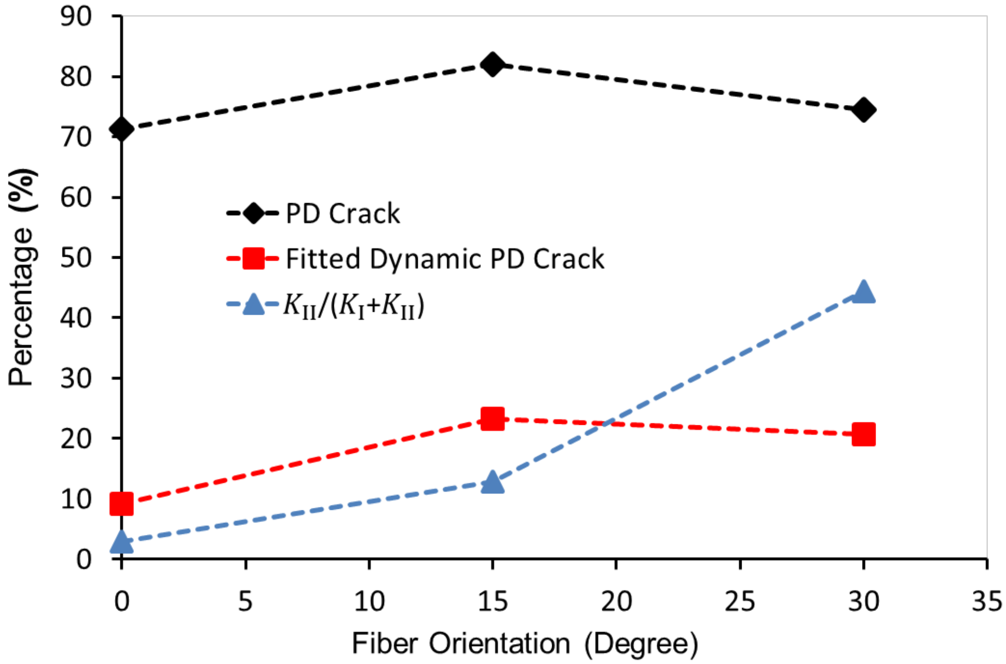

Figure 4.18 Percent of error of peak velocity value calculated with PD by using ordinary fracture energy and by using the fitted simultaneous dynamic fracture energy for fracture along fibers in 0º, 15º, and 30º orientations. And the percentage of mode II fracture in the corresponding fracture patterns [24].

The crack velocity peak value calculated from PD by using both ordinary toughness and the fitted dynamic toughness has been compared to that from the experimental results [24]. The error of the simulated peak crack velocity in composites with fiber in 0º, 15º, and 30º is shown in Figure 4.18. The corresponding percentage of mode II fracture over mode I and mode II fracture from the experiments is also shown in Figure 4.18. Based on the comparison in Figure 4.18, the peak crack velocity error calculated with the ordinary PD modeling is as high as 70% ~ 80%, which is about 60% higher than the error calculated with the fitted simultaneous dynamic PD modeling. By applying the instantaneous dynamic fracture toughness to PD failure simulation, the peak crack velocity error can be brought down by about 87%, 79%, and 73% for dynamic fracture in composites with fiber in 0º, 15º, and 30º respectively, compared to the results by using ordinary PD modeling. Therefore, to predict the high-speed dynamic fracture process more accurately, it is recommended to apply the simultaneous dynamic fracture toughness to the bond failure criteria in PD.

The peak crack velocity error differs in composites with different fiber orientations as described in Figure 4.18. Error for fracture in 0º direction is about 10% lower than that for fracture in 15º, and 30º directions, which is consistent with the percentage of mode II fracture in composites with different fiber orientations as shown in Figure 4.18. The bond failure criteria were defined with the mode I fracture toughness in this paper, so the error is much smaller for fracture in 0º which has the majority of mode I fracture. One possible reason for the larger errors for fracture in 15º and 30º directions can be due to the use of the orthogonal grid pattern in this study. Further experiments and PD simulations of mixed modes dynamic fracture in directions like 15º, 30º, and 45º are to be conducted.

4.6 Conclusion

A new bond-based peridynamic model with continuous material constant (meso-modulus) has been developed for unidirectional composites by using a homogenization method. Impact fracture can be simulated in the lamina with fiber oriented not only in grid-friendly directions 0º, 45º, and 90º but also in such arbitrary directions as 15º or 30º. A simultaneous crack velocity related dynamic strain energy release rate was extracted from fitted experimental results. By applying the simultaneous dynamic fracture energy formulations into the failure criteria (critical stretch) in the PD model, the calculated dynamic fracture process and crack velocity match better with the experimental results than the ones which use a constant fracture energy.

Chapter 5. Peridynamic Modeling of Impact-induced Damage Evolution and Delamination in Laminated Composite Materials

In this chapter, the two-dimensional bond-based peridynamic model for orthotropic composites has been extended into three-dimensional for laminated composites. In the model, both the critical bond stretch and critical bond compression have been used to describe the damage of the intralayer and interface of laminated composites. The proposed PD model is then employed to study the damage of a laminated composite plate subjected to out-of-plane impact loading. The laminates have different fiber layouts [90/θ/90], where θ varies from 0º, 15º, 30º, 45º, 60º, and 75º. The matrix and intralayer damage initiation and propagation, as well as the interlayer delamination, have been simulated with the PD model. A consistent trend of the damage and delamination patterns to the experimental results [47] have been predicted and discussed.

5.1 The PD Model for Laminated Composites

5.1.1 Micromodulus of bonds

A two-dimensional peridynamic model for a lamina[77] has been extended into three-dimensional for laminated composite. In the model, the assumption C_θ/C_2 was defined for intralayers as shown in Eq. (5-1), where E_x is the off-axis Young's modulus, and ν_{xy} is the corresponding Poisson's ratio. Material constant C_θ is dependent on C_2, E_x, and ν_{xy} for bonds in arbitrary directions. The details of the description and calculation of continuous micromodulus C_θ can be found Chapter 4, section 4.2, and in papers [77,78]. The micromodulus of interlayer bonds are defined the same as that of the matrix bonds.

$$\frac{c_\theta}{c_2} = \frac{E_x(1-2*\upsilon_{21})}{E_2(1-2*\upsilon_{xy})} \tag{5-1}$$

5.1.2 Failure criteria

The failure of intralayer bonds and interlayer bonds has been defined in this section. For the intralayer bonds in an orthotropic lamina, the bond's failure was defined as fiber bond's failure and matrix bond's failure, as shown in Figure 5.1. Critical stretch for bonds in the fiber direction was defined as s_{1t}. Critical stretch for bonds in the transverse direction is set as stretches s_{2t}. The critical stretch s_{1t} is equalized with the longitudinal ultimate teinsile strain ε_L^{ten}. The critical stretch s_{2t} is equalized with the transverse ultimate teinsile strain ε_T^{ten}. Equations of s_{1t} and s_{2t} are presented in Eq. (5-2). The corresponding critical compression of material bonds are defined as s_{1c} and s_{2c}, which can be equalized to the longitudinal ultimate compressive strain ε_L^{com} and transverse ultimate compressive strain ε_T^{com} seperatly, as shown in Eq. (5-3). For bonds in all other directions, the critical tensile strech and compresion are defined as the fourth order of sinusoidal equations of critical stretch in longitudinal and transverse direction, as shown in Eq. (5-4) and Eq. (5-5). The interlayer bonds failure criteria are set as the same as the matrix bonds. The interlayer critical stretch and compression are defined as the same as that of the intralayer bonds in transverse direction.

For each intralayer material point, it interacts with both the in-plane material points and the material points in the adjacent layer within the horizon, as shown in Figure 5.2. The damage of the intralayer material points is set as the ratio of broken bonds to the initially connected bonds. For each intralayer material point, the ratio of the broken bonds crossing the interlayer to all the original bonds crossing the interlayer is defined as the interlayer damage.

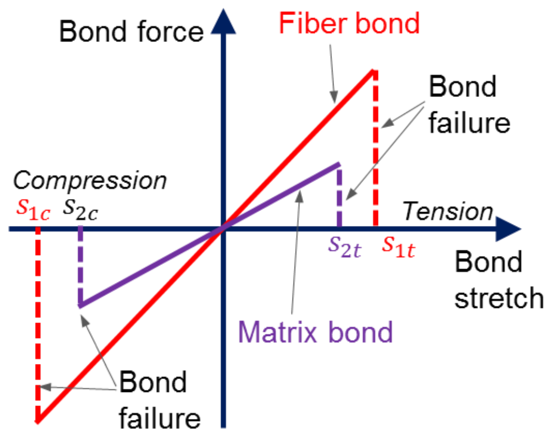

Figure 5.1 Peridynamic failure criteria. Critical stretch of bonds in fiber direction and transverse direction.

$$s_{1t} = \varepsilon_L^{ten}, \; s_{2t} = \varepsilon_T^{ten} \tag{5-2}$$

$$s_{1c} = \varepsilon_L^{com}, \; s_{2c} = \varepsilon_T^{com} \tag{5-3}$$

$$s_t = s_{1t} * \cos^4\theta + s_{2t} * \sin^4\theta \tag{5-4}$$

$$s_c = s_{1c} * \cos^4\theta + s_{2c} * \sin^4\theta \tag{5-5}$$

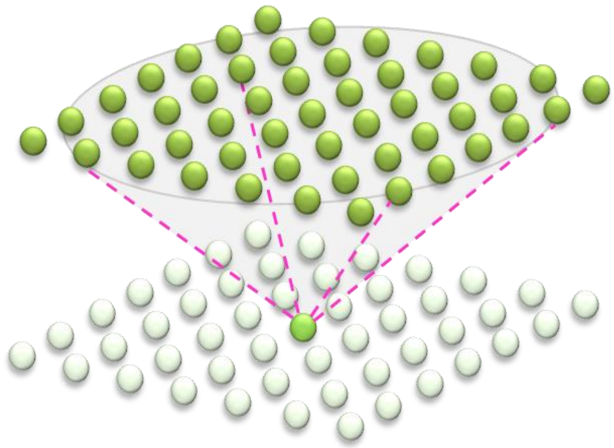

Figure 5.2 The intralayer material bond interacts with the material points in the adjacent layer within the horizon.

5.1.3 Problem description

The PD model is employed to study the impact-induced delamination and matrix damage in a laminated composite plate as shown in Figure 5.3. The laminated plate is with the fiber orientation [90/θ/90], where θ varies from 0º, 15º, 30º, 45º, 60º and 75º. The square plate is 90 *mm* long, 90 *mm* wide, and 1.5 *mm* thick. The composite laminate is made of E-glass fibers and SC-15 epoxy. The composite plate is fixed in between two clamp plates as the boundary condition. The impact loading is added to the center of the top surface of the composite plate. The material properties and the ultimate tensile/compressive strain of the E-glass/epoxy lamina are listed in Table 5-1 and Table 5-2.[69,79]

Table 5-1. Material properties of the E-glass/epoxy lamina.[69]

Longitudinal Young's modulus, E_1	Transverse Young's modulus, E_2	Poisson's ratio, ν_{12}	Shear modulus, G_{12}	Density, ρ
41 Gpa	10.4 Gpa	0.28	4.3 Gpa	1970 kg/m^3

Table 5-2. The ultimate strain of the unidirectional E-glass/epoxy lamina.[79]

Longitudinal tension, ε_L^{ten}	Longitudinal compression, ε_L^{com}	Transverse tension, ε_T^{ten}	Transverse compression, ε_T^{com}
0.028	-0.015	0.0038	-0.012

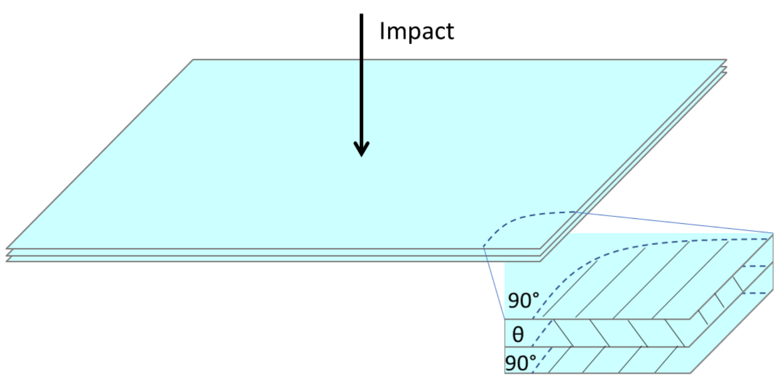

Figure 5.3 The impact on the top surface of the laminated composite plate.

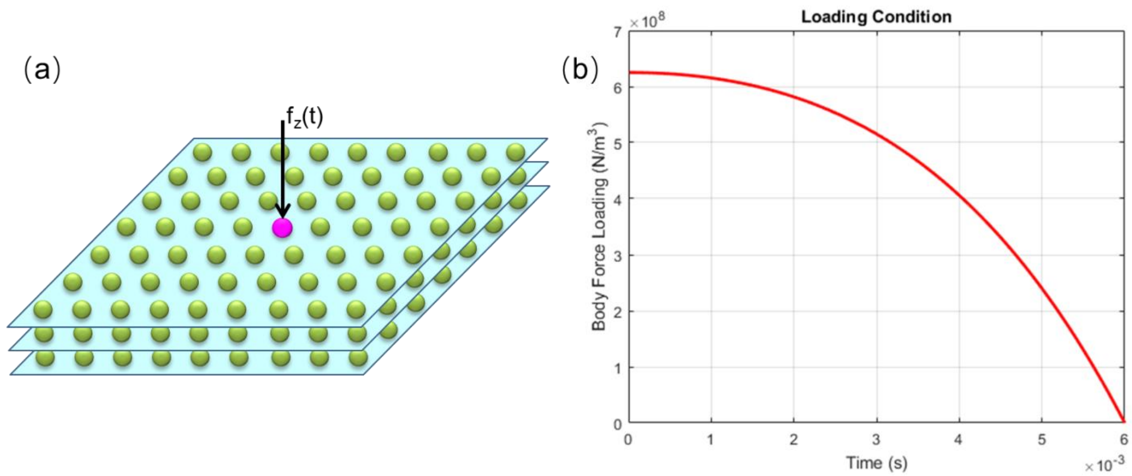

Figure 5.4 Impact algorithm. (a) Body force added to the material point at the center of the top layer. (b) Body force.

The laminate plate is discretized into orthogonal PD cubic material points with a unit length size of 0.5 *mm*. Each material point has a horizon with the size of δ = 3.2*dx as suggested by Hu[67] and Silling.[19] The time step for the PD explicit integration is set as dt = 1 x 10^{-5} *s* based on the stability analysis in the paper.[19] Impact loading is added to the center of the top surface of the plate. To simulate the impact condition, a time-dependent body force was added to the material point in the center of the top layer as shown in Figure 5.4 (a). To simulate the impact force magnitude and time period, the body force was set as shown in Figure 5.4 (b). The laminated plate has a fixed boundary condition in PD modeling. The material points within a horizon of the boundary were defined with zero displacements in x, y and z directions for all the time steps.

5.2 Results and discussion

The impact-induced matrix/intralayer damage and delamination have been simulated with the PD model for laminates with lamina layouts of [90/0/90], [90/15/90], [90/30/90], [90/45/90], [90/60/90], and [90/75/90]. The intralayer damage, delamination, and out-of-plane displacement contours are shown in the following figures. The detail laminate damage initiation and evolution process will be discussed in the laminates [90/0/90]. The damage patterns of the composites after certain time of loading are also discussed for the laminates [90/15/90], [90/30/90], [90/45/90], [90/60/90], and [90/75/90].

5.2.1 Impact-induced intralayer damage and delamination process in laminates [90/0/90]

The PD simulated matrix damage and delamination in the laminates [90/0/90] are shown in Figure 5.5, Figure 5.6, and Figure 5.7. Damage initiation in the laminates was captured after 150 μs of the loading, as shown in Figure 5.5. The matrix damage initiated from the second layer, in which the fiber is in the direction of 0º. The damaged area is in a small peanut shape along the fiber direction in this layer. Seldom damage occurred in the top and third layers. The initiation of the matrix damage is due to the shear loading rather than compression or tension in the top and bottom surface of the plate. The delamination initiated in the first interlayer (the interlayer between the top layer and the second layer), shown as the delamination 1 in Figure 5.5. No delamination occurred in the second interlayer. The out-of-plane displacement of the plate is shown in Figure 5.5.

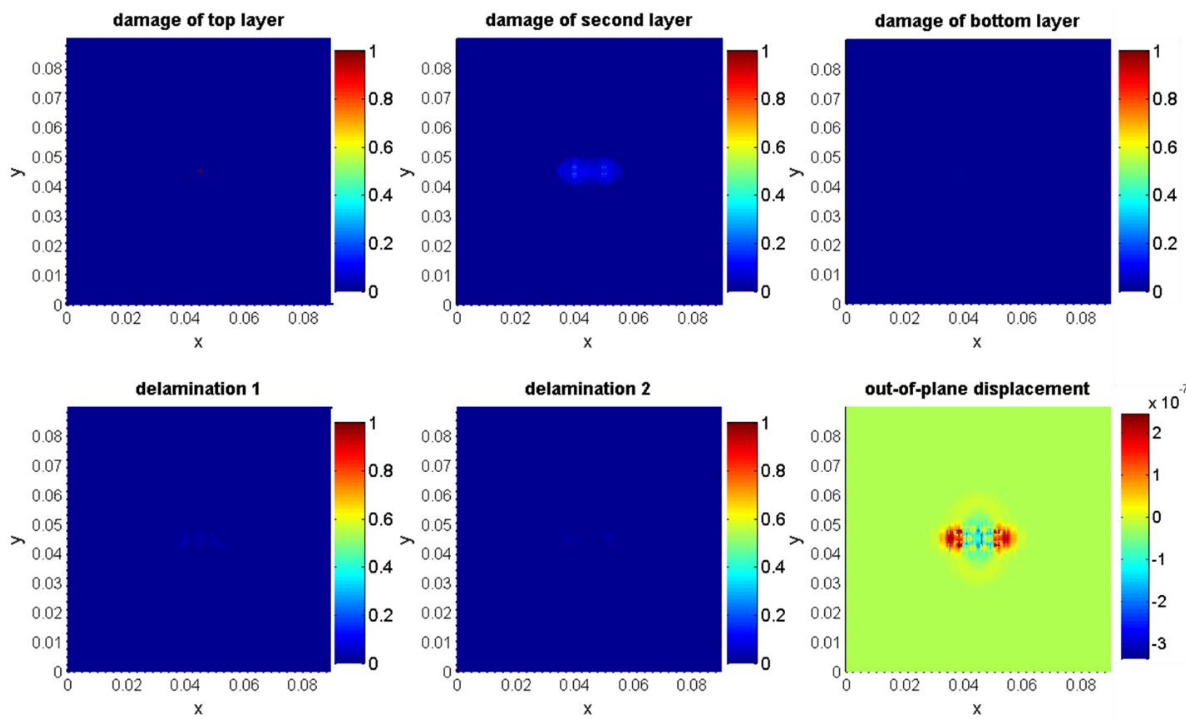

Figure 5.5 Intralayer damage, delamination, and displacement field of the laminates [90/0/90] at damage initiation, after loading for 150 μs.

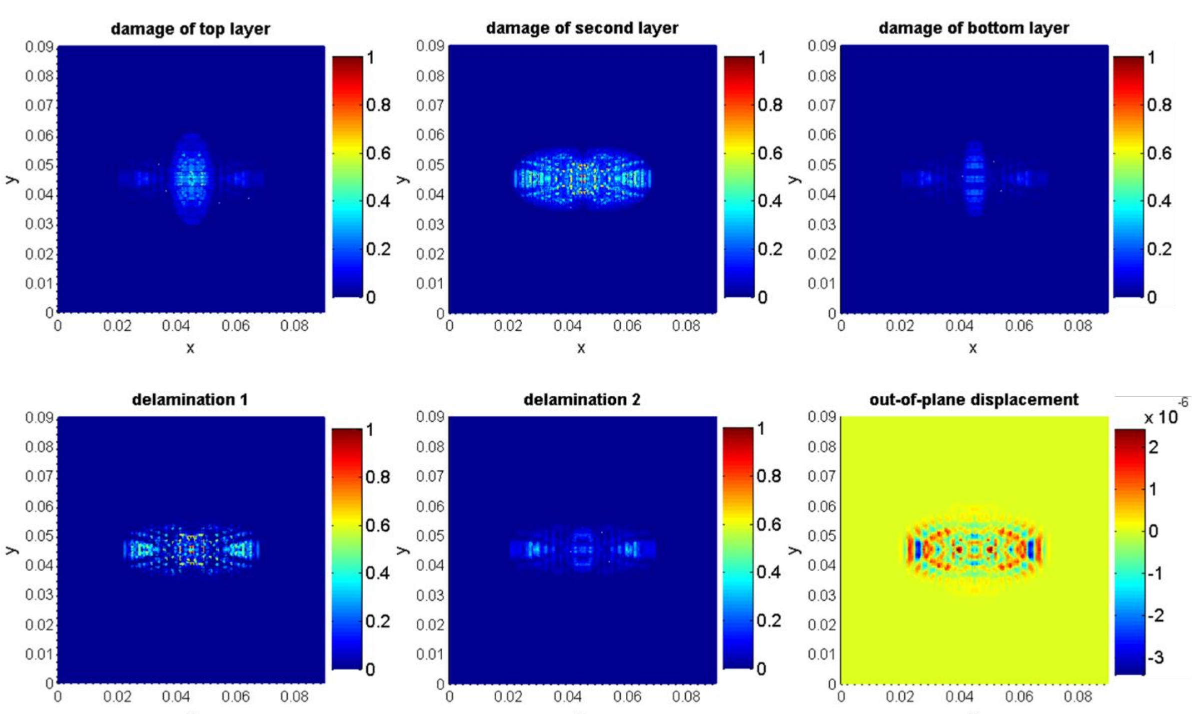

Figure 5.6 Intralayer damage, delamination, and displacement field of the laminates [90/0/90] after loading for 250 μs.

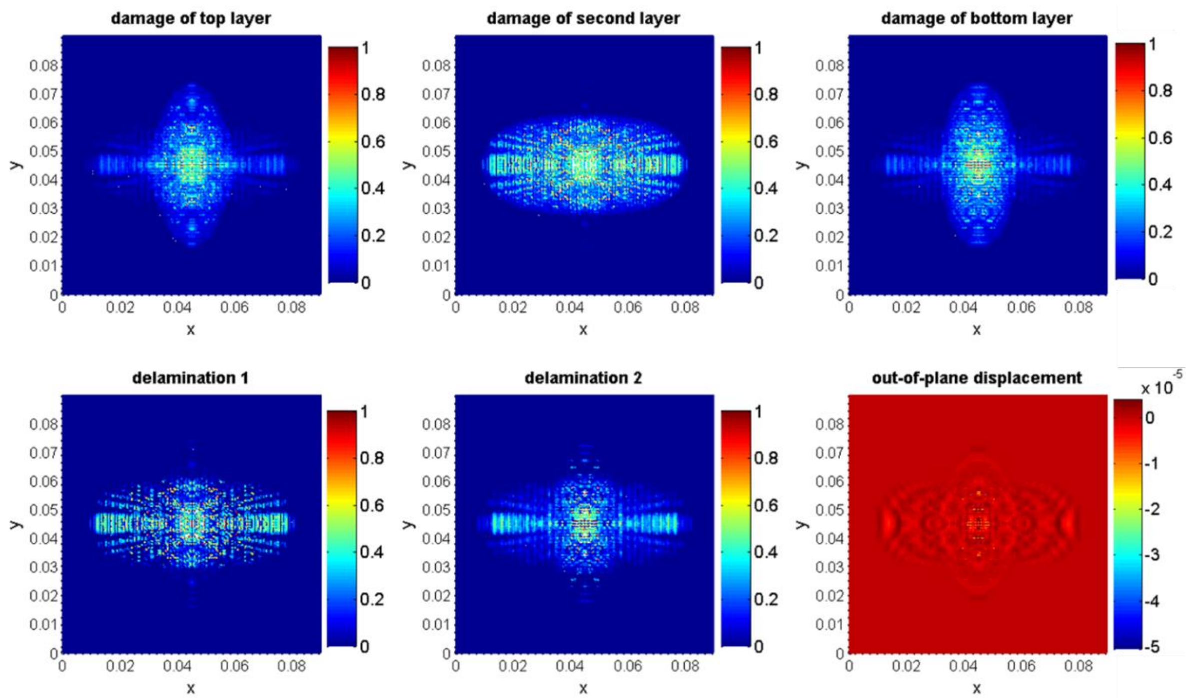

Figure 5.7 Intralayer damage, delamination, and displacement field of the laminates [90/0/90] after loading for 350 μs.

The intralayer damage and delamination of the laminates [90/0/90] at 250 μs after the impact loading is shown in Figure 5.6. The out-of-plane displacement value is getting larger than the one at the damage initiation. Also, the deformation area is getting bigger around the impact center, especially in 0º direction, resulting in a peanut-shaped region along the 0º direction. The displacement field is symmetric by both x and y-axis crossing the plate center. Matrix damage occurred in all the three layers. In the top layer, the damage at the center has an ellipse shape along the fiber direction in 90º, the damage in the second layer is a larger ellipse-shaped area along the fiber direction in 0º. The matrix damage in the bottom layer is extended in both 0º and 90º. Matrix damage areas in the middle and bottom layers are bigger than that in the top layer, as shown in Figure 5.6. Delamination for the first interlayer is typically in peanut shape and has a similar area to that of the damage in the second layer. Delamination shape in the second interlayer has a shape and area close to the damage in the bottom layer.

The intralayer damage and delamination of the laminates [90/0/90] 350 μs after the impact loading are shown in Figure 5.7. The out-of-plane displacement value and area are getting even larger than that at the damage initiation. Both matrix damage and delamination areas increased. The matrix damage areas in the top and bottom layers have the similar sizes and shape of the ellipse along the fiber direction in 90º. The matrix damage in the second layer has a larger size, and with the shape of the ellipse along the fiber direction in 0º. Delamination in the first interlayer has a typical peanut shape along the fiber direction of the second lamina (in 0º). It also has a similar area size to the damaged area of the second lamina. Delamination in the second interlayer is also getting bigger and has a similar shape to that of the damage in the bottom layer.

5.2.2 Impact-induced intralayer damage and delamination in laminates [90/15/90], [90/30/90], [90/45/90], [90/60/90], and [90/75/90].

The PD simulated intralayer damage, delamination, and displacement field of the laminates [90/15/90] after loading for 250 μs is shown in Figure 5.8. All the damage and delamination areas are centrosymmetric due to the impact loading at the center of the plate. In the top layer, the damage at the center has an ellipse shape along the fiber direction in 90º. The damage in the second layer is a larger ellipse-like-shaped area along the fiber direction in 15º. The damaged areas in the top layer and second layer are larger than that of the bottom layer, which has a smaller ellipse shape along the direction close to but not precisely in 90º (fiber direction). The intralayer damage in both top and bottom layer contain part extended in 15º, the fiber direction for the second lamina. Delamination for the first interlayer is typically centrosymmetric in an oblique peanut shape and has a similar area and orientation to that of the damage in the second layer. Delamination shape in the second interlayer has a smaller area and with the shape close to the damage in the bottom layer. The out-of-plane displacement field is also with an ellipse shape along the direction of 15º, and with an area slightly bigger than the damaged area.

The PD simulated Intralayer damage, delamination, and displacement field of the laminates [90/30/90] after loading for 300 μs is shown in Figure 5.9. Similar to the damage patterns of the laminates [90/15/90], The intralayer damage areas have the peanut ellipse shape and orientation in the in-plane fiber directions. The delaminations areas have the similar shape and size to the damaged area in the corresponding lower layer.

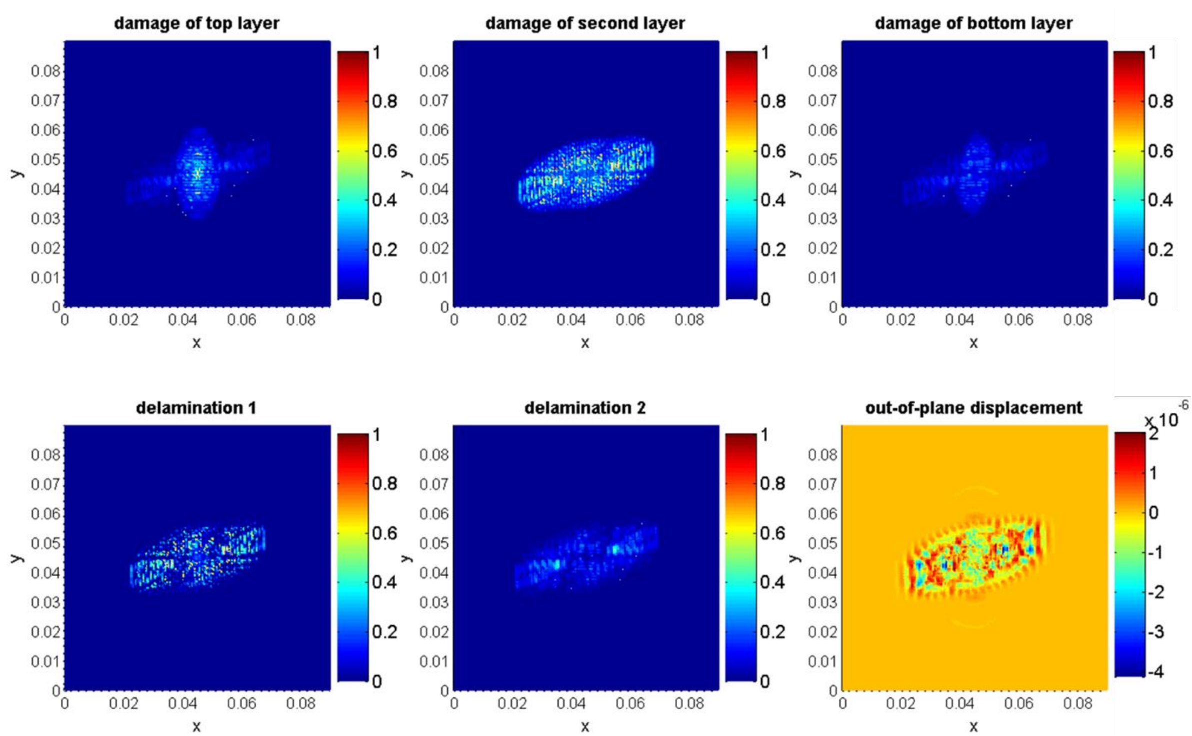

Figure 5.8 Intralayer damage, delamination, and displacement field of the laminates [90/15/90] after loading for 250 μs.

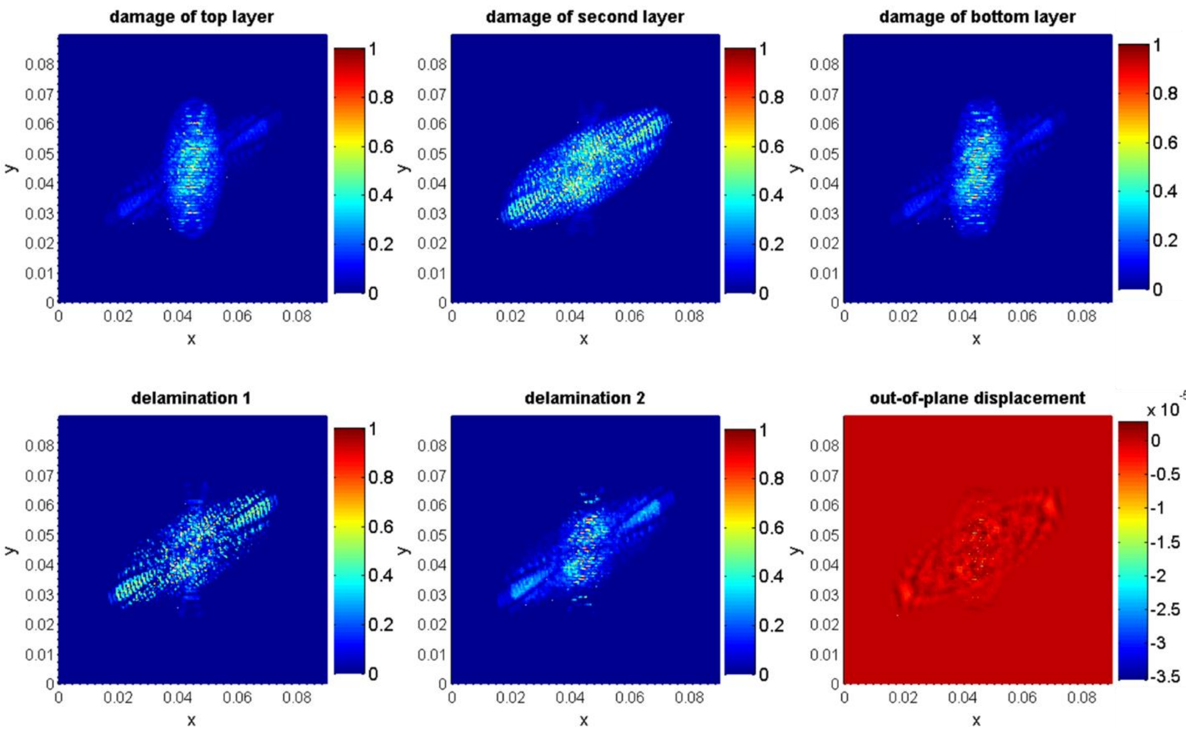

Figure 5.9 Intralayer damage, delamination, and displacement field of the laminates [90/30/90] after loading for 300 μs.

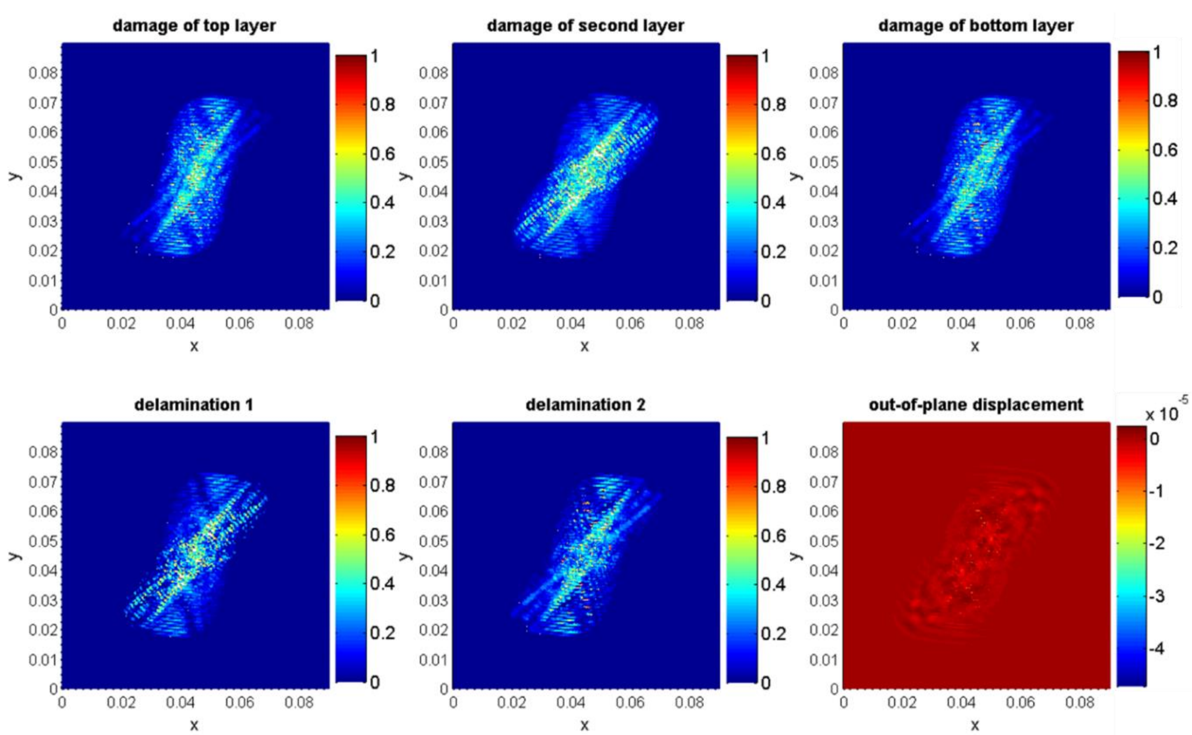

Figure 5.10 Intralayer damage, delamination, and displacement field of the laminates [90/45/90] after loading for 300 μs.

The PD simulated intralayer damage, delamination, and displacement fields of the laminates [90/45/90] after loading for 300 μs, laminates [90/60/90] after loading for 250 μs, and laminates [90/75/90] after loading for 300 μs are shown in Figure 5.10, Figure 5.11, and Figure 5.12 respectively. The contours of the layer damages, delaminations, and the out-of-plane displacements have the similar patterns for these three laminates. Firstly, all the damage and delamination areas are centrosymmetric due to the impact loading at the center of the plate. In the top layer, the damage areas have the oblique peanut shape along the direction between the two fiber directions of the top layer in 90º and the second layer in 45º, 60º, and 75º. The damage areas in the second layer have the most significant size and orientations along the fiber direction in 45º, 60º, and 75º. The damage areas in the top layer and second layer are larger than that of the bottom layer, which has the similar shapes, sizes, and orientations to the damage areas in the top layers. The delamination areas have similar shapes, sizes, and orientations to the damage areas in the corresponding layer below the interlayer. The out-of-plane displacement fields are also with the peanut shape along the directions of intralayer damage orientations, and with an area slightly bigger than the damage areas.

For all the laminates, the intralayer damage areas have the peanut shape and the orientations in exactly or close to the fiber directions. The delamination areas also have the peanut shapes, with sizes and orientations close to that of the corresponding layer below. The out-of-plane displacement fields have the areas size covering all the intralayer and interlayer damage sizes, and a shape covering all the intralayer and interlayer damage shapes. More damage evolution process of the laminates [90/15/90], [90/30/90], [90/45/90], [90/60/90], and [90/75/90] will be presented in Appendix D.

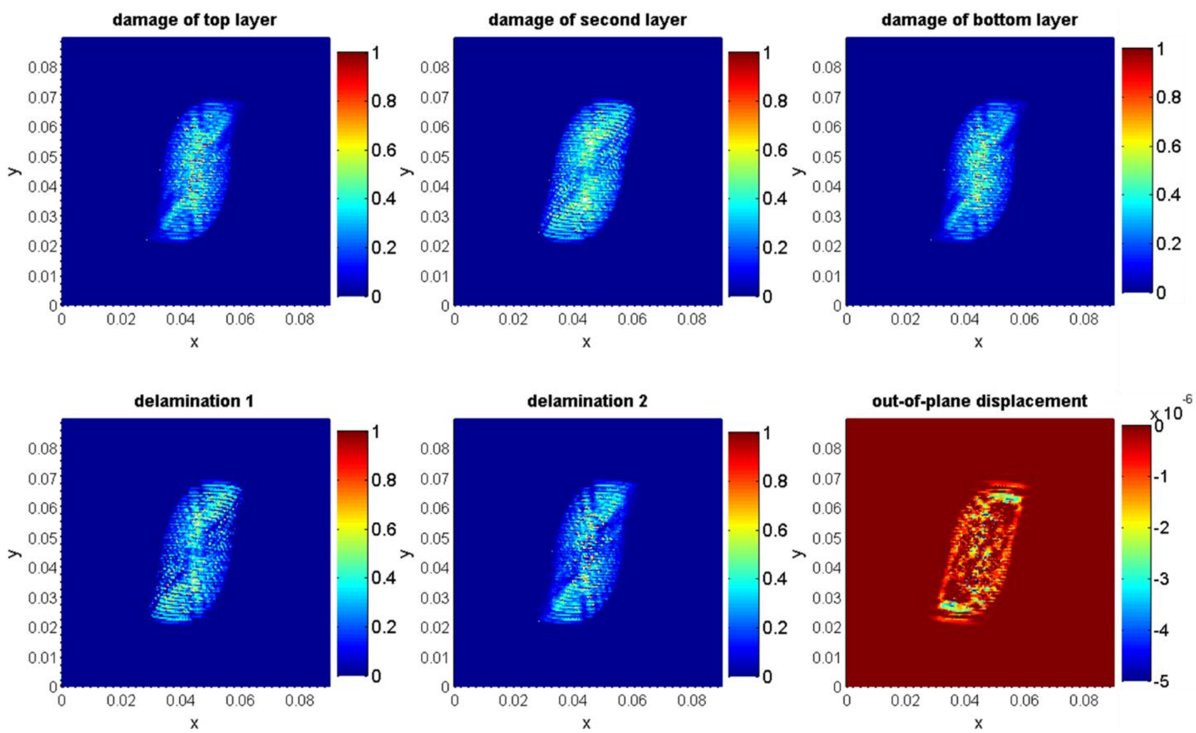

Figure 5.11 Intralayer damage, delamination, and displacement field of the laminates [90/60/90] after loading for 250 μs.

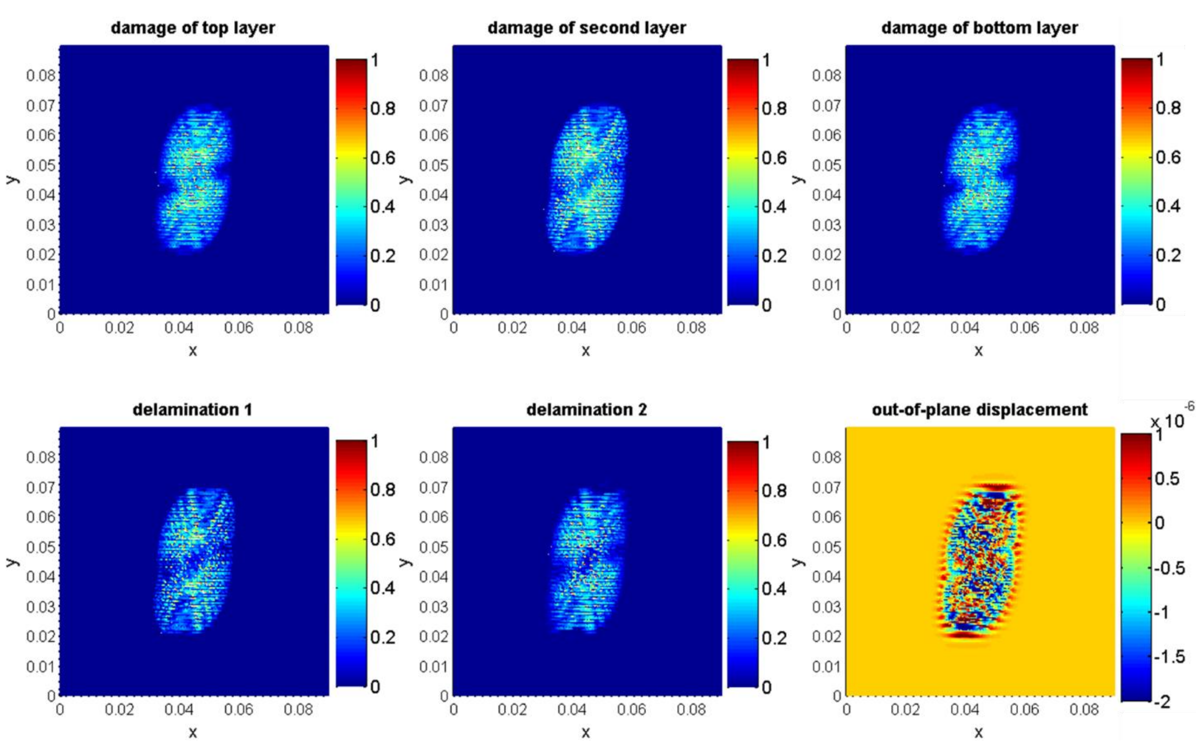

Figure 5.12 Intralayer damage, delamination, and displacement field of the laminates [90/75/90] after loading for 250 μs.

5.3 Conclusion

The bond based peridynamic model for unidirectional lamina has been extended for the composite laminates, with the definition of micromodulus and failure criteria for interlayer bonds. Out-of-plane impact on the [90/θ/90] laminate composites has been simulated with the peridynamic model. Matrix damage in each layer and delamination in the interlayers have been simulated with the PD modeling.

Chapter 6. An Experimental Study of the In-plane Tensile Properties and the Out-of-plane Low-velocity Impact Damage Process of the Unidirectional Laminate, Two-dimensional Woven Laminate, and the Quasi-three-dimensional Carbon Fiber Composite Materials

6.1 Introduction

Delamination is one of the most common failure modes of the laminated composites in application. To explore the composite materials with higher delamination resistant capability, the quasi-three-dimensional (Q3D) composite structure has been introduced [80]. In the Q3D fiber structure, the fibers from each layer are woven into those in the adjacent layers (above and below). As a result, the multiple layers physically attached to each other through the thickness direction [80]. The Q3D woven fiber layers are physically interlocked and held together as one three-dimensionally woven structure. But the Q3D woven structure is different from the three-dimensional (3D) weaves that with the fiber yarns specifically weaved in the thickness direction. Due to the step-by-step interlocking through the thickness, the fiber yarns in the Q3D structure can be maintained as flat as possible to keep an effective in-plane stiffness as the laminates. The study [80] on bi-axial Q3D woven structure ([0/90]) shows that bi-axial Q3D weaves had "lower impact-induced damage, higher specific energy absorption, lower impact-induced structural degradation, and competitive in-plane properties than the laminated counterparts." [80]

In this study, the Q3D woven structure has the tri-axial fiber orientation in 0º, 60º, and -60º. Compared to the bi-axial Q3D woven structure in 0º and 90º, the current tri-axial

Q3D structure is supposed to have a greater in-plane isotropy and a better resistance to delamination [81]. The three composite structures are the unidirectional laminate (UDL) in $[0/60/-60]_4$, the two-dimensional plane weaved laminate (2DW laminate) in $[\underline{0/60/-60}]_4$, and the quasi-three-dimensional composite structure (Q3D) in $\underline{[0/60/-60]_4}$. The study aims at identifying the potential advantage of the advanced Q3D composite structure in delamination, and the competitive other material properties, such as the in-plane stiffness and strength.

Firstly, the composite panels were fabricated with the vacuum injection process with the curing at 122 ºC for 4 hours. The tensile specimens along orientations at 0º, 15º, 30º, and 90º were prepared and tested according to the ASTM D3039 standard. Secondly, the unidirectional tensile testing of the specimens was conducted with the MTS machine, combining the three-dimensional Digital Image Correlation (3D DIC) method, from which the loading-deformation relations of the tensile testing have been extracted. Then, the tensile modulus, Poisson’s ratio and tensile strength of the oriented specimens have been calculated for the three composite structures. The quasi-isotropic material properties and the orientation influence on the tensile strength of the composite structures have been analyzed and discussed. Moreover, the out-of-plane low-velocity impact testing was conducted for the three composite plate samples, combining with the 3D DIC analysis. The impact loading, deformation, and the impact penetration damage process will be discussed.

6.2 Fabrication of the composite plaques

6.2.1 The fiber structures preparation

The Q3D fiber structure can be braided with the braiding machine at CVRC, MSU, as shown in Figure 6.1(a). The machine braids the fibers into a closed cylindrical tube-shaped fabric as shown in Figure 6.1(b). The braided Q3D structure has the fibers oriented in three directions as shown in Figure 6.1(c), the 0º direction, and the other two symmetric θ directions, where θ can be set as the desired angle by operating the braiding machine.

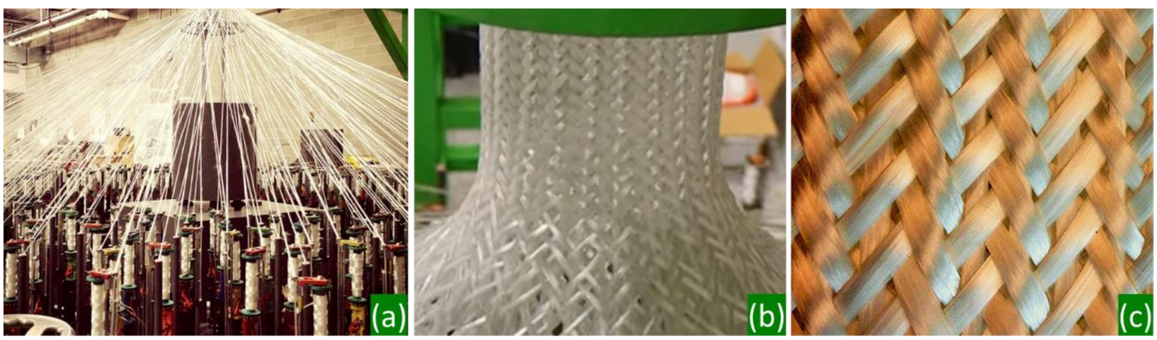

Figure 6.1 Quasi-three-dimensional (Q3D) composite structure. (a) The braiding machine, (b) the braiding process, and (c) the braided Q3D glass fiber structure.

The carbon fibers are provided by the Ford Motor Company. The carbon fiber is the DOWAKASA 24K A-42, with the tensile modulus of 240 GPa, and the tensile strength of 4200 MPa. The fiber tows were used to prepare the UDL structure and braid the 2DW and the Q3D structures, which is shown in Figure 6.2.

Each of the three composite structures has a twelve ply of fibers, repetitively orientating in three different directions as -60º, 0º, and 60º. The UDL fiber structure is as shown in

Figure 6.2(a), with the unidirectional fiber ply orientation $[0/60/-60]_4$. The 2DW structure is a layup of four woven fabrics, each is braided with the fibers in -60º, 0º, and 60º directions. The 2DW has a fiber ply orientation $[\ \underline{0/60/-60}\ ]_4$, as shown in Figure 6.2(b). The Q3D structure is directly braided with the twelve plies repetitively in the orientation of directions as -60º, 0º, and 60º ($\underline{[0/60/-60]_4}$), as shown in Figure 6.2(c). Each layer was braided interlocked with the adjacent layer, resulting in an integral fabric structure.

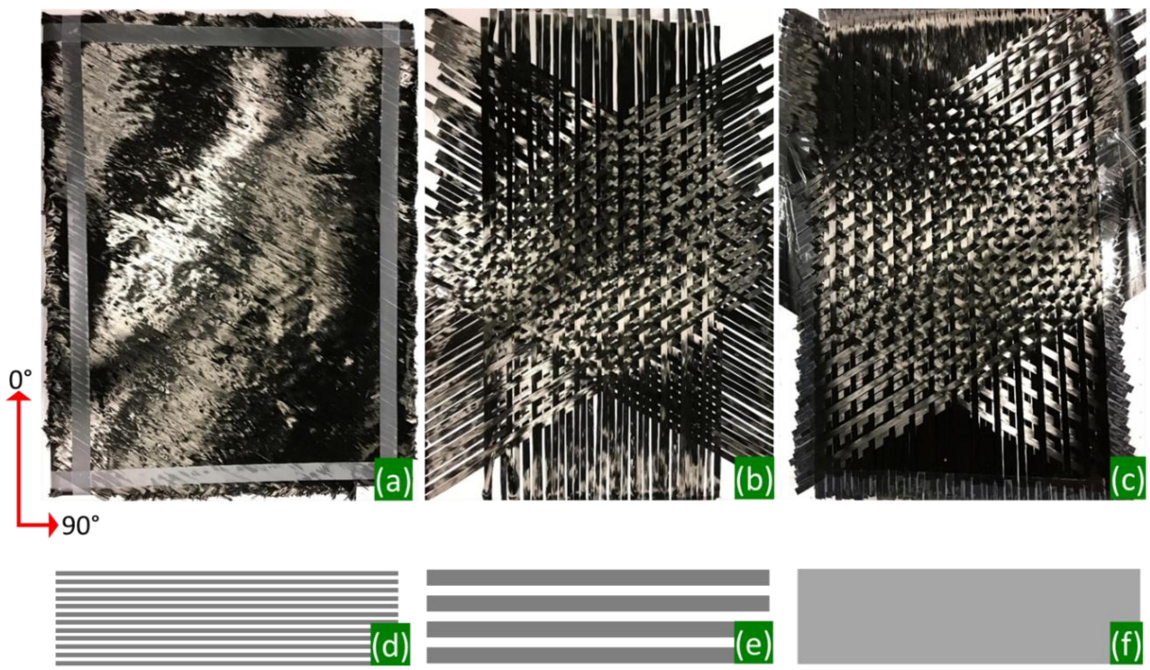

Figure 6.2 The carbon fiber braided structures. (a) UD laminate, (b) 2DW laminate, and (c) Q3D fabric.

6.2.2 Fabrication process of the composite plaques

The resin system used for the composite fabrication is the SC-15 epoxy, which is used by being mixed with the hardener (part B). The curing of the resin is conducted at 122 ºC for 4 hours as suggested in the study [82]. The vacuum infusion setup and process are shown in Figure 6.3. Firstly, a flat aluminum flat plate mold is prepared with its surface cleaned and polished with the sandpaper. Then mold surface is coated with a thin layer of the release agent, for composite plaques releasing after the curing. A releasing cloth is then placed on the surface of the plate mold, with the fabrics directly on the cloth as shown in Figure 6.3(a). Another release cloth is then placed on the fabric with a drainage grid placed on it as shown in Figure 6.3(b). The sealing tape with the inlet and the outlet is then placed around the fabrics. A vacuum bag is then placed on the sealing tape to seal the fabrics inside. The inlet is for resin flowing through the whole fabrics as the infusion, the outlet is connected to a vacuum pump to suck the air inside the sealing space. Once the inlet is closed, the vacuum pump is turned on and the air inside is sucked out. After the pressure inside reaches the negative standard atmosphere air pressure, with no leaking for the whole sealing bag, the inlet is put into the bucket with resin. The resin is sucked into the vacuum bag and goes through the fabrics. Once the resin reaches the other end of the fabrics, both the inlet and the outlet will be closed. The whole plate is then placed into the oven, curing at 122 ºC for 4 hours [82].

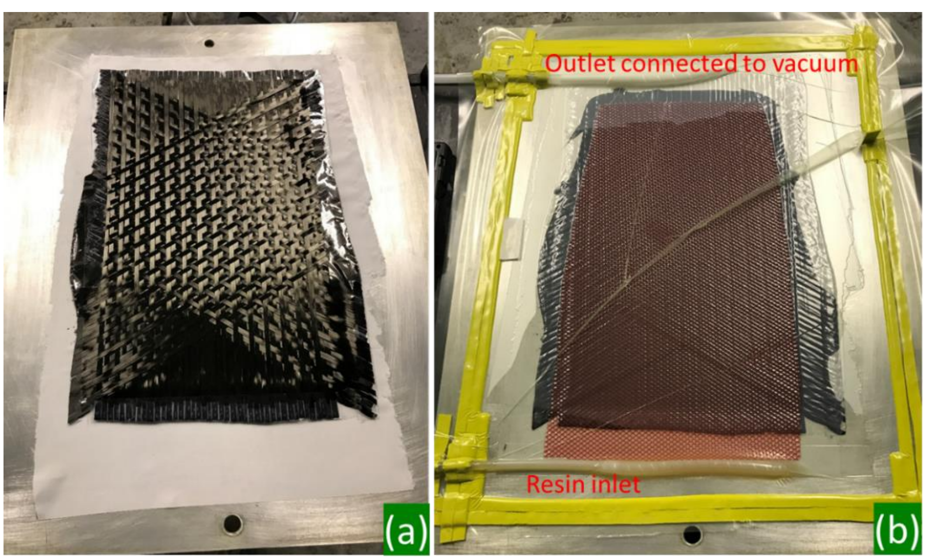

Figure 6.3 The vacuum infusion process. (a) the layout of the releasing cloth and the fabric, (b) vacuum infusion setup.

6.3 In-plane quasi-static tensile testing

In-plane material properties have been studied with the unidirectional tensile testing. The tensile loading conditions and specimen preparation were conducted according to the ASTM D3039 [83]. Details from the specimen preparation to the tensile failure analysis are discussed below.

6.3.1 Specimen preparation

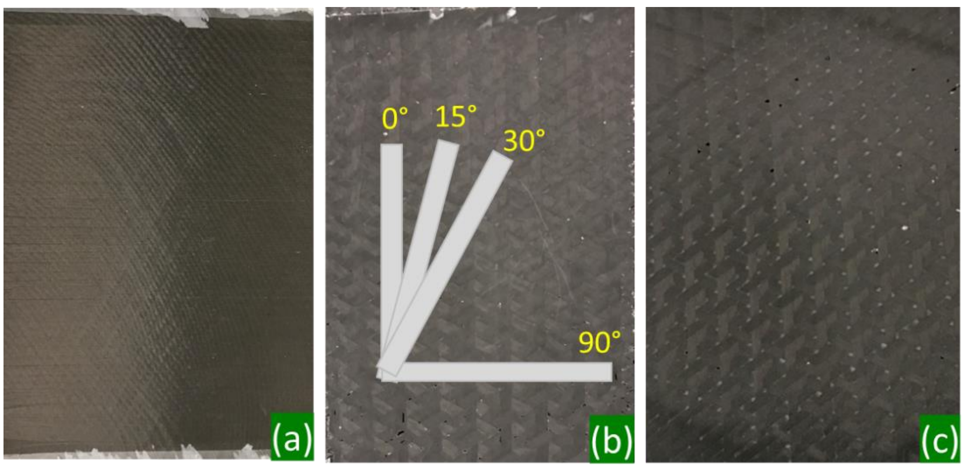

Figure 6.4 The three different composite plaques

The cured composite plates are shown in Figure 6.4. The UDL plate has the smoothest surface with the smallest surface roughness compared to the 2DW and Q3D composite. The difference in composite plaques surfaces is caused by the different fiber structures layout and interlayer fiber tows interlock between laminate fiber layout and woven fiber structures. The three composite plaques have the similar thickness around 2 mm.

The volume fractions of the composite plaques were calculated. The three composites have the same volume of fibers per each unit of the in-plane area. Because they have the same layers and tows amount of the carbon fibers resulted from the same braiding template, even though the fiber tows layout and braiding patterns are different. The fiber volume per unit in-plane area then was calculated as dividing the fiber mass by the area. The thickness of the composite panels was measured as the composite material volume per unit in-plane area. The volume fraction for the UDL, 2DW, and Q3D plaques are then calculated as 42.8%, 44.9%, and 39.6% respectively.

The specimens were cut in different orientations in the three composite structures/plaques. The 0º direction specimen is cut along the fibers in 0º orientation in the composite plaques. Other specimens were cut with angles of 15º, 30º, and 90º to the 0º direction, as shown in Figure 6.4(b). The specimen preparation is shown in Figure 6.5, according to ASTM D3039. The specimens have the size of 9” in length and 1” in width. End taps were cut from a glass-fiber laminated composite plate and mounted to both ends and sides of the specimens with the epoxy glue as adhesive. The specimens are ready for tensile testing after the curing of the epoxy glue.

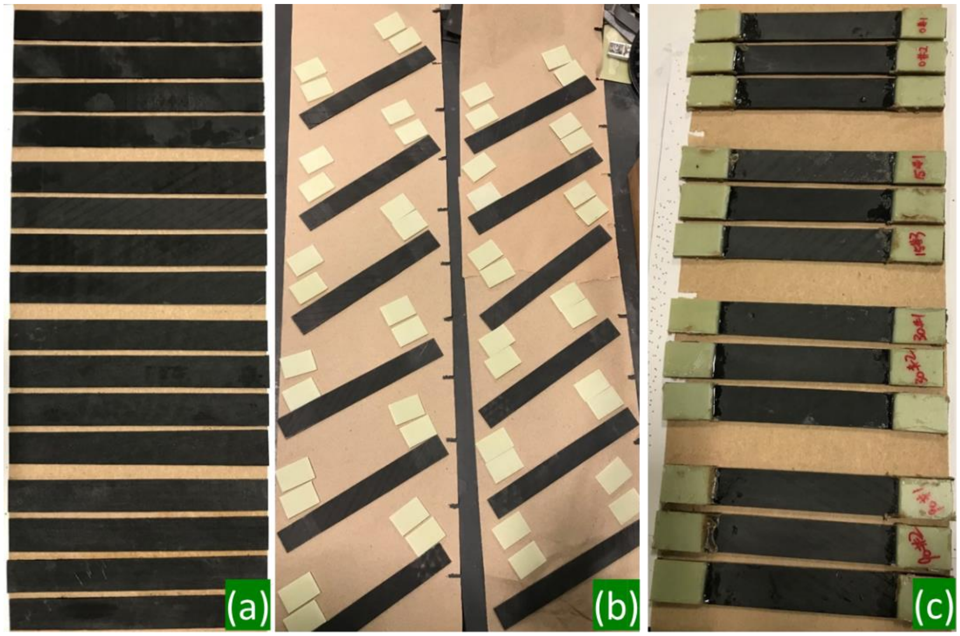

Figure 6.5 specimens

6.3.2 Tensile testing set up

The unidirectional tensile testing system setup is shown in Figure 6.6. Specimens were placed in between the sample clamps of the MTS tensile machine, as shown in Figure 6.6. The MTS machine is connected to the data collection and machine control system as shown in Figure 6.6. The tensile testing is set as displacement loading with the loading rate of 0.2 mm/min, until the tensile failure of the specimens. The MTS machine recorded the tensile loading/force history for each tensile testing.

The light source is used to generate light projected to the surface of the specimens during the tensile testing. Two cameras were supported with the frames and placed in front of the specimen, facing the specimen surface perpendicularly, to catch the loading surface deformation during the tensile process for DIC analysis.

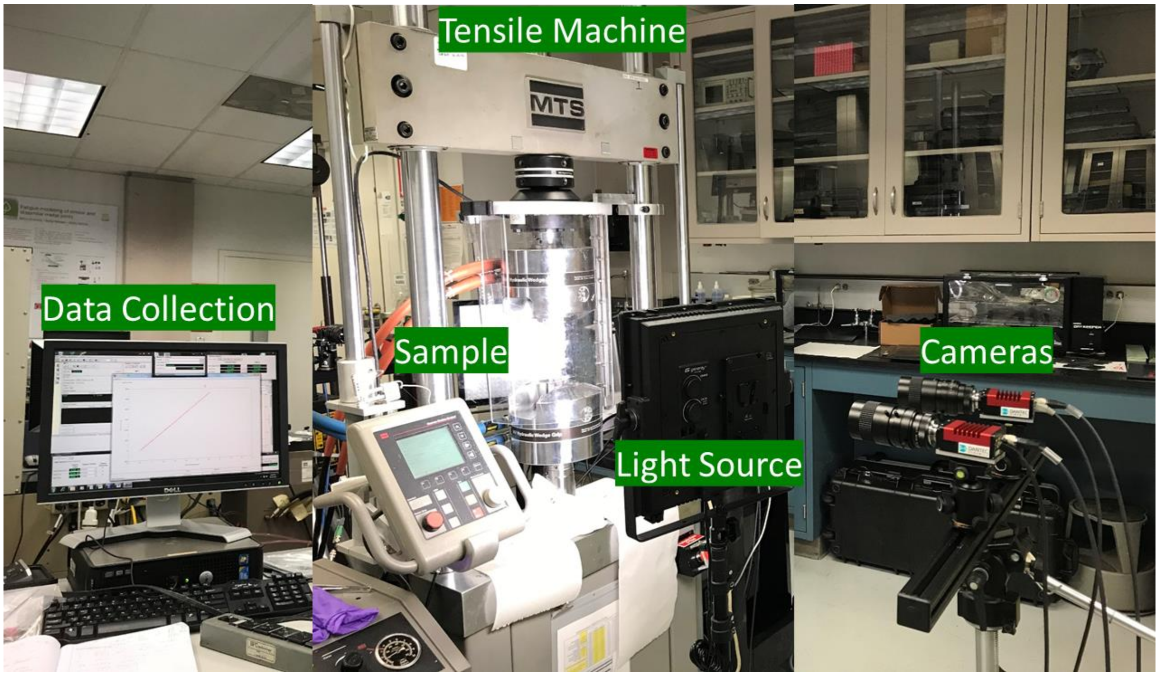

Figure 6.6 Tensile testing setup with MTS machine

6.3.3 Tensile testing load-displacement curve

The deformation process of the specimen is extracted with the 3D DIC analysis. The tensile deformation process was recorded with the two cameras with the figure save frequency of 3/s. The saved figures are then imputed into the 3D DIC software ARAMIS from the GOM Correlate. The deformation/strain fields of the sample surface were calculated with the software. The unidirectional deformation/strain (strain in the loading direction) history is then extracted. For example, the DIC extracted longitudinal strain (strain y) fields of the UDL0º specimen at a different time during the tensile process is shown in Figure 6.7. The strain field was calculated through the whole specimen surface. To exclude the local constraint effect from the specimen clamps of the MTS machine, only the central 1/3 of the strain field contour was used. The average value of the central part of strain contour was calculated with ARAMIS (DIC software), as the strain value at the corresponding time step. The original strain field on the specimen surface is zero before any tensile loading added to the specimen, shown as the first figure in Figure 6.7. As the loading increased, the average strain contour value increased, as marked in the contour bars in Figure 6.7.

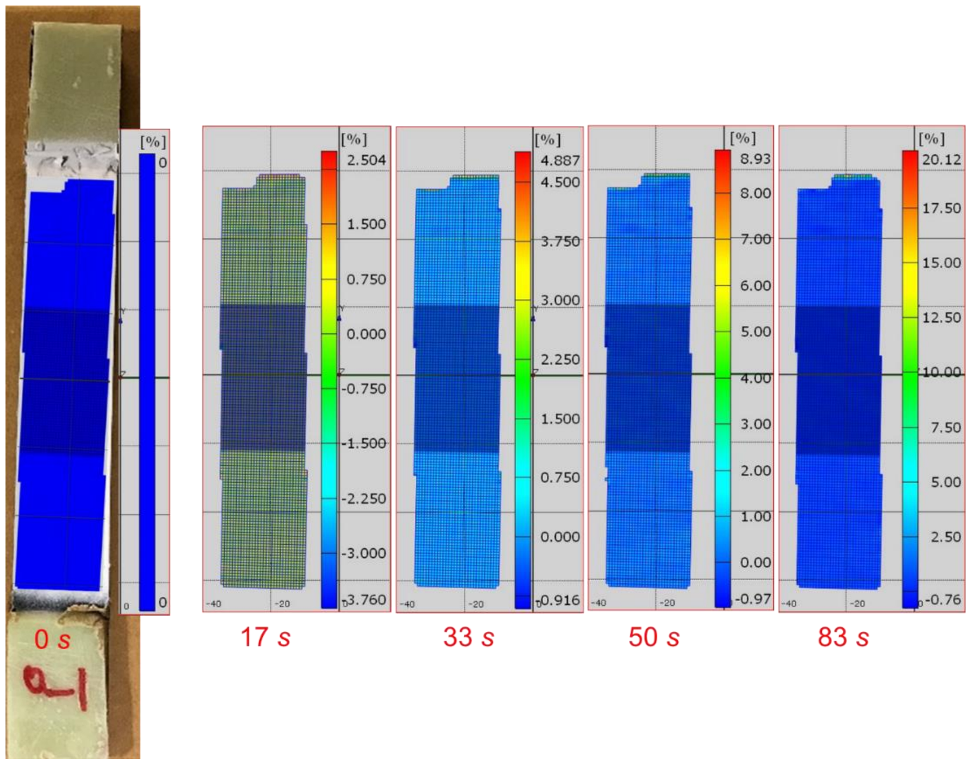

Figure 6.7 DIC extracted longitudinal strain field for the UDL laminate 0° specimen

By combining the DIC extracted strain history with the loading history recorded form the MTS machine, the tensile testing loading-displacement curves for the three different composite specimens were extracted. For example, the loading-displacement curves of the tensile of UDL specimens with different orientations are shown in Figure 6.8. All curves start from the linear elastic stage to the nonlinear stage, then end as the tensile failure of the specimens.

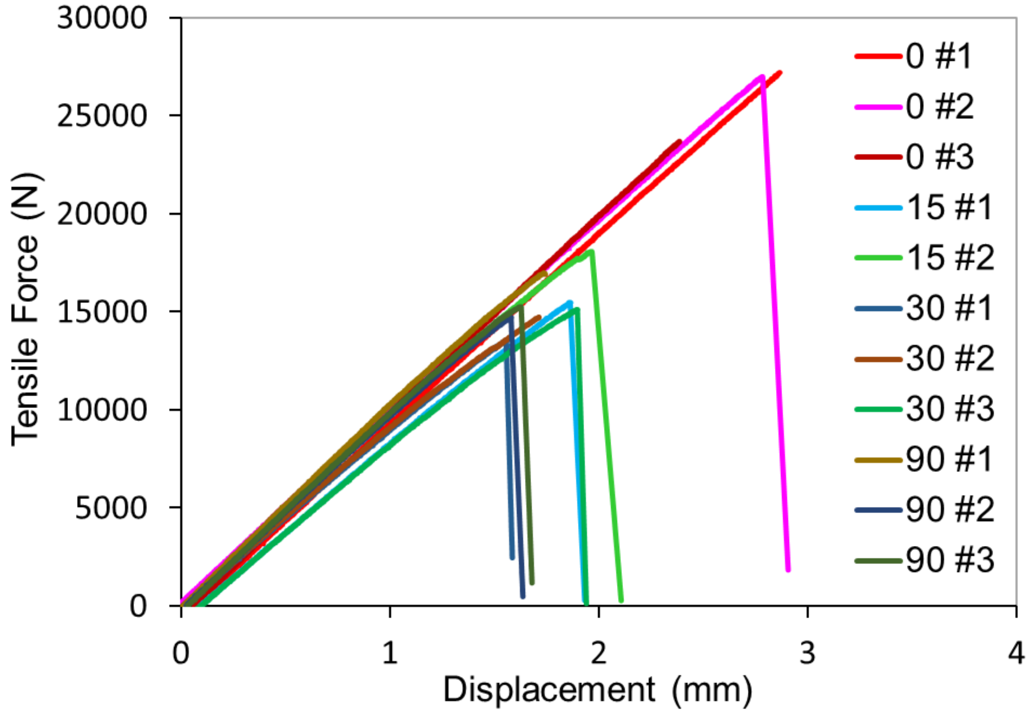

Figure 6.8. Tensile testing loading-displacement curves

The curves for all the specimens have very similar linear elastic deformation stages, which is because of the homogeneously quasi-isotropic effect due to the fiber orientations in -60º, 0º, and 60º. The similar linear elastic stage brings out the similar elastic properties for all the specimens, detail elastic properties will be discussed in the results part.

For specimens with fiber orientations in 0º and 15º, the curves tend to be a more linear-failure trend, with the nonlinear part not as obvious as that of the curves for the specimens with fiber orientations in 30º and 90º. This is due to the different amount of fiber effect compared to the matrix effect for the specimens with different fiber orientation. For specimens in 0º and 15º, more fibers are either along or close to the longitudinal specimen orientation, therefore, fibers effect counts more for the specimens during the longitudinal tensile testing. While for the specimens in 30º and 90º, fibers layout is further to the longitudinal specimen orientation, as a result, the fiber effect counts less, the matrix effect counts more, which results in the more nonlinear deformation before the failure.

The tensile failure loading for specimens in 0º is much higher than the specimens in all other orientations, which is also because there is more fiber effect in tensile strength for the specimens in 0º.

6.3.4 Tensile modulus and Poisson's ratio

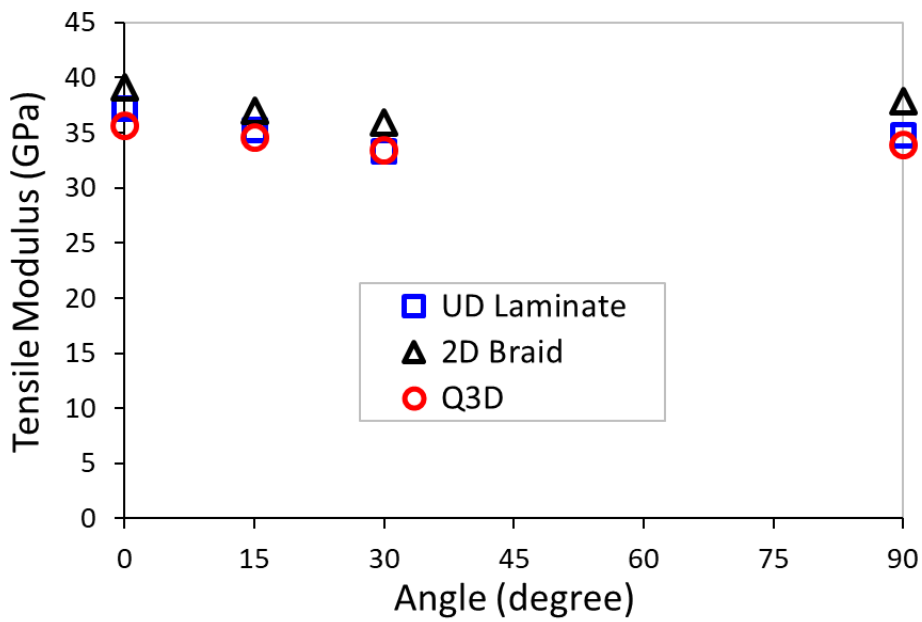

Figure 6.9. The tensile modulus of the three composite specimens with different fiber orientations

The tensile modulus for the three composite samples in different orientations is shown in Figure 6.9. The composite structures have the similar value of tensile modulus around 35

GPa, for samples in different orientations, such as in 0º, 15º, 30º, and 90º as shown in the figure. The consistent tensile modulus value in different orientations is because of the in-plane quasi-isotropic property of the composites. The composites have the fiber orientations evenly orientating in -60º, 0º, and 60º directions for 12 layers, which results in the average distribution of the orthotropic in-plane property of the unidirectional fiber tows, eventually causes the in-plane quasi-isotropic property.

For the three different composite structures, tensile modulus values are close to each other in any one of the orientations. The difference in fiber layout structures did not bring much difference in the tensile modulus of the composites. slight difference in value may be caused by the different sample quality resulted from the manufacturing process. Detail influence on the material properties caused by the manufacturing process can be further discussed.

The Poisson's ratio for the three composite samples in different orientations is shown in Figure 6.10.

Most of the Poisson's ratio values lies between 0.3~0.4, round 0.35. Similar to the tensile modulus, the Poisson ratio values have little difference between the different composite structures. For each composite structure, the Poisson's ratio values of samples in different orientations are also similar, which further reflects the quasi-isotropic elastic material properties of the composite structures.

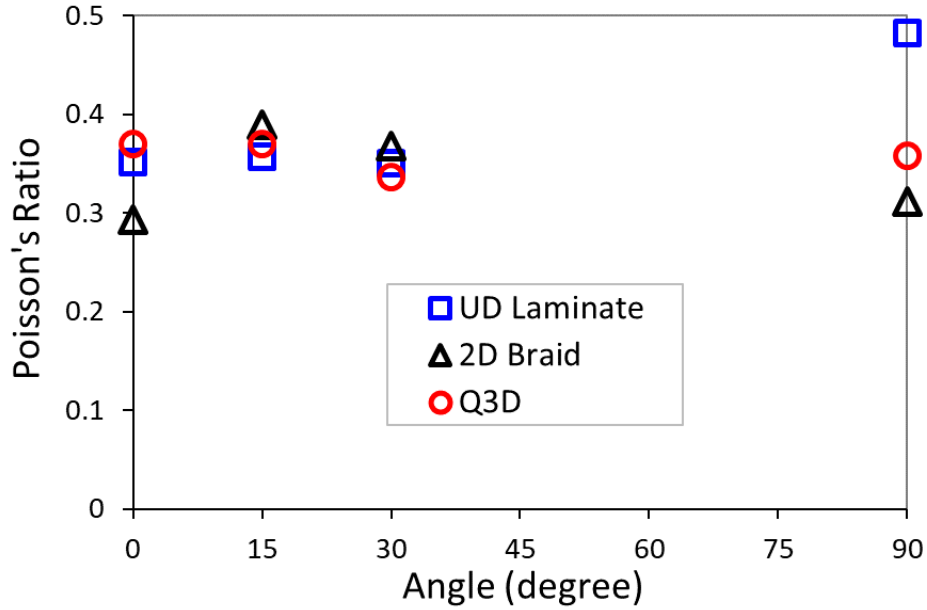

Figure 6.10 Tensile modulus of the three composite specimens with different fiber orientations

6.3.5 Tensile strength

The tensile strength of the three composite samples in different orientations is shown in Figure 6.11. For the three different composite structures, the tensile strength values are very close for specimens in the same orientation, which is because they have the same fiber layout orientations even the fiber layout structures are different. Moreover, the major contribution to the tensile strength is from the fiber since the fibers have the much higher tensile strength compared to the epoxy matrix. Therefore, the same fibers amount and orientations in the specimens resulted in the similar tensile strength. Slight difference in strength can be caused by the different out-of-plane fiber undulation and woven structure, also could be caused by the different specimen thickness, fiber volume ratios resulted from the fabrication process.

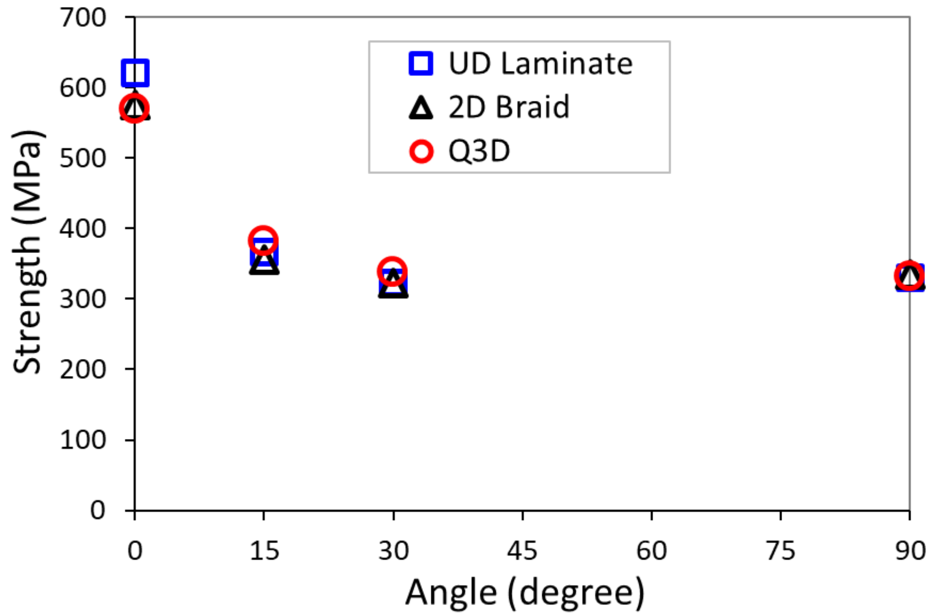

Figure 6.11 The tensile strength of the three composite specimens with different fiber orientations

For either one of the three composite structures, the tensile strength of the specimens varies in different orientations. Specimens in 0º direction have the highest tensile strength around 600 MPa. The specimens in all other directions have the much lower average tensile strength. Specimens in 15º direction have the tensile strength of about 360 MPa, while the specimens in 30º and 90º directions have almost the same level of tensile strength around 330 MPa. The difference in tensile strength is because the specimens have the biggest amount of fibers along the longitudinal specimen direction (loading direction). The carbon fiber has a much higher tensile strength than the matrix materials. Therefore, the more fibers orient in or close to the longitudinal direction of the specimens, the higher tensile strength the specimens have. This property of the tensile strength changing according to the specimen cut orientations is different from that of the elastic properties, such as the tensile modulus and the Poisson's ratio. The elastic properties are the homogenized meso-scale properties, which is because the composite materials were treated as a quasi-homogeneous fiber-matrix-mixed media. The composites have the same amount of carbon fibers in 0º, 60º, and -60º orientations, three evenly distributed orientations among the plane, which results in the quasi-isotropic in-plane properties in a homogenized way.

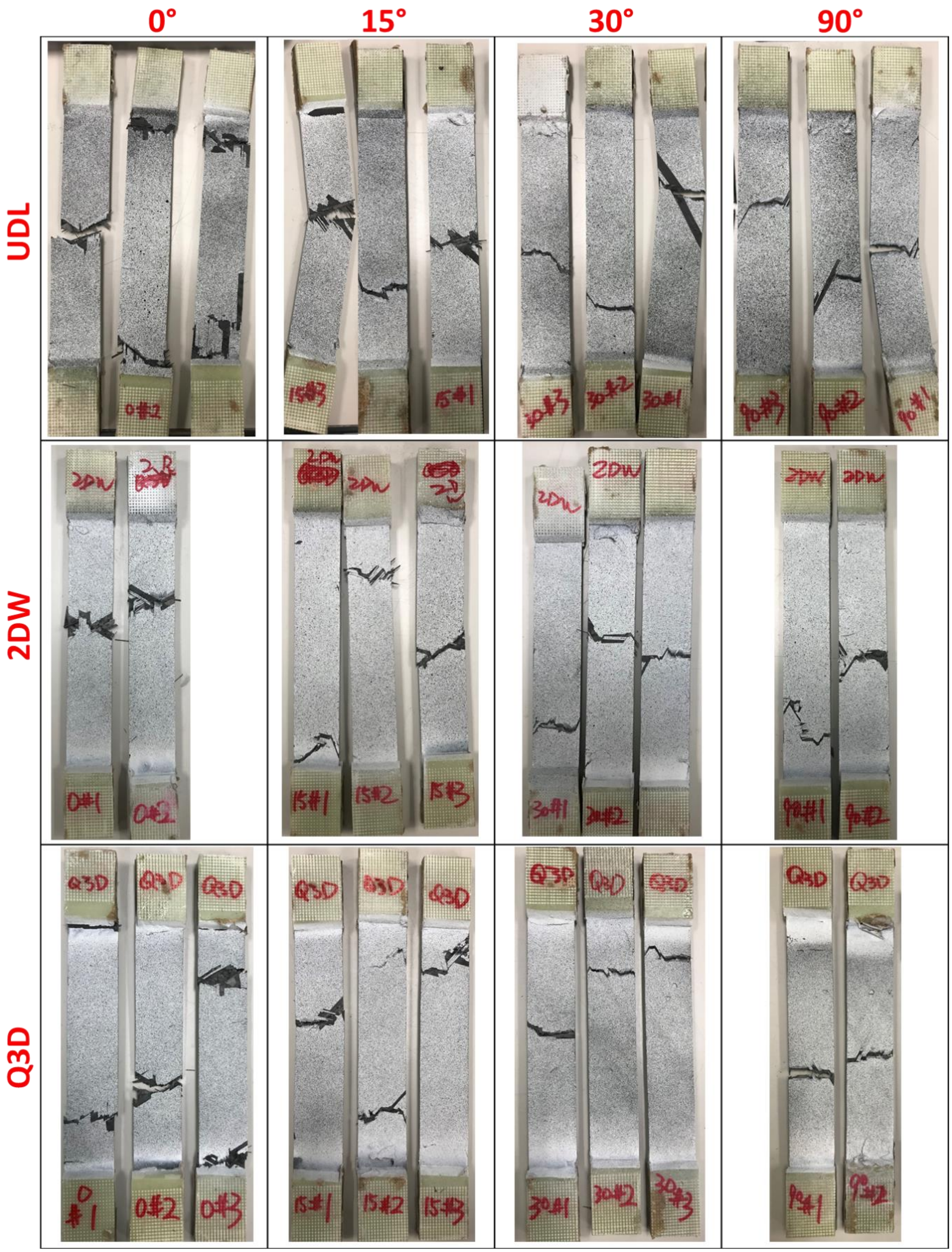

Figure 6.12 Specimens failure of the UDL, 2DW, and the Q3D composites in different orientations

6.3.6 Tensile failure analysis of UDL, 2DW, and Q3D composite materials specimens

The tensile failure specimens of the UDL, 2DW, and the Q3D composite materials in different orientations are shown in the Figure 6.12. For all three composite materials, the failure patterns between specimens in different orientations are different. The specimens in 0º direction failed with the severest specimen breakages. The specimens break through the whole sample with even two failure cross sections and a huge part of the fiber tows breakage and peeling off. The specimens broke with the strongest sound at the failure. The failure cross sections are along the lateral direction. The specimens in 15º broke also with rough failure cross sections since the fibers orientation in 15º and 45º, which is close to the longitudinal direction. The specimens in 30º and 90º have the similar failure patterns because the fiber orientations are the same due to the symmetry of the fiber orientations in [0/60/-60] composites. The specimens broke with the cleaner failure cross sections, which is because there are four layers of fibers along the 90º direction with only matrix material failure, then less severe fiber breakage and pooling out occurred. The failure cross sections aligned in the lateral direction, which is because of the axisymmetric fiber orientations along the longitudinal direction.

In the UDL specimens, failure cross sections came with both severe fibers breakage and the pealing out in between laminates, because the weak interlayer strength caused the delamination. Less delamination occurred in the 2DW specimens because there are only three interlayers in the specimen. while for the Q3D specimens, the adjacent fiber tows interlock with each other, which results in less delamination at the tensile failure, as shown in the Figure 6.12. Because of the interlayer fiber bonding difference among the three composite structures, for specimens in the same orientation, the UDL specimens have the roughest failure cross-section, the 2DW specimens have cleaner and the Q3D specimens have the cleanest failure cross sections.

6.4 Out-of-plane low-velocity impact testing

Out-of-plane low-velocity impact testing was conducted to study the impact failure mechanism and the impact resistance of the three different composite structures.

6.4.1 Impact specimen preparation

Three composite plaques were fabricated as shown in Figure 6.13. They are the UDL, 2DW, and the Q3D composite plaques. Each composite plaque was then cut into four 4*4 inches plate samples as shown in the Figure 6.13. The plate samples were used for the impact testing, with one surface painted with white flat painting as background and with black dot painting for the DIC analysis. The painting dots sizes and distribution density are determined according to the camera resolution and the DIC analysis requirements. More details about the DIC analysis experimental settings can be found in the paper [63,84].

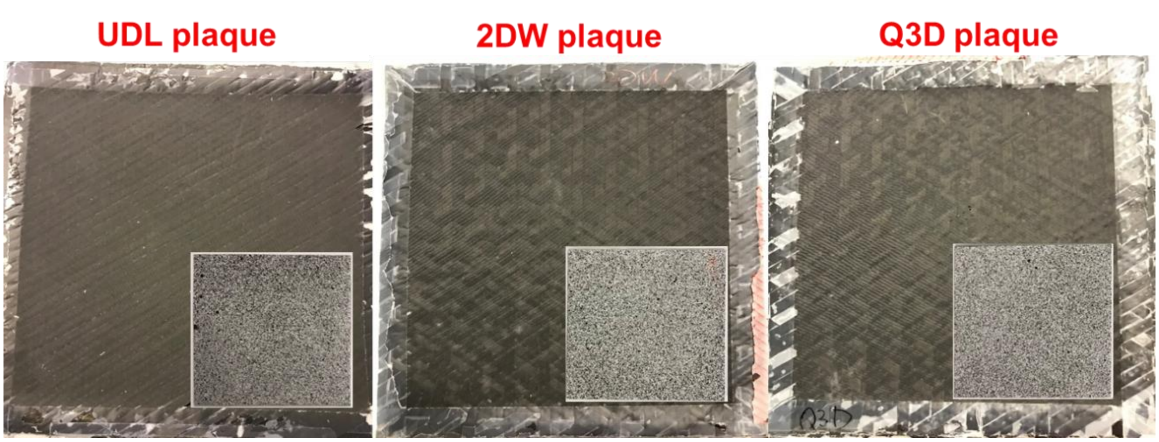

Figure 6.13 The three composite plaques with the corresponding painted impact plate samples

6.4.2 Impact testing setup

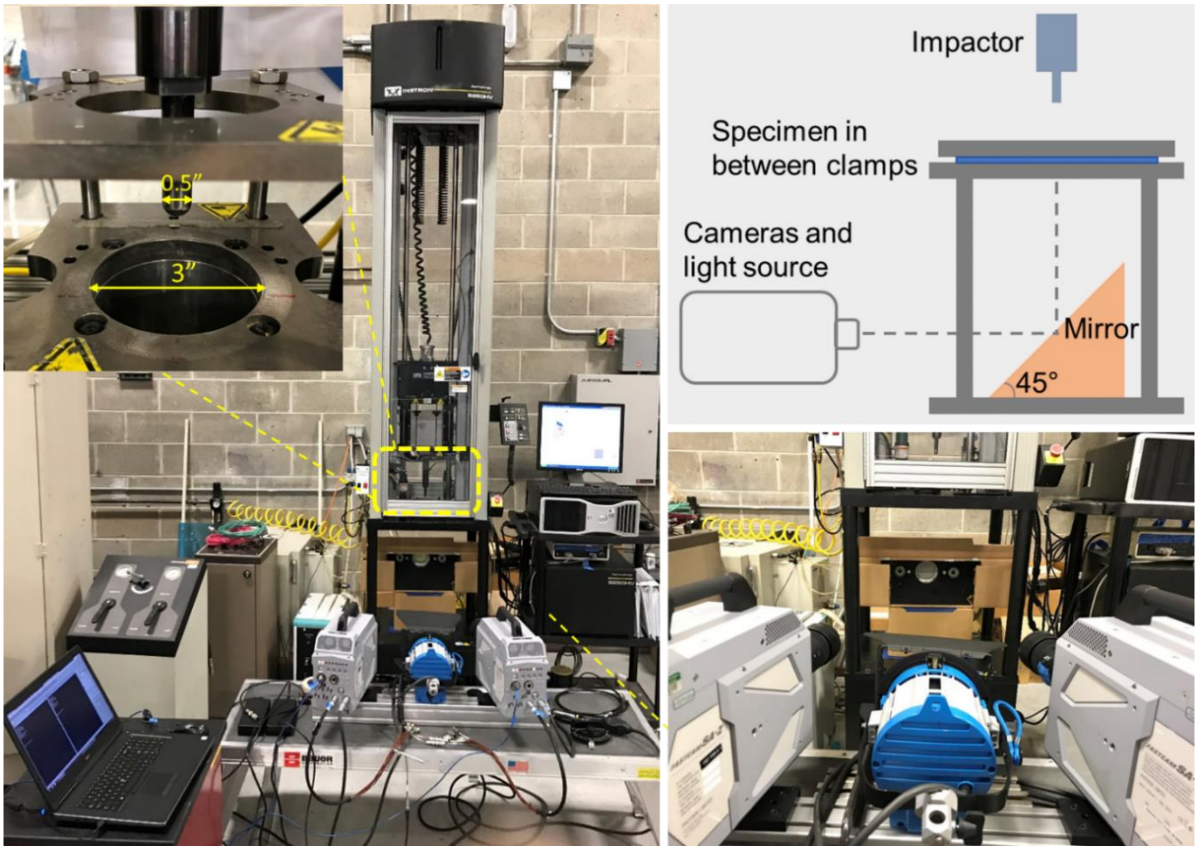

Figure 6.14 Out-of-plane impact testing setup

The impact testing settings are described in this section as shown in the Figure 6.14. The setup includes the Dynatup machine and the 3D DIC settings. The machine is the Instron Dynatup 9250 system, driven by the air system with a pressure of around 90 Psi. The impactor/drop weight has a weight of 17 kg, including the load cell attached to the bottom of the drop weight. The load cell has a tub with the tub head diameter of 0.5" is shown in the figure. Right below the load cell tub is the sample clamps. The sample clamps have the circular hole in the center with the diameter of 3" is shown in the figure. During the impact testing, the impactor is raised to a height as the setting for the impact energy or impact velocity or just impact height. The samples are placed in between the clamps and will be clamped tight by the machine after the fire button clicked. The impactor then drops freely and hit the top surface of the sample to generate the impact on the sample. The Dynatup is connected to a control system as shown in the figure. The impact loading history and the displacement of the impactor after the drop are recorded with the load cell and the laser sensors separately and saved into the control system.

The other part of the setting is the DIC system, which includes two high-speed cameras, a light source, and the video control system as shown in the Figure 6.14. The two cameras were placed in front of the Dynatup machine, with a focus angle of 20º according to the 3D DIC image quality requirements.[65] To catch the bottom surface image of the specimen that placed in the horizontal direction, a mirror with an angle of 45º was placed right below the specimen. Therefore, the bottom surface of the specimen can be reflected and caught by the cameras placed in the horizontal plane. The lateral view of the mirror settings is shown in the Figure 6.14. The light source is placed in between the cameras. With the help of the reflecting mirror, the light can be reflected and projected on the bottom surface of the specimen, as the light source of the cameras. The frequency of the high-speed cameras can reach as high as 20000/*s*, with a time step between two adjacent images as short as 50 μs, which ensures the cameras catch the detail deformation and failure process during the impact process with a very high accuracy. The cameras were controlled by the Photron FASTCAM Viewer system installed in the laptop connected as shown in the figure. The whole 3D DIC settings were purchased from the Trillion Inc.

6.4.3 Impact loading, deflection, and energy absorption of the three composites

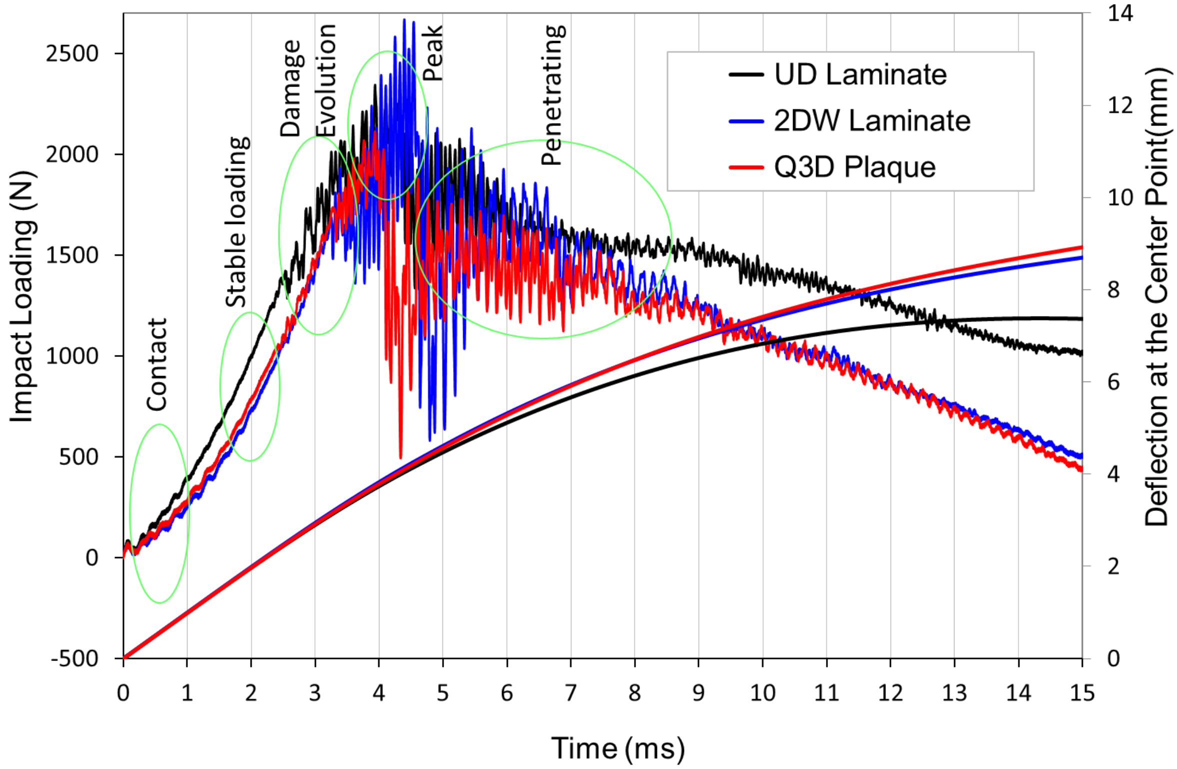

Figure 6.15 The impact loading and deflection history

The drop weight (17 kg) was set to impact on all the composite plate specimens at the impact velocity of 1 m/s. The impact loading, energy absorption, and the impactor displacement histories were recorded by the Dynatup automatically during the testing. The impactor displacement was treated as the specimen center deflection since the specimen plate is thin. The impact loading history and the deflection history of the three composite specimens center point are shown in the Figure 6.15. The loading time duration is about 15 *ms*, which includes several impact stages. The different impact stages can be obviously distinguished as follows based on the loading curve roughness in the figure:

(1) The contact process of the impactor and the sample top surface. The impact loading starts to rise from zero, then fluctuates slightly due to the further full contact of the impactor and the sample surface, which is not smoothly flat because of the fiber layout and woven undulation. The less fluctuation of the loading curve of the impact on the UDL sample exactly reflects that the UDL sample has a smoother surface with less roughness compared to the other two woven structure.

(2) The elastic stable loading process. The loading curves are relatively smooth, rise immediately till 1000 N.

(3) The damage evolution process. The damage initiates with a sudden severe fluctuation of the loading curves around 2.5 *ms*. The curves fluctuate more and more with the damage evolution. The UDL curve fluctuates much stronger than that of the 2DW and Q3D composites, which reflects the severe delamination and the in-plane fibers-matrix debonding in the UDL during the damage evolution. While for the 2DW and the Q3D, the fiber tows were woven together, therefore less delamination and debonding with smaller damage area occurred in the damage evolution process.

(4) Peak loading. The loading curves reach the peak value around 4 *ms* during this stage. The peak loadings are between 2000 N and 2500 N for the three composites. The curves drop suddenly with a huge magnitude right after the peak value, which reflects the unstable failure of the composites during the impact loading process. The unstable failure could be the fiber breakage due to the complex combination of the bending and shear loading from the impactor.

(5) Penetration process. The penetration process starts with the unstable sudden failure of the composite plates. The loading continues to rise up after the unstable drop, which reflects the late stage of the impact – penetration. Bigger contact areas occur during the penetration due to the spherical impactor head shape, more materials damage occurred. Which results in a continuous loading with a high average value but very strong fluctuation.

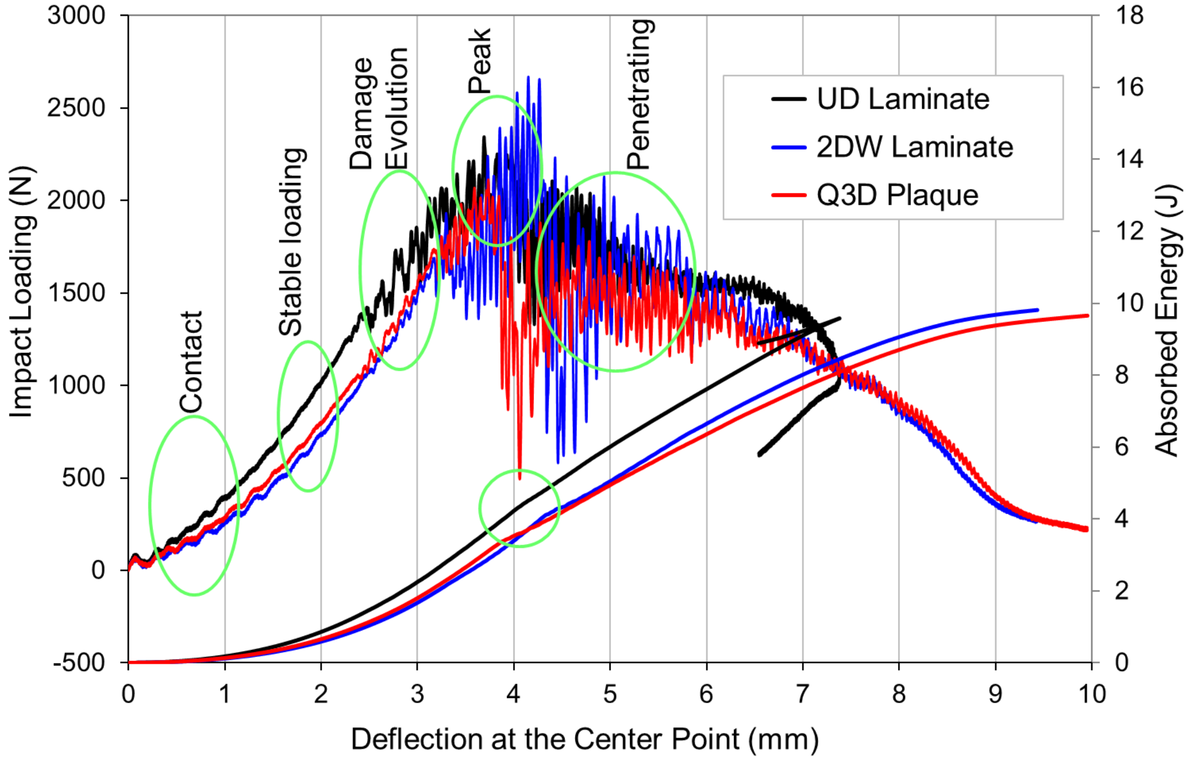

Figure 6.16 The impact Loading and absorbed energy to deflection

The impact loading and absorbed energy change according to the deflection of the composite plate sample center point are shown in the Figure 6.16. The different impact stages discussed above are also marked in the Figure 6.16.

6.4.4 3D DIC analysis setting in GOM and calibration with the loading-displacement curve.

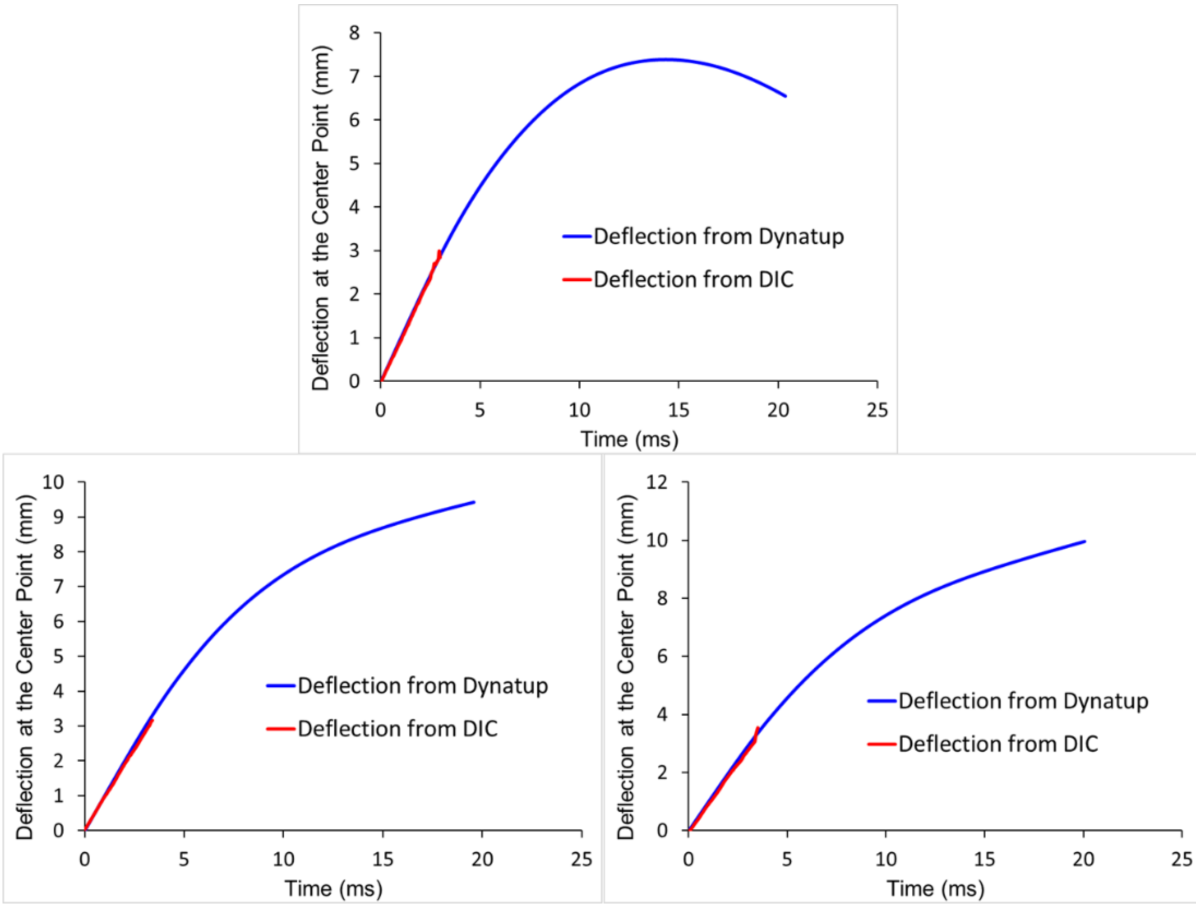

Figure 6.17 Calibration of the DIC deflection curves with Dynatup machine recorded data

The camera's settings in the 3D DIC testing were arranged as described in the Figure 6.17. To get the proper image quality for the DIC analysis with GOM, the resolution of the image is set as 512*512 pixels. In GOM software, the facet is set with a size of about 3~7 black dots. While each black dot is set with about 3~7 pixels size. The images taken at the same time with the left and right cameras were imported into the GOM software. By using the images and the 3D DIC calibration file, the GOM software then calculated the data of the displacements, strain, impact velocity and energy of the composite plate samples during the impact. All the data calculated and extracted from the GOM software is the dynamic data, with the time step of 50 μs.

The DIC analysis results were calibrated by comparing the calculated impact point deflection in the vertical direction and the impactor displacement history recorded from the DYNATUP machine. The deflection history of the plate sample center point (impact point) and the impactor displacement history curves for the three composite samples are shown in the Figure 6.17. Form the figures, the overlap as a good match of the DIC calculated deflection curves and the Impactor displacement curves can be obviously observed, for the beginning stage, when the DIC date is capable to be extracted with no severe damage to break the paintings in the image. The good match between the DIC data and the machine data is taken as an effective calibration of the DIC analysis date. More detail analysis from the DIC date will be discussed in the later sections.

6.4.5 A comparison study of the impact failure mechanism of the three composite structures

The damaged composite plate samples after the impact of 1 m/s from the 17 kg impactor are shown in the Figure 6.18. The impact damage areas on the frontal surfaces have the similar sizes for the UDL, 2DW, and the Q3D composite plates. While the damages in the back surfaces are different as shown in the Figure 6.18. Long strips of the fibers were peeled off in the ULD plate in the -60º degree, resulting in a much larger damage area in the UDL than the 2DW and the Q3D plates, which have the similar sizes of the damage areas. This is because that in the UDL plate, each layer of the lamina was connected to the other layers with the matrix interlayer. While for the other two composite structures, there are fibers interlocks between layers. Especially for the Q3D composite, the interlock of fiber tows was designed between each adjacent layer.

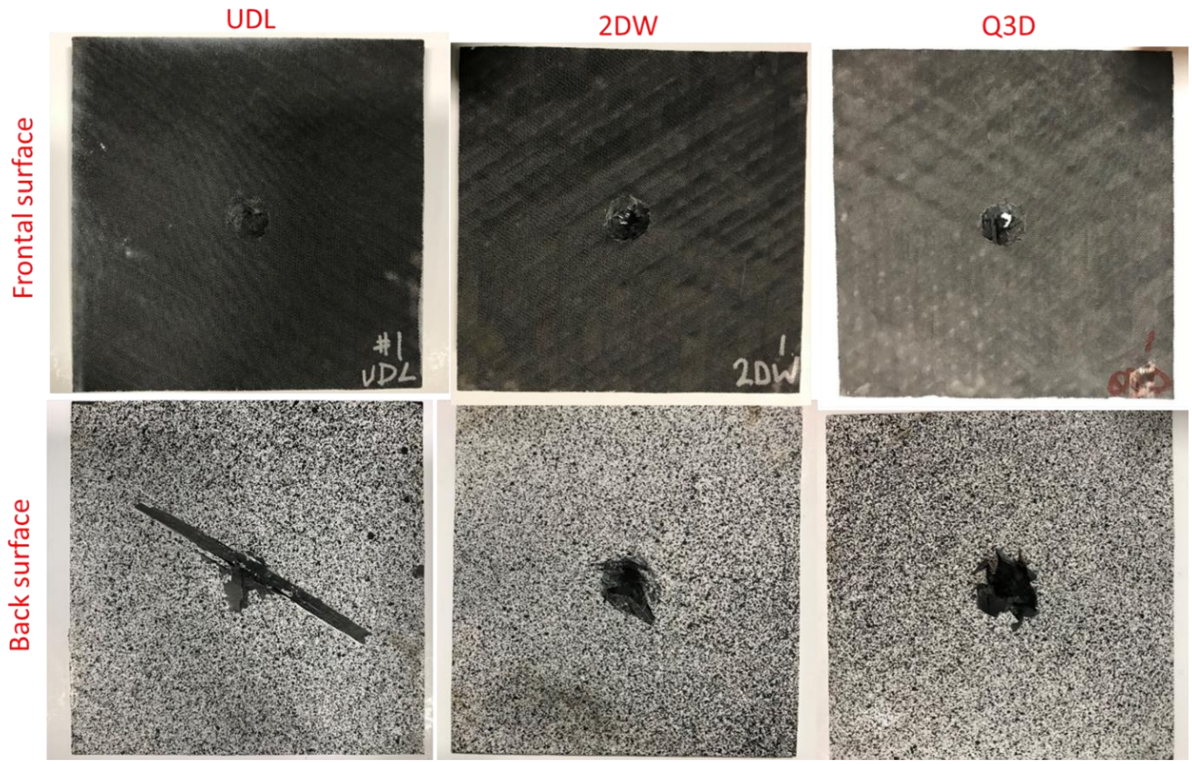

Figure 6.18 impact failure on both sides of the samples

For detail understanding of the impact damage process besides the impact failure of the composite plats as discussed above, the bottom surface damage morphologies are presented in the Figure 6.19. The images present the bottom surfaces of the UDL, 2DW and the Q3D composite plats at 5 *ms* and 8 *ms* separately. The first row of images can be treated as the initiation of the damage because at 5 *ms* the peak loading just dropped and the penetration of the impactor in the plates initiated. The damages patterns are different. For the UDL plate, the lamina fiber tow in the -60º degree started to be peeled off from the plate. For the 2DW plate, the damage initiates with a much smaller area but also align

-60º degree as the fiber orientation in the bottom surface of the plate. For the Q3D plate, the damage initiation pattern is different than the other two plates. The damage initiation pattern is shown in the figure as a star shape break up with the broken point in the center, and the radial damage propagation evenly to the edge side of the plate, which is similar to that of a brittle isotropic plate. As the damage evolution to the impact penetration to 8 *ms*, the impactor surface almost penetrated through the plate samples. The damages in the three composite plates increase in areas with the consistent damage pattern compared to the damage initiation at 5 *ms*. The bottom layer fiber strips were totally peeled off in the center area along the -60º degree for the UDL plate. The damage areas in the 2DW and Q3D plates also increased by size with the consistent damage orientation and pattern as that at 5 *ms*. The damage pattern of the Q3D plate is still similar to that of a brittle isotropic plate, which reflects that the Q3D plate has the highest local quasi-static material properties compared to the other two. Even though all the three composite plates were tested as quasi-isotropic in the global average meso-scale specimens in the tensile testing. The global quasi-isotropic elastic material properties of the three composites are due to the same amount of the fibers in the averaged-counted orientations in -60º, 0º, and 60º degrees. While the different local material properties in the damage initiation and evolution are introduced by the different fiber constructions between each adjacent layers of the composites. The damage evolution process reflected the local quasi-isotropic material properties difference in the different composite structures.

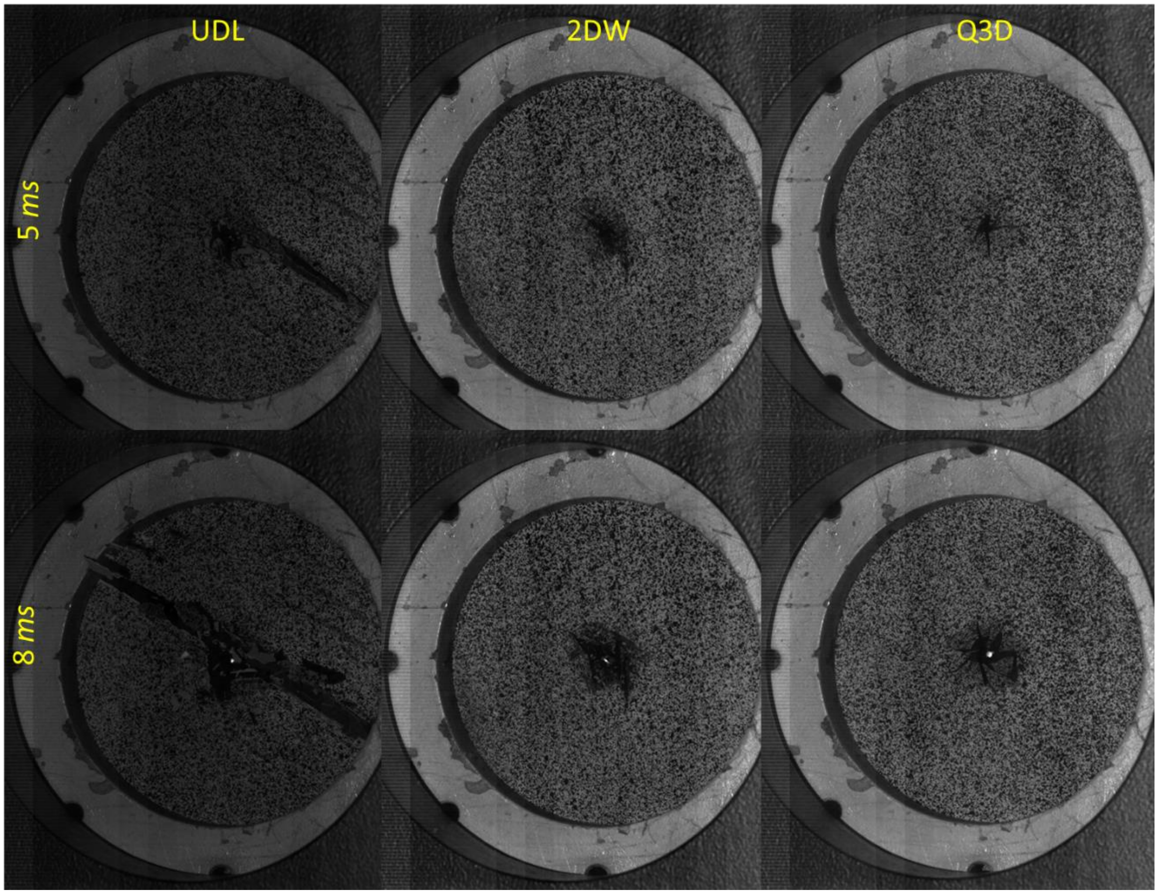

Figure 6.19 The impact failure on the bottom surface of the samples at different time steps

To further study the damage evolution mechanism difference in the three different composite plates, the major strain contours with orientation arrows of the bottom surfaces were calculated from the 3D DIC analysis, as shown in the Figure 6.20. The first row of contours presents the major strain with orientation arrows for the three composite plates at 3.8 *ms*, when the loading is almost the peak loading as shown in the Figure 6.20. The second row of contours presents the major strain at 4.5 *ms*, when the loading curves just drop right after the peak value. the major strain fields on the three composite plate surfaces are different.

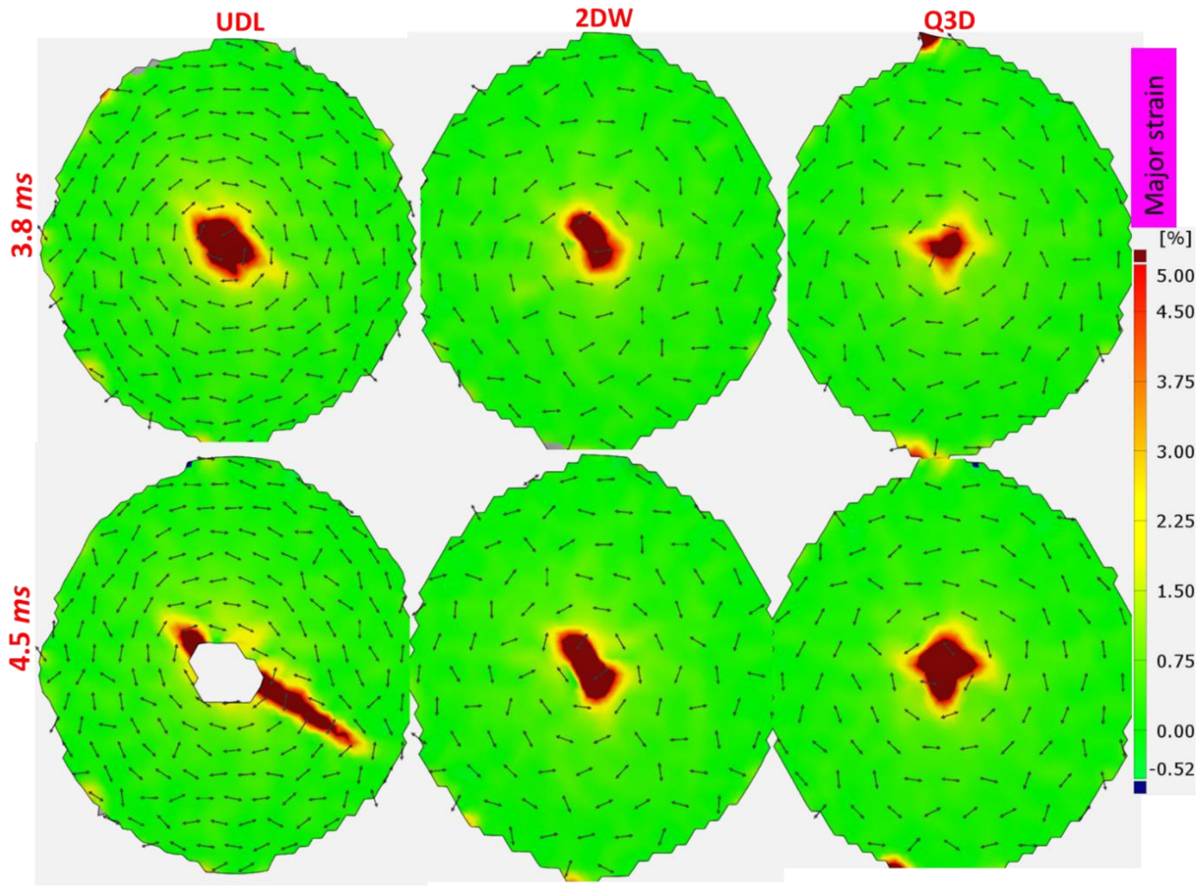

Figure 6.20 The DIC analysis of major strain on the bottom surfaces of the samples at different time steps

At the peak loading, the UDL composite has the largest major strain area with the over-scale high strain marked as dark red as shown in the Figure 6.20. The high major strain field has a shape with the convex orientation along the fiber direction of the bottom layer as shown in the figure. The 2DW plate has the smaller major strain area and the Q3D has the smallest area. The orientation of the 2DW plate high strain area is still obvious along the fiber orientation. But for the Q3D plate, the high major strain field has a centrosymmetric star-shaped area, which is similar to that of the isotropic material plate.

The difference in high major strain fields shape reflects the different local quasi-isotropic material properties of the three composite structures.

The difference in major strain fields increases severely right after the peak loading when the impact-induced penetration occurs. The impact penetration brings different damage patterns to the three composite plate samples, especially on the bottom surface as shown in the second row of contours in the Figure 6.20. For the UDL plate, the penetration causes the peeling-off of the bottom surface layer, with the enlarged high major strain field along the fiber orientation more obviously as a strip-shape. The major strain area on the 2DW plate also increases, with the similar aspect ratio along the fiber direction. For the Q3D plate, the major strain field increases with the area but still with the star-shaped centrosymmetric shape. The major strain direction is marked with the arrows for all the composite plates. The arrows orientate almost in the tangential direction of the circular plate, vertical to boundary curve of the high strain fields.

When subjected to the same impact energy, the UDL plate has the largest average damage area, the Q3D has the smallest average damage area, the 2DW is in between. Therefore, the Q3D plate has the biggest ratio of impact energy over damage area, which means under the same area of material damage, the Q3D composite can absorb higher impact energy than the UDL and 2DW composites due to the woven structure difference. To further verify the energy absorption capability of the three composite materials, multi-modes interlayer fracture/delamination testing can be performed in the future.

6.4.6 The impact failure process

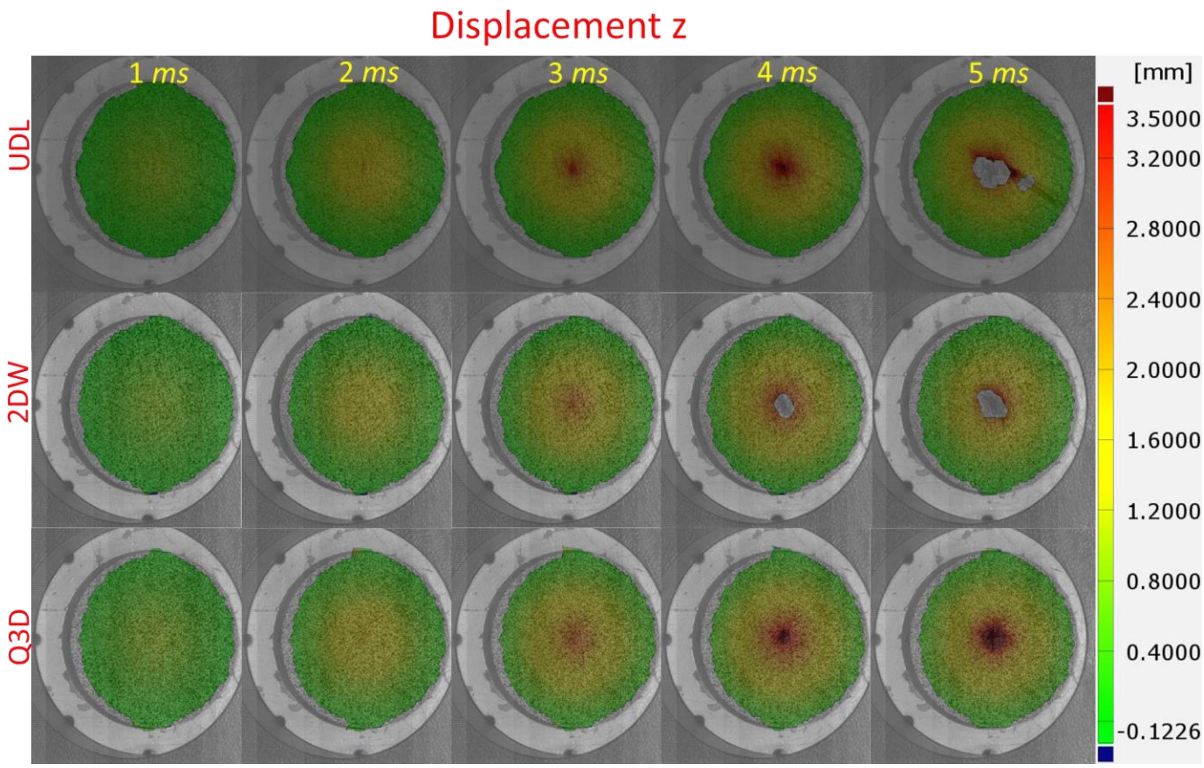

Figure 6.21 The DIC analysis of out-of-plane displacement fields during the impact process

The DIC analyzed impact displacement and strain fields for the three composites at different time steps are illustrated in the Figure 6.21~23. The impact deformation and damage process of the composite plates, and the corresponding comparisons between each composite structure can be studied from the figures.

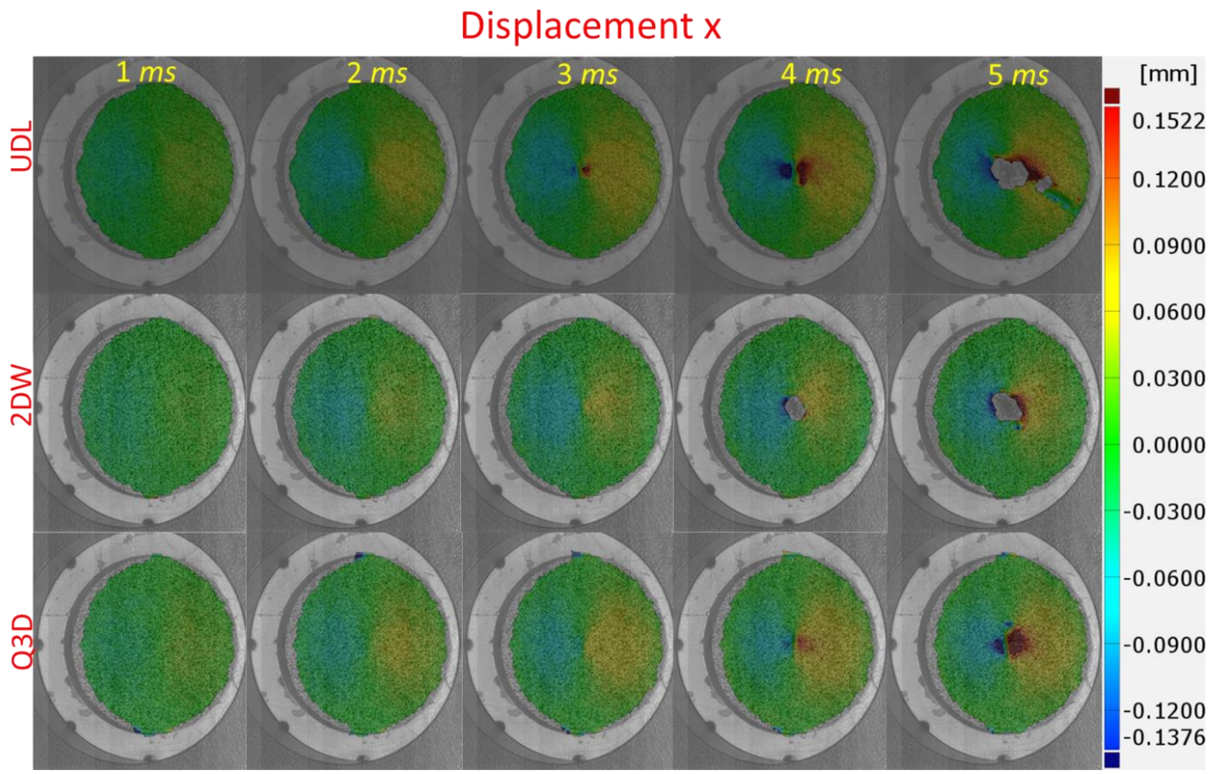

Figure 6.22 The DIC analysis of displacement fields in x-direction during the impact process

The out-of-plane displacement (displacement z) fields of the three composite plates from DIC analysis are shown in the Figure 6.21, at the time steps from 1 *ms* to 5 *ms*. For all three composite plates, the displacement z increases with the time steps. The center point of the plate has the biggest displacement increase because the impact position is the center of the plate. The displacement at the edge boundary is almost zero because the edge boundary is fixed with the clamps during the whole impact testing. The displacement contours are centrosymmetric in early impact stage such as before 3 *ms*, which reflects the homogenized quasi-isotropic in-plane material property of the three composite materials at the macro scale. After the peak loading, the contours changed. The displacement contour for Q3D plate still kept almost centrosymmetric. While for the

2DW and UDL plates, the displacement distribution around the impact center aligns with a trend to the fiber orientation of the bottom layer in -60º. The difference reflects that the Q3D composite material keeps both homogenized global and the local quasi-isotropic material property due to the fiber interlock structure between each adjacent layer. The 2DW And the UDL composite plates have the global but don't have the local quasi-isotropic material property.

The displacement x fields of the three composite plates from DIC analysis are shown in the Figure 6.22, at the time steps from 1 *ms* to 5 *ms*. The displacement x fields are different from the corresponding out-of-plane displacement fields. The contours of UDL plate present obvious orientation along the fiber orientation of the bottom surface layer, which reflects the material orthotropy of the surface layer. For the Q3D plate, the displacement x contours keep almost axisymmetric through the whole process, which reflects the quasi-isotropic material property. The 2DW plate is in between, it has the axisymmetric contours before the peak loading, as the elastic deformation process. The contours later than the peak loading have the orientation along the surface layer fiber direction, which also reflects the local orthotropic property of the damage pattern. The convex contour orientation is less obvious than that of the UDL plate contours but essentially different from that of the Q3D plate that has the highest quasi-isotropic material property in both the elastic deformation stage and the material damage stage.

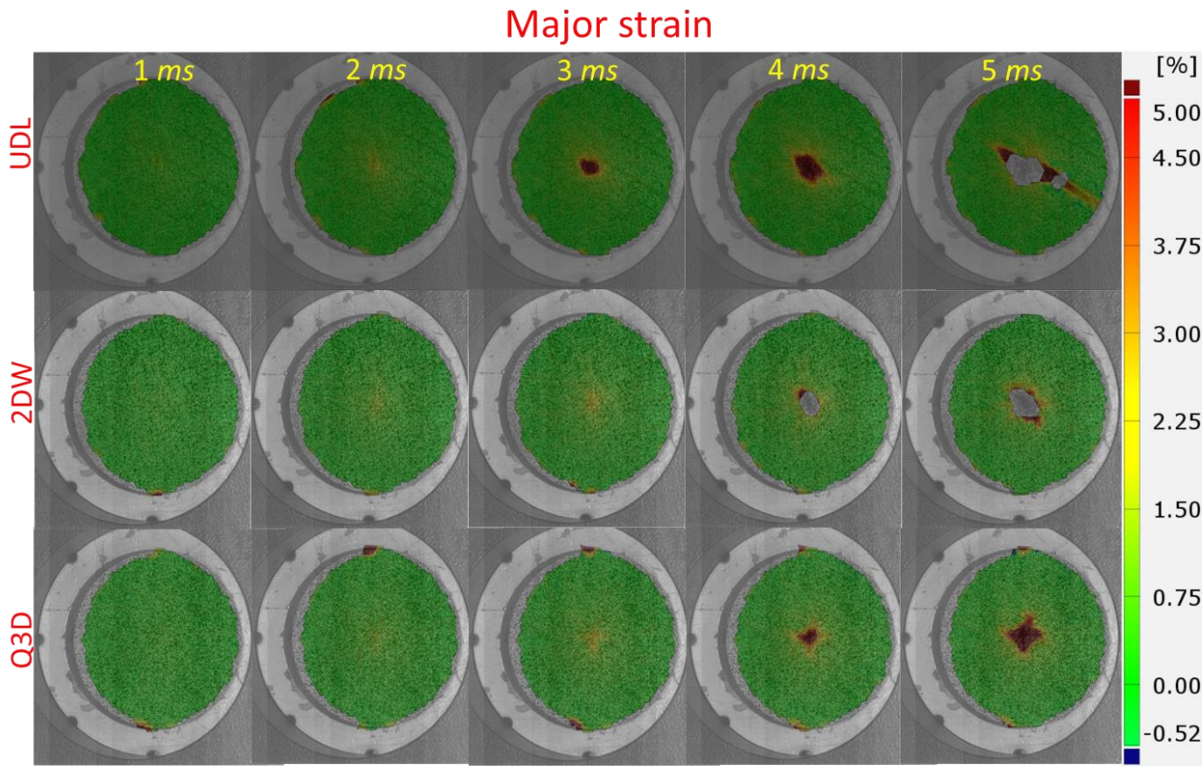

Figure 6.23 The DIC analysis of major strain fields during the impact process

The major strain fields of the three composite plates from DIC analysis are shown in the Figure 6.23, at the time steps from 1 *ms* to 5 *ms*. The major strain increases as the time step too. The UDL plate reaches the earliest high major strain (at 3 *ms*) at the center of the plate as shown in the figure. The major strain contours on the UDL and 2DW plates have the orientation along to the fiber direction of the surface layer. The major strain of the Q3D plate is close to that of the isotropic material plate. Similar results were discussed in the Figure 6.20.

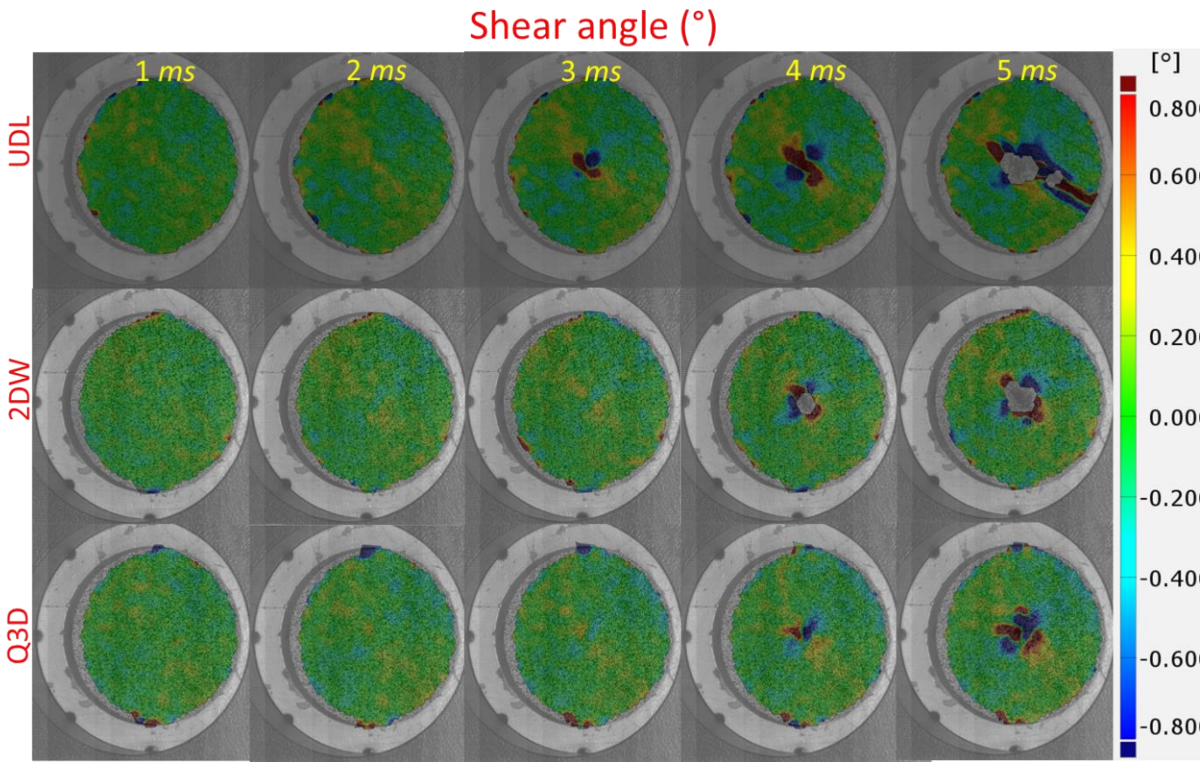

Figure 6.24 The DIC analysis of shear angle (in-plane shear strain) fields during the impact process

The in-plane shear angle (engineering shear strain) fields of the three composite plates from DIC analysis are shown in the Figure 6.24, at the time steps from 1 *ms* to 5 *ms*. Similarly, the shear strain contour of the UDL plate reaches the earliest high value at the center position with the severest orientation along the fiber direction in the surface layer. The contours on the 2DW and Q3D plates have smaller areas and less orthotropic orientation compared to that of the UDL plate. The detail contours of the shear strain evolution process are shown in the Figure 6.24.

6.5 Conclusion

Conclusions for in-plane tensile testing:

1. Quasi-isotropic in-plane material properties including tensile modulus and Poisson's ratio have been verified for the composite structures through unidirectional quasi-static tensile testing. Tensile strength decreased rapidly with the specimens oriented from 0º to other directions (15º, 30º, and 90º) as defined in the composite plaques.
2. For the three different composite structures in the same orientation, the in-plane tensile modulus, the Poisson's ratio, and the strength are similar quantitatively.
3. The influence of the different fiber structures on the composite material performance is the failure mechanism during the tensile loading process. For UDL specimens, more interlayer delamination can be found at the failure cross-section other than the fiber breakage. The Q3D specimens have the smoother failure cross section with less roughness of fiber tows peeling off, which is because the fiber layers are weaved together as an integral plaque with less interlayer failure.

Conclusions for out-of-plane low-velocity impact testing:

1. The impact stiffness and impact strength are quantitatively similar for the three composite plate samples, with the impactor of 17 kg and impact velocity of 1 m/s.
2. The different fiber layout structures influence the composite impact performances. Firstly, the different damage and failure mechanisms during the impact process. The UDL plate has the delamination on the bottom surface layer because there is no strengthening for the interlayer in the UDL plate. The penetration on the Q3D

plate is similar to that of the isotropic material plate because the Q3D plate has the best homogeneous property through-thickness direction due to the adjacent layer fiber tows interlock. Secondly, The ratio of the impact energy over the average damage area reflects that the Q3D composite has higher impact energy absorption capability per unit damage area than the UDL and the 2DW composites due to the fibers-interlock between each adjacent layer.

Chapter 7. Conclusion and Outlook

7.1 Conclusion and Contributions

In this work, the impact fracture, impact damage, and failure process have been investigated with experimental testing and peridynamic modeling and simulation, for fiber-reinforced composite materials. The specific conclusions and contributions are:

1) Identified the influence of the impact energy/loading on the fracture process, and the feasibility of 2D PD modeling in capturing the different impact fracture

The impact-induced dynamic fracture initiation and propagation in single-edge-notched PMMA beams have been analyzed. Crack velocities have the similar trend, they rise from a lower value, then reach the peak value, and then decrease till fracture. Peak velocity of the fracture in beam subjected to bigger impact loading is higher than that in the beam under smaller impact loading. The PD simulated crack velocities can match the experimental results basically at this velocity range below 300 m/s. The PD simulated crack velocity deviates from the experimental results around the peak values. The deviation increases as the experimental peak velocity increases. The simulation of higher crack velocity in different materials needs to be further investigated.

2) Developed the meso-scale PD model for orthotropic composite materials, proposed the homogenization PD modeling method, captured the impact fracture process with the fitted dynamic failure criteria in the PD model.

A new bond-based peridynamic model with the continuous material constants has been developed for orthotropic composites by using a homogenization method. Impact fracture patterns can be simulated in the unidirectional lamina with fiber oriented not only in grid-friendly directions 0º, 45º, and 90º but also in such arbitrary directions as 15º or 30º. A simultaneous crack velocity related dynamic strain energy release rate was extracted from fitted experimental results. By applying the simultaneous dynamic fracture energy formulations into the failure criteria in the PD model, the calculated dynamic fracture process and crack velocity match more accurately with the experimental results than the ones which use a constant fracture energy. The homogenization method can be applied to develop meso-scale PD models for other composite materials/structures by combining the materials' stiffness and strength in continuum mechanics system.

3) Extended the PD model for laminated composite materials, studied the impact delamination and planer damage of the laminates.

Peridynamic model for orthotropic lamina has been extended for the composite laminates. By applying the micromodulus and orientation-dependent failure criteria to PD, the out-of-plane impact damage process in the [90/θ/90] laminates can be predicted, with θ varies from 15º, 35º, 45º, 60º, to 75º. Both the matrix damage and delamination in the composite laminates have been simulated with effective patterns compared to previous experimental studies. The model can be further developed and employed to simulate multi-modes fracture and failure in laminated composite materials.

4) A systematic study of a novel Q3D carbon fiber composites' mechanical properties and impact resistant potentials through design, fabrication, and impact testing combining high-speed 3D DIC method.

Quasi-isotropic in-plane material properties including tensile modulus and Poisson's ratio have been identified for the composite structures (UDL, 2DW, and Q3D) through unidirectional quasi-static tensile testing. Tensile strength decreased rapidly with the specimens oriented from 0º, 15º, 30º, to 90º directions as defined in the composite plaques. For the three different composite structures in the same orientation, the in-plane tensile modulus, the Poisson's ratio, and the strength are similar quantitatively. The Q3D specimens have the smoother failure cross section with less roughness of fiber tows peeling off because the fiber layers are weaved together as an integral plaque with less interlayer failure.

The influence of the different fiber structures on the composite impact performance is the damage and failure mechanism during the impact process. The UDL plate has the delamination on the bottom surface layer because there is no strengthening for the interlayer in the UDL plate. The penetration on the Q3D plate is similar to that of the isotropic material plate because the Q3D plate has the best homogeneous property through thickness direction. Moreover, the Q3D composite has higher impact energy absorption capability per unit damage area than the UDL and the 2DW composites due to the fiber tows interlock between each adjacent layer. The experimental study proposes the method of material dynamic properties characterization, and the design idea of novel composite materials with high-stiffness, high-strength, and high-damage enduring potentials.

7.2 Outlook of Future Work

The homogenization method was used to develop the meso-scale PD model for composites by directly linking the laminate theory. Similarly, the method can be applied to develop the PD model for other composites with complex fiber structures, such as the woven fabric composites. The development of the PD model for the plane woven composites and other fiber composite structures will be conducted in the future.

More numerical studies with different modeling variables and simulations parameters will be conducted with the PD model and its extended versions, for obtaining effective numerical simulations of the composites in different mechanical or multi-physical loading situations.

More detail impact algorithm will be added to the 3D modeling of impact on laminates. More experimental characterization of damage and delamination process will be performed to quantitatively verify the modeling results of intralayer damage and delamination evolution process.

The experimental method of impact combining DIC (with high-speed camera) can be applied to more composite structures in different mechanical situations. For example, the compression after impact experiments (CAI) of the laminated composites. The compression buckling and shear failing can be captured with the high-speed camera with DIC in both the lateral and the frontal directions, to capture the in-plane and out-of-plane impact failure process of composites in the same time. The comprehensive details of the material dynamic failure process can help on understanding the material properties and providing significant knowledge for the development of numerical modeling and simulation.

The exploring of the advantages of the Q3D composite structures can be extended with different testing. Such as the quasi-static bending, the open mode fracture testing etc. Future experimental investigations will be conducted to identify more mechanical advantages of the Q3D composite structure, for further fiber-reinforced composite materials design on the demanding of light-weighting applications in industrial areas.

APPENDICES

Appendix A   Numerical Flowchart of a Peridynamic Program

The explicit numerical flowchart of the PD program is shown in the Figure A.1.

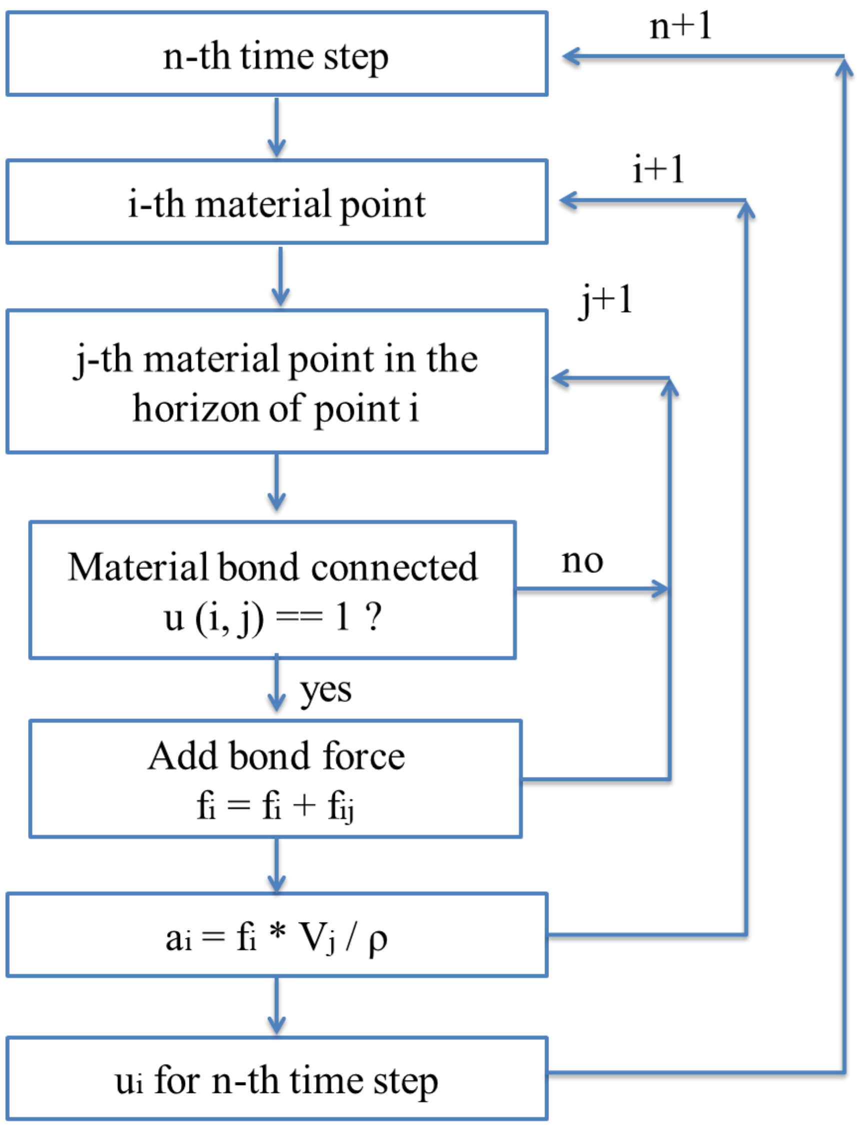

Figure A.1   The flowchart of a peridynamic program

Appendix B Impact algorithm in the Peridynamic modeling

The impact algorithm in the 2D peridynamic modeling is shown in Figure B.1.

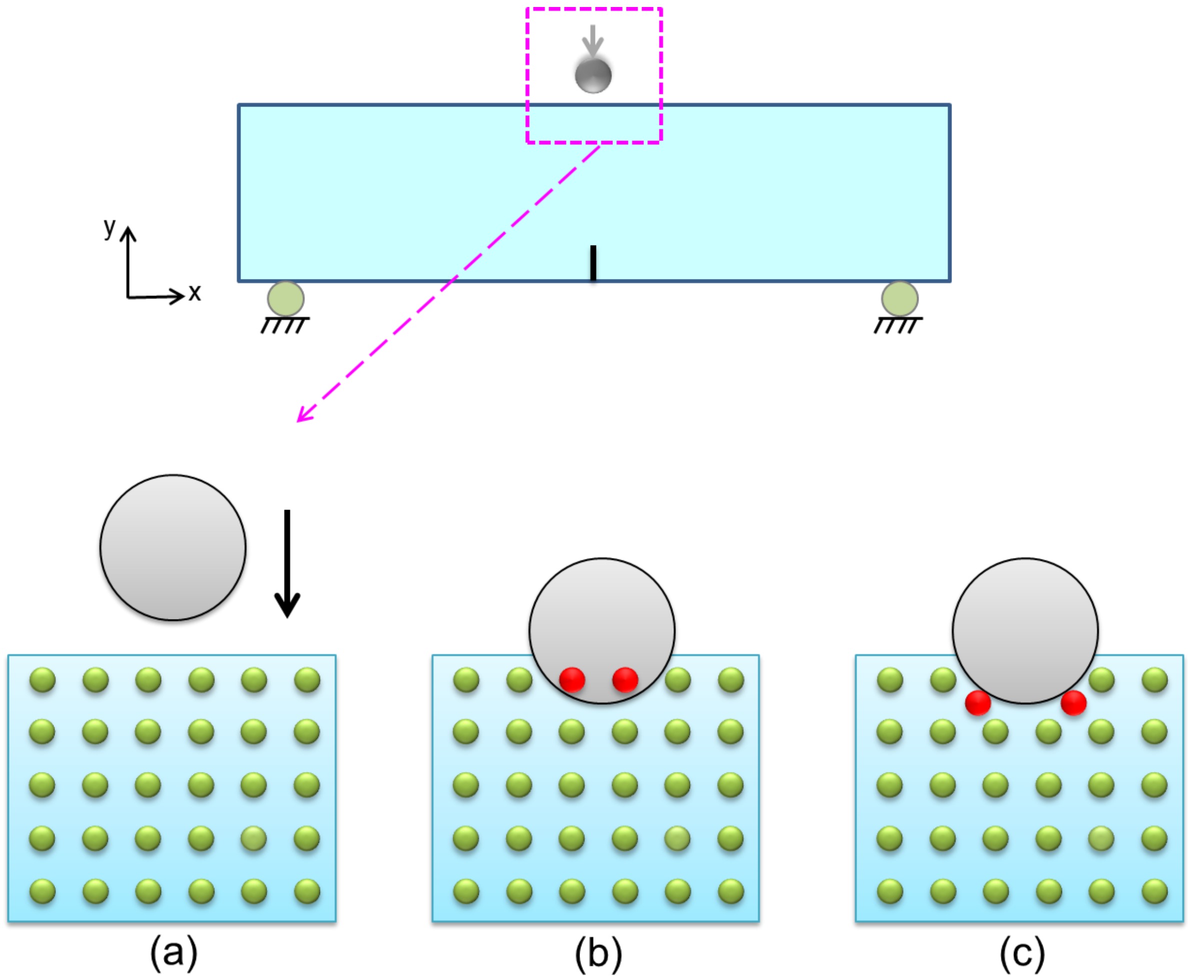

Figure B.1 Impact algorithm in the PD modeling.

For the impact algorithm in PD simulation, we set a spherical projectile with the certain size and mass toward the plate/beam according to the experimental conditions. The impactor is defined as a rigid body. As shown in Figure B.1(a), the impactor moves towards the sample in the beginning. Once the impactor contacts the sample, it penetrates inside and overlaps with the material points as shown in Figure B.1(b). To model the rigid impact, the points are forced to move to the surface of the impactor at the closest path Figure B.1(c). Thus, the contact surface is defined between the impactor and the sample at the current time step. Displacements of points at the sample surface area result in the corresponding bond forces, which interact with the impactor explicitly. Similar impact algorithm is used in the peridynamics as described by Madenci [34].

Appendix C Original notch definition in the Peridynamic modeling

The definition of the original notch at the center of the bottom surface of the beam in the 2D peridynamic modeling is shown in Figure C.1. All the material bonds crossing the original notch/crack are defined as broken, which generates the different damage ratios of the material points around the original notch as shown below.

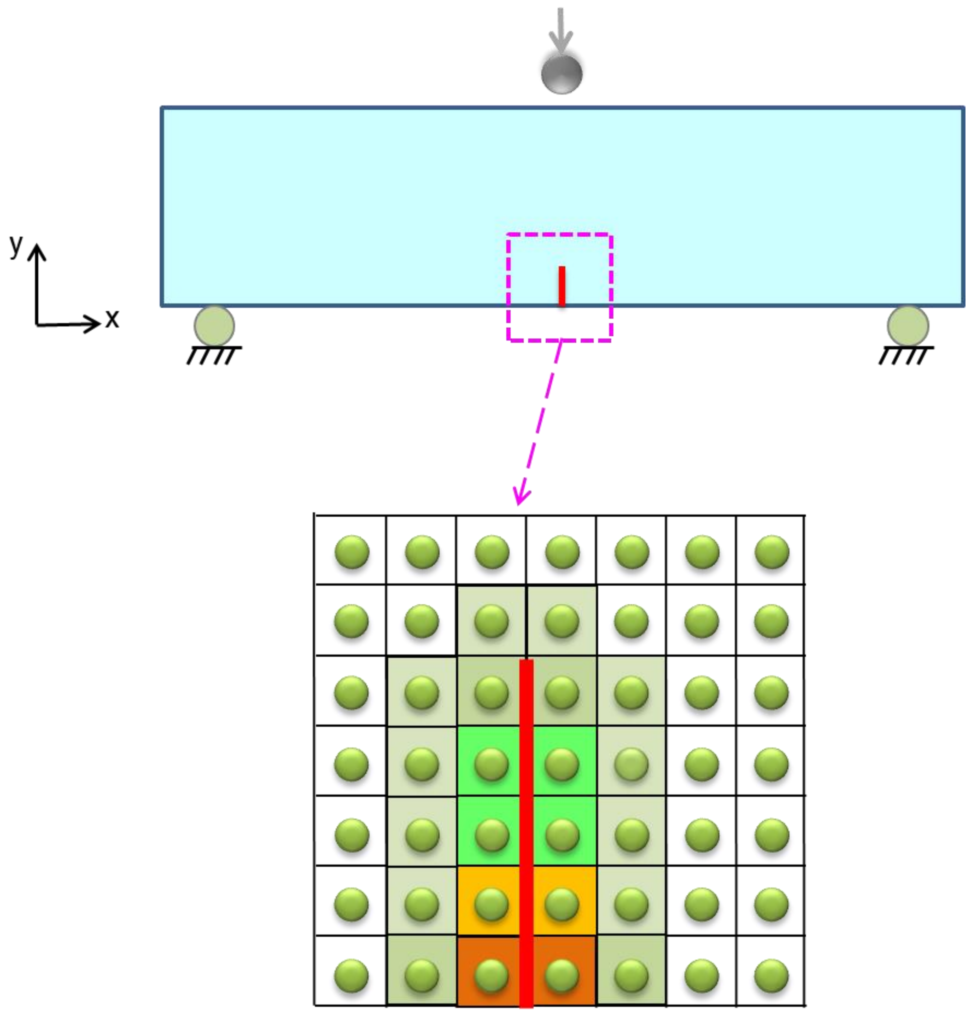

Figure C.1 Impact algorithm in the PD modeling.

Appendix D   PD Simulated Laminates Damage Evolution Process

The damage evolution process simulated with the PD model are shown as figures in this appendix. The laminates have the fiber layout of [90/15/90], [90/30/90], [90/45/90], [90/60/90], and [90/75/90]. The laminates are subjected to the mimic impact loading as described in Chapter 5.

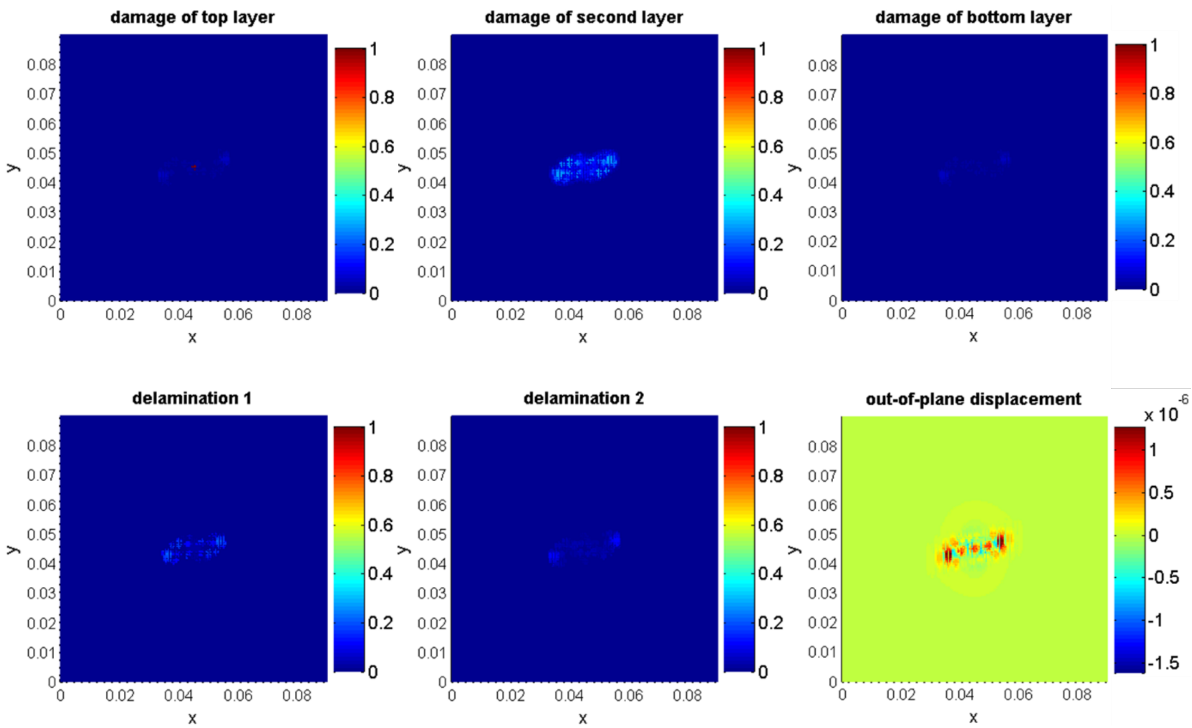

Figure D.1 Intralayer damage, delamination, and displacement field of the laminates [90/15/90] at damage initiation, after loading for 150 μs.

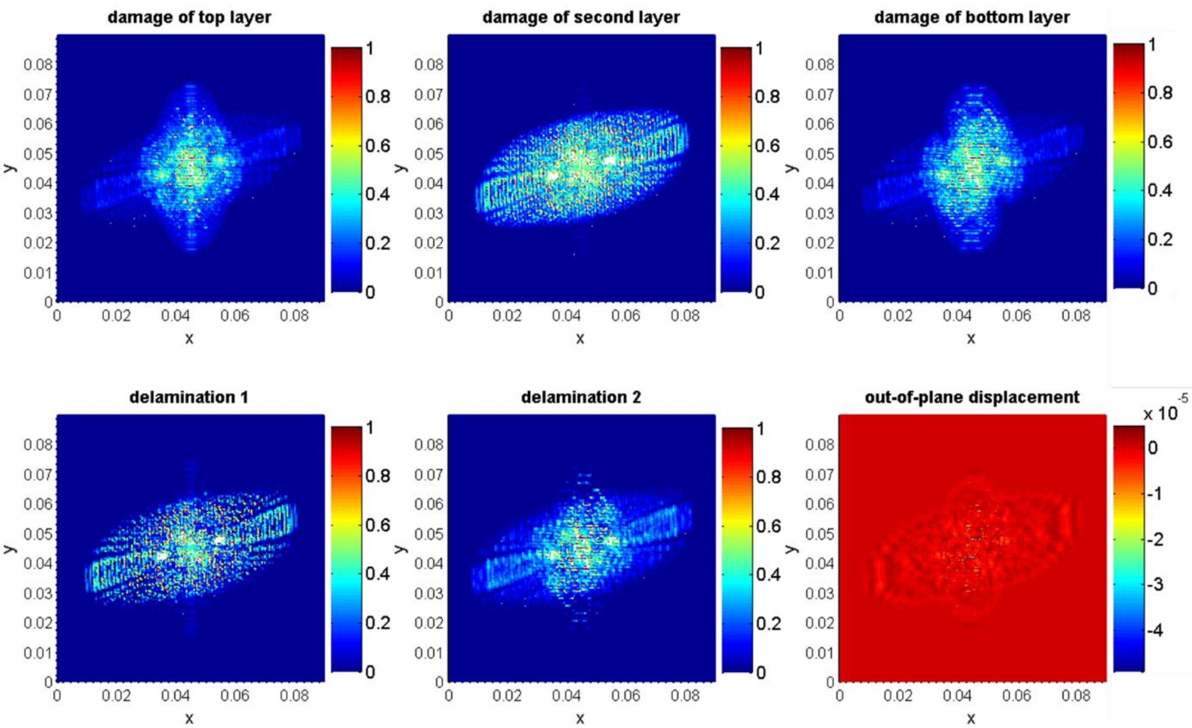

Figure D.2 Intralayer damage, delamination, and displacement field of the laminates [90/15/90] at after loading for 350 μs.

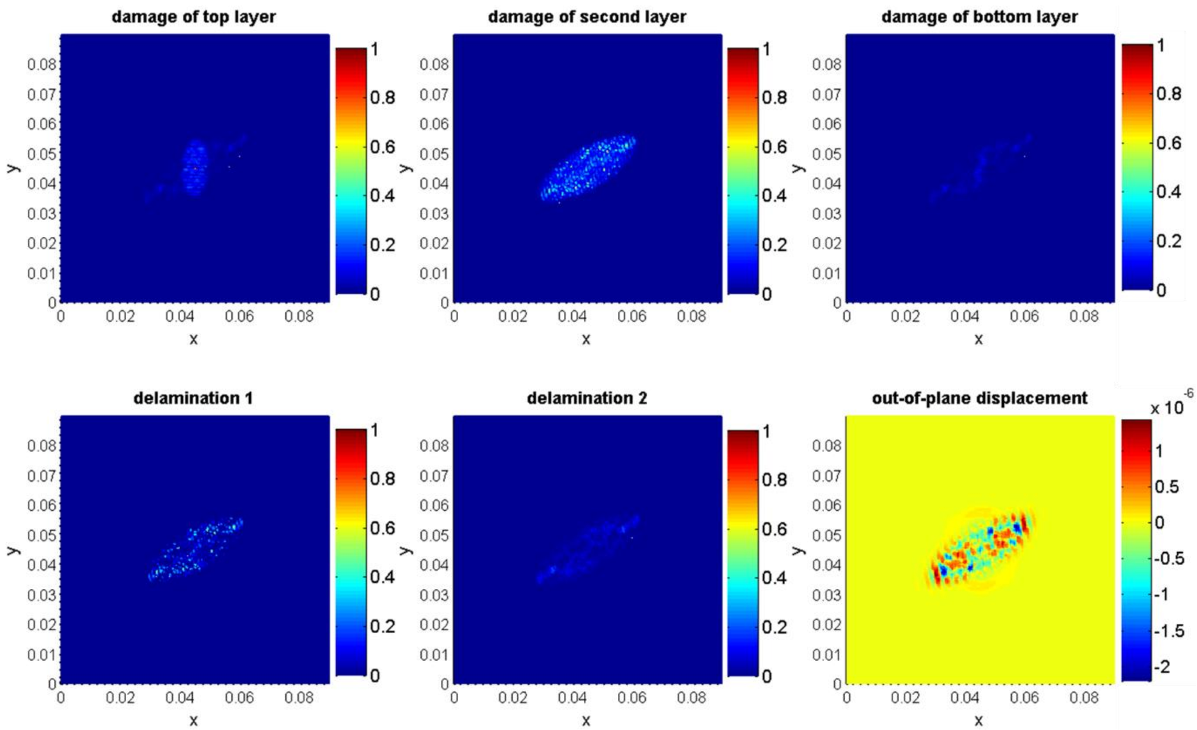

Figure D.3 Intralayer damage, delamination, and displacement field of the laminates [90/30/90] after loading for 200 μs.

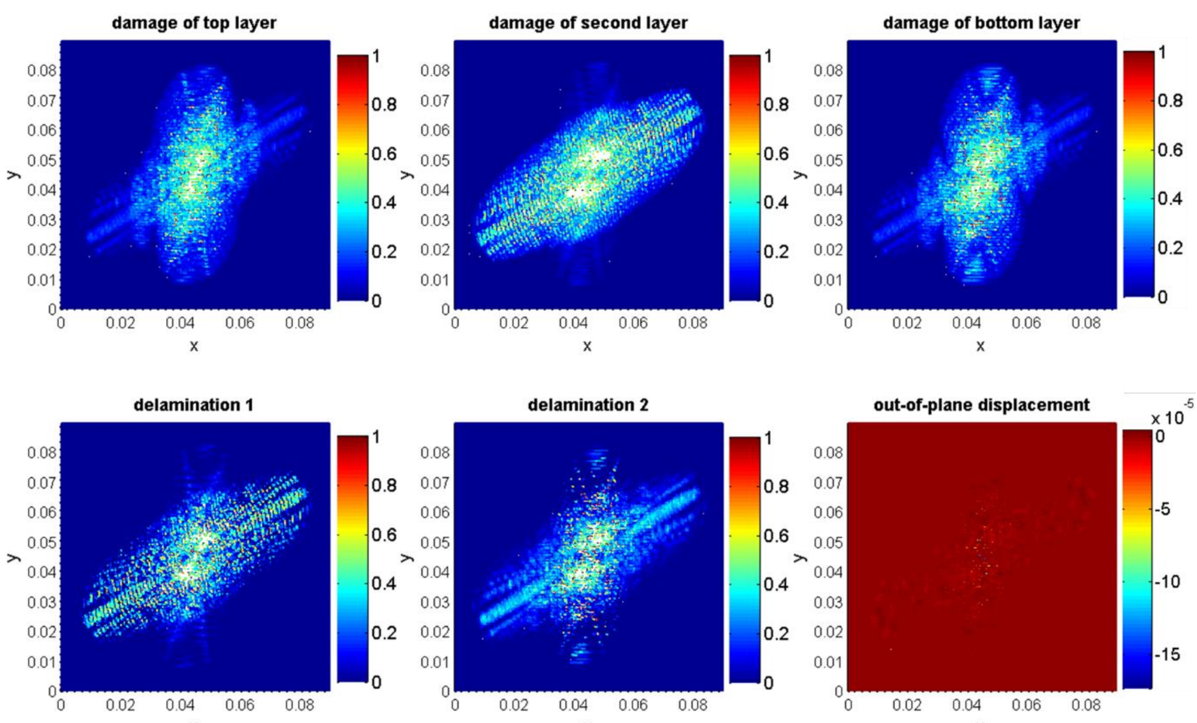

Figure D.4 Intralayer damage, delamination, and displacement field of the laminates [90/30/90] at after loading for 400 μs.

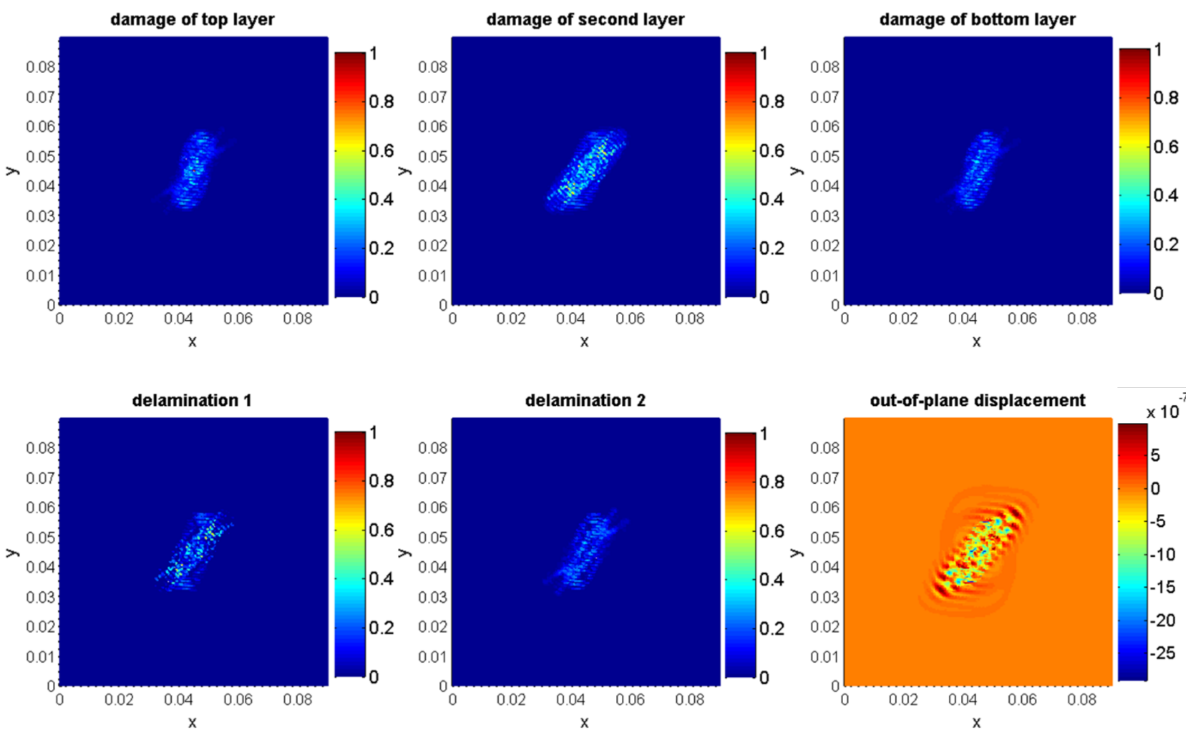

Figure D.5 Intralayer damage, delamination, and displacement field of the laminates [90/45/90] after loading for 200 μs.

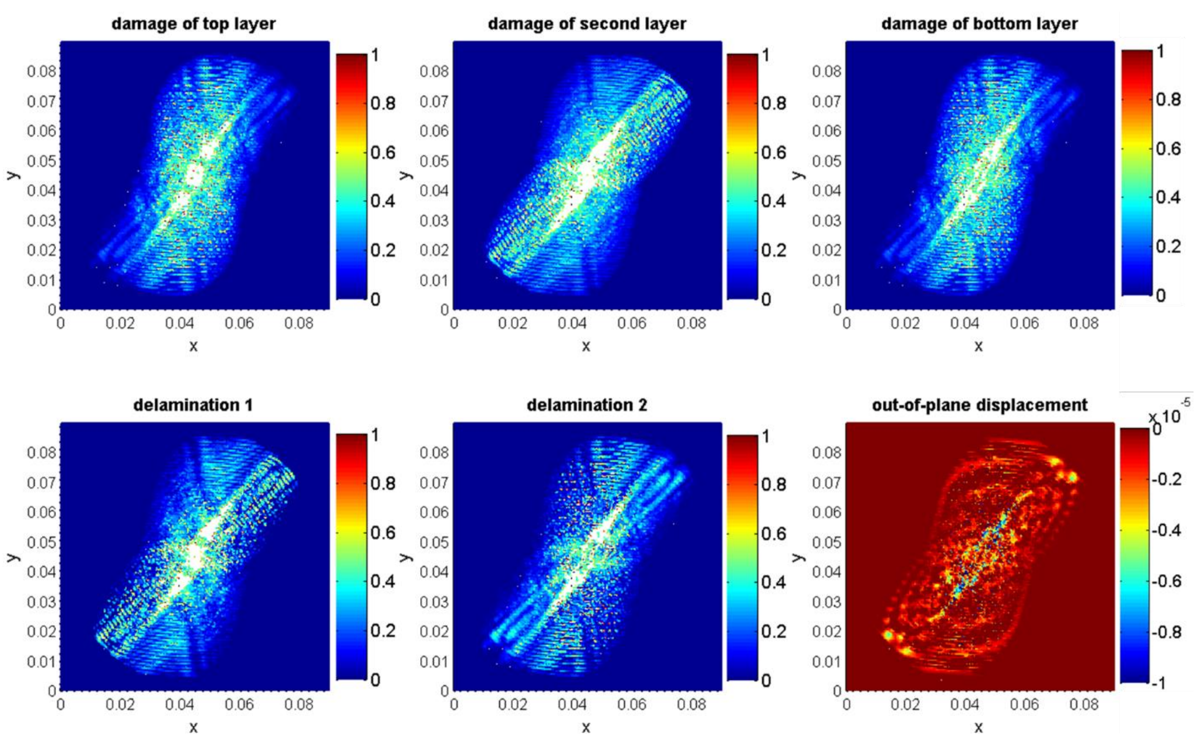

Figure D.6 Intralayer damage, delamination, and displacement field of the laminates [90/45/90] after loading for 400 μs.

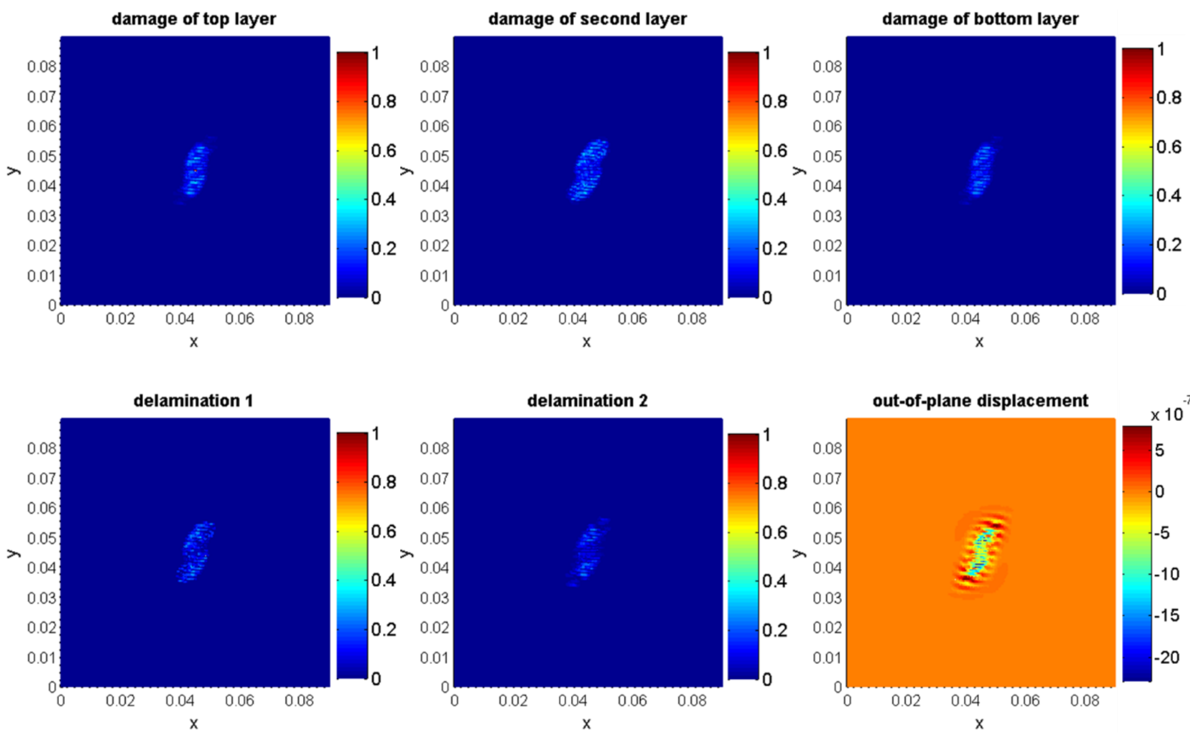

Figure D.7 Intralayer damage, delamination, and displacement field of the laminates [90/60/90] at damage initiation, after loading for 150 μs.

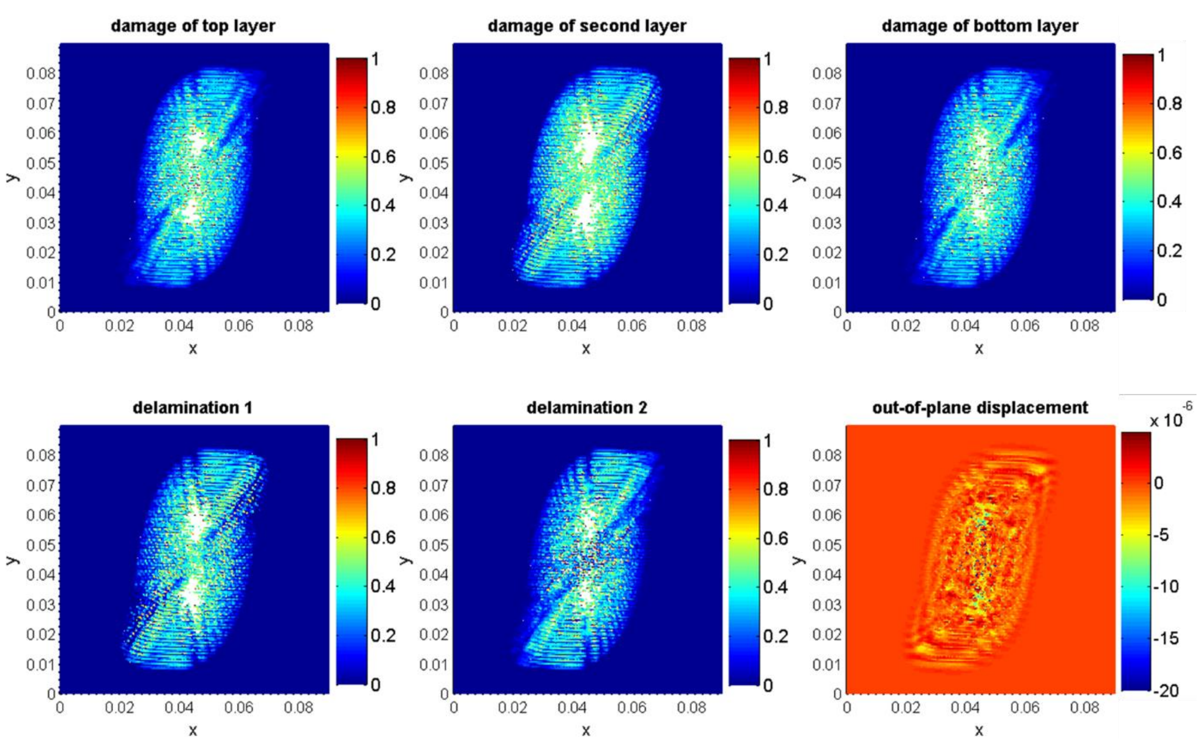

Figure D.8 Intralayer damage, delamination, and displacement field of the laminates [90/60/90] at after loading for 350 μs.

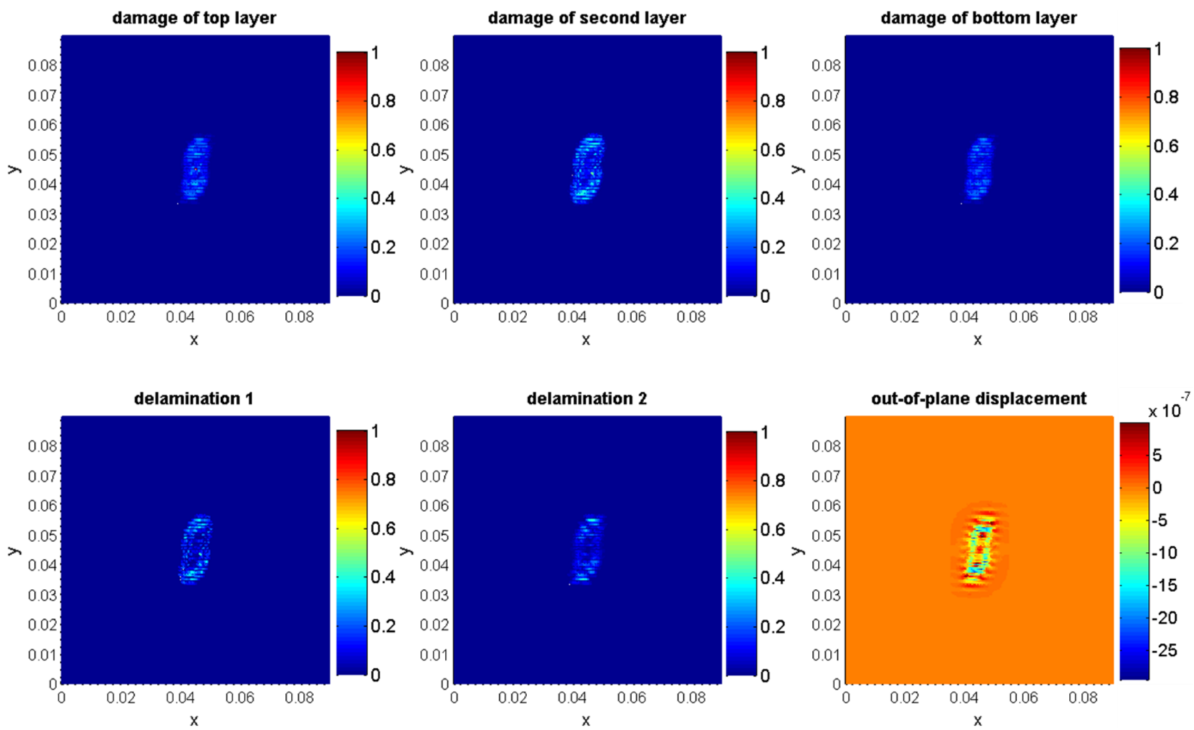

Figure D.9 Intralayer damage, delamination, and displacement field of the laminates [90/75/90] at damage initiation, after loading for 150 μs.

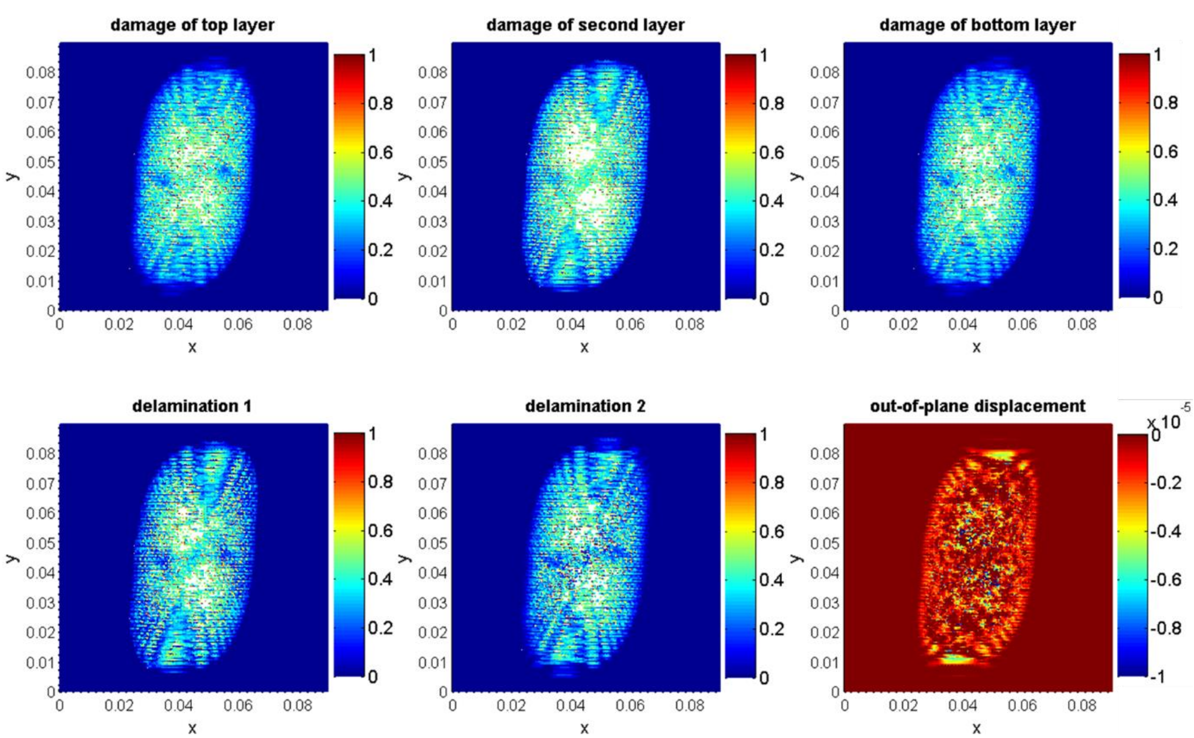

Figure D.10 Intralayer damage, delamination, and displacement field of the laminates [90/75/90] at after loading for 350 μs.

BIBLIOGRAPHY

BIBLIOGRAPHY

[1] P.K. Mallick, Fiber-Reinforced Composites: Materials, Manufacturing, and Design, Third Edition, CRC Press, 2007.

[2] A.P. Mouritz, M.K. Bannister, P.J. Falzon, K.H. Leong, Review of applications for advanced three-dimensional fibre textile composites, Compos. Part Appl. Sci. Manuf. 30 (1999) 1445–1461. doi:10.1016/S1359-835X(99)00034-2.

[3] C.G. Davila, P.P. Camanho, C.A. Rose, Failure Criteria for FRP Laminates, J. Compos. Mater. 39 (2005) 323–345. doi:10.1177/0021998305046452.

[4] J.-K. Kim, M.-L. Sham, Impact and delamination failure of woven-fabric composites, Compos. Sci. Technol. 60 (2000) 745–761. doi:10.1016/S0266-3538(99)00166-9.

[5] M.O.W. Richardson, M.J. Wisheart, Review of low-velocity impact properties of composite materials, Compos. Part Appl. Sci. Manuf. 27 (1996) 1123–1131. doi:10.1016/1359-835X(96)00074-7.

[6] W.J. Cantwell, J. Morton, The impact resistance of composite materials — a review, Composites. 22 (1991) 347–362. doi:10.1016/0010-4361(91)90549-V.

[7] C. ZWEBEN, Tensile failure of fiber composites., AIAA J. 6 (1968) 2325–2331. doi:10.2514/3.4990.

[8] S.T. Pinho, C.G. Davila, P.P. Camanho, L. Iannucci, P. Robinson, Failure Models and Criteria for FRP Under In-Plane or Three-Dimensional Stress States Including Shear Non-Linearity, 2005. http://ntrs.nasa.gov/search.jsp?R=20050110223 (accessed October 10, 2016).

[9] C.R. Schultheisz, A.M. Waas, Compressive failure of composites, part I: Testing and micromechanical theories, Prog. Aerosp. Sci. 32 (1996) 1–42. doi:10.1016/0376-0421(94)00002-3.

[10] S. Kyriakides, R. Arseculeratne, E.J. Perry, K.M. Liechti, On the compressive failure of fiber reinforced composites, Int. J. Solids Struct. 32 (1995) 689–738. doi:10.1016/0020-7683(94)00157-R.

[11] D.W. Scott, J.S. Lai, A.-H. Zureick, Creep Behavior of Fiber-Reinforced Polymeric Composites: A Review of the Technical Literature, J. Reinf. Plast. Compos. 14 (1995) 588–617. doi:10.1177/073168449501400603.

[12] J. Degrieck, W. Van Paepegem, Fatigue damage modeling of fibre-reinforced composite materials: Review, Appl. Mech. Rev. 54 (2001) 279–300. doi:10.1115/1.1381395.

[13] F. Hou, S. Hong, Characterization of R-curve behavior of translaminar crack growth in cross-ply composite laminates using digital image correlation, Eng. Fract. Mech. 117 (2014) 51–70. doi:10.1016/j.engfracmech.2014.01.010.

[14] X. Li, S.R. Hallett, M.R. Wisnom, Numerical investigation of progressive damage and the effect of layup in overheight compact tension tests, Compos. Part Appl. Sci. Manuf. 43 (2012) 2137–2150. doi:10.1016/j.compositesa.2012.03.002.

[15] S. Li, M.D. Thouless, A.M. Waas, J.A. Schroeder, P.D. Zavattieri, Use of a cohesive-zone model to analyze the fracture of a fiber-reinforced polymer–matrix composite, Compos. Sci. Technol. 65 (2005) 537–549. doi:10.1016/j.compscitech.2004.08.004.

[16] E. Oterkus, E. Madenci, O. Weckner, S. Silling, P. Bogert, A. Tessler, Combined finite element and peridynamic analyses for predicting failure in a stiffened composite curved panel with a central slot, Compos. Struct. 94 (2012) 839–850. doi:10.1016/j.compstruct.2011.07.019.

[17] B. Kilic, E. Madenci, Coupling of peridynamic theory and the finite element method, J. Mech. Mater. Struct. 5 (2010) 707–733. doi:10.2140/jomms.2010.5.707.

[18] S.A. Silling, Reformulation of elasticity theory for discontinuities and long-range forces, J. Mech. Phys. Solids. 48 (2000) 175–209. doi:10.1016/S0022-5096(99)00029-0.

[19] S.A. Silling, E. Askari, A meshfree method based on the peridynamic model of solid mechanics, Comput. Struct. 83 (2005) 1526–1535. doi:10.1016/j.compstruc.2004.11.026.

[20] S.A. Silling, M. Epton, O. Weckner, J. Xu, E. Askari, Peridynamic States and Constitutive Modeling, J. Elast. 88 (2007) 151–184. doi:10.1007/s10659-007-9125-1.

[21] ASTM, Composite Materials: Fatigue and Fracture, Fourth Volume, in: n.d.

[22] M.M. Shokrieh, M.J. Omidi, Tension behavior of unidirectional glass/epoxy composites under different strain rates, Compos. Struct. 88 (2009) 595–601. doi:10.1016/j.compstruct.2008.06.012.

[23] M.M. Shokrieh, M.J. Omidi, Investigation of strain rate effects on in-plane shear properties of glass/epoxy composites, Compos. Struct. 91 (2009) 95–102. doi:10.1016/j.compstruct.2009.04.035.

[24] D. Lee, H. Tippur, M. Kirugulige, P. Bogert, Experimental Study of Dynamic Crack Growth in Unidirectional Graphite/Epoxy Composites using Digital Image

Correlation Method and High-Speed Photography, J. Compos. Mater. (2009). doi:10.1177/0021998309342139.

[25] D. Lee, H. Tippur, P. Bogert, Quasi-static and dynamic fracture of graphite/epoxy composites: An optical study of loading-rate effects, Compos. Part B Eng. 41 (2010) 462–474. doi:10.1016/j.compositesb.2010.05.007.

[26] D. Lee, H.V. Tippur, B.J. Jensen, P.B. Bogert, Tensile and Fracture Characterization of PETI-5 and IM7/PETI-5 Graphite/Epoxy Composites Under Quasi-Static and Dynamic Loading Conditions, J. Eng. Mater. Technol. 133 (2011) 021015–021015. doi:10.1115/1.4003487.

[27] D. Lee, H. Tippur, P. Bogert, Dynamic fracture of graphite/epoxy composites stiffened by buffer strips: An experimental study, Compos. Struct. 94 (2012) 3538–3545. doi:10.1016/j.compstruct.2012.05.032.

[28] R.M. Sencu, Z.J. Yang, Y.C. Wang, 5 - From micro to macro: Simulating crack propagation in carbon fibre composites, in: P.W.R. Beaumont, C.S. Hodzic (Eds.), Struct. Integr. Durab. Adv. Compos., Woodhead Publishing, 2015: pp. 105–124. http://www.sciencedirect.com/science/article/pii/B9780081001370000055 (accessed September 14, 2015).

[29] S.R. Hallett, B.G. Green, W.G. Jiang, M.R. Wisnom, An experimental and numerical investigation into the damage mechanisms in notched composites, Compos. Part Appl. Sci. Manuf. 40 (2009) 613–624. doi:10.1016/j.compositesa.2009.02.021.

[30] L.M.A. Cahill, S. Natarajan, S.P.A. Bordas, R.M. O'Higgins, C.T. McCarthy, An experimental/numerical investigation into the main driving force for crack propagation in uni-directional fibre-reinforced composite laminae, Compos. Struct. 107 (2014) 119–130. doi:10.1016/j.compstruct.2013.05.039.

[31] E.J. Pineda, A.M. Waas, A Thermodynamically-Based Mesh Objective Work Potential Theory for Predicting Intralaminar Progressive Damage and Failure in Fiber-Reinforced Laminates, in: Honolulu, HI, United States, 2012. http://ntrs.nasa.gov/search.jsp?R=20120012876 (accessed May 8, 2016).

[32] B. Kilic, A. Agwai, E. Madenci, Peridynamic theory for progressive damage prediction in center-cracked composite laminates, Compos. Struct. 90 (2009) 141–151. doi:10.1016/j.compstruct.2009.02.015.

[33] E. Oterkus, E. Madenci, Peridynamic analysis of fiber-reinforced composite materials, J. Mech. Mater. Struct. 7 (2012) 45–84. doi:10.2140/jomms.2012.7.45.

[34] E. Madenci, E. Oterkus, Peridynamic Theory and Its Applications, Springer, New York, 2014.

[35] W. Hu, Y.D. Ha, F. Bobaru, Peridynamic model for dynamic fracture in unidirectional fiber-reinforced composites, Comput. Methods Appl. Mech. Eng. 217–220 (2012) 247–261. doi:10.1016/j.cma.2012.01.016.

[36] Q. Bing, C.T. Sun, Modeling and testing strain rate-dependent compressive strength of carbon/epoxy composites, Compos. Sci. Technol. 65 (2005) 2481–2491. doi:10.1016/j.compscitech.2005.06.012.

[37] J. Tsai, C.T. Sun, Constitutive model for high strain rate response of polymeric composites, Compos. Sci. Technol. 62 (2002) 1289–1297. doi:10.1016/S0266-3538(02)00064-7.

[38] Z. Kutlu, F.-K. Chang, Modeling Compression Failure of laminated Composites Containing Multiple Through-the-Width Delaminations, J. Compos. Mater. 26 (1992) 350–387. doi:10.1177/002199839202600303.

[39] P.F. Liu, J.Y. Zheng, Recent developments on damage modeling and finite element analysis for composite laminates: A review, Mater. Des. 31 (2010) 3825–3834. doi:10.1016/j.matdes.2010.03.031.

[40] B. Kilic, E. Madenci, Structural stability and failure analysis using peridynamic theory, Int. J. Non-Linear Mech. 44 (2009) 845–854. doi:10.1016/j.ijnonlinmec.2009.05.007.

[41] D. Huang, Q. Zhang, P. Qiao, Damage and progressive failure of concrete structures using non-local peridynamic modeling, Sci. China Technol. Sci. 54 (2011) 591–596. doi:10.1007/s11431-011-4306-3.

[42] F. Shen, Q. Zhang, D. Huang, Damage and Failure Process of Concrete Structure under Uniaxial Compression Based on Peridynamics Modeling, Math. Probl. Eng. 2013 (2013) e631074. doi:10.1155/2013/631074.

[43] Y. Wang, X. Zhou, X. Xu, Numerical simulation of propagation and coalescence of flaws in rock materials under compressive loads using the extended non-ordinary state-based peridynamics, Eng. Fract. Mech. 163 (2016) 248–273. doi:10.1016/j.engfracmech.2016.06.013.

[44] Y.L. Hu, E. Madenci, Bond-based peridynamic modeling of composite laminates with arbitrary fiber orientation and stacking sequence, Compos. Struct. 153 (2016) 139–175. doi:10.1016/j.compstruct.2016.05.063.

[45] S. Agrawal, K.K. Singh, P.K. Sarkar, Impact damage on fibre-reinforced polymer matrix composite – A review, J. Compos. Mater. (2013) 0021998312472217. doi:10.1177/0021998312472217.

[46] S. Abrate, Impact on Laminated Composite Materials, Appl. Mech. Rev. 44 (1991) 155–190. doi:10.1115/1.3119500.

[47] H.Y. Choi, F.-K. Chang, A Model for Predicting Damage in Graphite/Epoxy Laminated Composites Resulting from Low-Velocity Point Impact, J. Compos. Mater. 26 (1992) 2134–2169. doi:10.1177/002199839202601408.

[48] H.Y. Choi, H.-Y.T. Wu, F.-K. Chang, A New Approach toward Understanding Damage Mechanisms and Mechanics of Laminated Composites Due to Low-Velocity Impact: Part II—Analysis, J. Compos. Mater. 25 (1991) 1012–1038. doi:10.1177/002199839102500804.

[49] O.T. Topac, B. Tasdemir, B. Gozluklu, E. Gurses, D. Coker, Experimental and Computational Investigation of Out-of-Plane Low Velocity Impact Behavior of CFRP Composite Plates, in: SpringerLink, Springer International Publishing, n.d.: pp. 9–16. doi:10.1007/978-3-319-21611-9_2.

[50] S. Takeda, S. Minakuchi, Y. Okabe, N. Takeda, Delamination monitoring of laminated composites subjected to low-velocity impact using small-diameter FBG sensors, Compos. Part Appl. Sci. Manuf. 36 (2005) 903–908. doi:10.1016/j.compositesa.2004.12.005.

[51] C. Bouvet, S. Rivallant, J.J. Barrau, Low velocity impact modeling in composite laminates capturing permanent indentation, Compos. Sci. Technol. 72 (2012) 1977–1988. doi:10.1016/j.compscitech.2012.08.019.

[52] D. Feng, F. Aymerich, Damage prediction in composite sandwich panels subjected to low-velocity impact, Compos. Part Appl. Sci. Manuf. 52 (2013) 12–22. doi:10.1016/j.compositesa.2013.04.010.

[53] R. Karakuzu, E. Erbil, M. Aktas, Impact characterization of glass/epoxy composite plates: An experimental and numerical study, Compos. Part B Eng. 41 (2010) 388–395. doi:10.1016/j.compositesb.2010.02.003.

[54] V. Tita, J. de Carvalho, D. Vandepitte, Failure analysis of low velocity impact on thin composite laminates: Experimental and numerical approaches, Compos. Struct. 83 (2008) 413–428. doi:10.1016/j.compstruct.2007.06.003.

[55] A. Turon, P.P. Camanho, J. Costa, C.G. Dávila, A damage model for the simulation of delamination in advanced composites under variable-mode loading, Mech. Mater. 38 (2006) 1072–1089. doi:10.1016/j.mechmat.2005.10.003.

[56] J.P. Hou, N. Petrinic, C. Ruiz, S.R. Hallett, Prediction of impact damage in composite plates, Compos. Sci. Technol. 60 (2000) 273–281. doi:10.1016/S0266-3538(99)00126-8.

[57] J.P. Hou, N. Petrinic, C. Ruiz, A delamination criterion for laminated composites under low-velocity impact, Compos. Sci. Technol. 61 (2001) 2069–2074. doi:10.1016/S0266-3538(01)00128-2.

[58] C. Bouvet, B. Castanié, M. Bizeul, J.-J. Barrau, Low velocity impact modelling in laminate composite panels with discrete interface elements, Int. J. Solids Struct. 46 (2009) 2809–2821. doi:10.1016/j.ijsolstr.2009.03.010.

[59] Y. Shi, T. Swait, C. Soutis, Modelling damage evolution in composite laminates subjected to low velocity impact, Compos. Struct. 94 (2012) 2902–2913. doi:10.1016/j.compstruct.2012.03.039.

[60] L. Maio, E. Monaco, F. Ricci, L. Lecce, Simulation of low velocity impact on composite laminates with progressive failure analysis, Compos. Struct. 103 (2013) 75–85. doi:10.1016/j.compstruct.2013.02.027.

[61] J. Xu, S. Silling, Peridynamic Analysis of Impact Damage in Composite Laminates, J. Aerosp. Eng. 21 (2008) 187–194. doi:10.1061/(ASCE)0893-1321(2008)21:3(187).

[62] T.C. Chu, W.F. Ranson, M.A. Sutton, Applications of digital-image-correlation techniques to experimental mechanics, Exp. Mech. 25 (1985) 232–244. doi:10.1007/BF02325092.

[63] F. Hild, S. Roux, Digital Image Correlation: from Displacement Measurement to Identification of Elastic Properties – a Review, Strain. 42 (2006) 69–80. doi:10.1111/j.1475-1305.2006.00258.x.

[64] S. Roux, J. Réthoré, F. Hild, Digital image correlation and fracture: an advanced technique for estimating stress intensity factors of 2D and 3D cracks, J. Phys. Appl. Phys. 42 (2009) 214004. doi:10.1088/0022-3727/42/21/214004.

[65] GOM Training Webinar - 2D Digital Image Correlation with GOM Correlate, 2016. https://www.youtube.com/watch?v=pGXuXg7dRlo.

[66] Y.D. Ha, F. Bobaru, Studies of dynamic crack propagation and crack branching with peridynamics, Int. J. Fract. 162 (2010) 229–244. doi:10.1007/s10704-010-9442-4.

[67] Y. Hu, Y. Yu, H. Wang, Peridynamic analytical method for progressive damage in notched composite laminates, Compos. Struct. 108 (2014) 801–810. doi:10.1016/j.compstruct.2013.10.018.

[68] M. Ghajari, L. Iannucci, P. Curtis, A peridynamic material model for the analysis of dynamic crack propagation in orthotropic media, Comput. Methods Appl. Mech. Eng. 276 (2014) 431–452. doi:10.1016/j.cma.2014.04.002.

[69] T. Jia, DEVELOPMENT AND APPLICATIONS OF NEW PERIDYNAMIC MODELS, Michigan State University, 2012.

[70] N. Liu, D. Liu, W. Zhou, Peridynamic modelling of impact damage in three-point bending beam with offset notch, Appl. Math. Mech. (2016) 1–12. doi:10.1007/s10483-017-2158-6.

[71] J.N. Reddy, Mechanics of Laminated Composite Plates and Shells: Theory and Analysis, Second Edition, CRC Press, 2004.

[72] D. Dipasquale, G. Sarego, M. Zaccariotto, U. Galvanetto, Dependence of crack paths on the orientation of regular 2D peridynamic grids, Eng. Fract. Mech. 160 (2016) 248–263. doi:10.1016/j.engfracmech.2016.03.022.

[73] K. Takahashi, K. Arakawa, Dependence of crack acceleration on the dynamic stress-intensity factor in polymers, Exp. Mech. 27 (1987) 195–199. doi:10.1007/BF02319474.

[74] A.S. Kobayashi, M. Ramulu, M.S. Dadkhah, K.-H. Yang, B.S.J. Kang, Dynamic fracture toughness, Int. J. Fract. 30 (1986) 275–285. doi:10.1007/BF00019707.

[75] J. Krafft, G. Irwin, Crack-Velocity Considerations, in: ASTM Committee E-24 (Ed.), Fract. Toughness Test. Its Appl., ASTM International, 100 Barr Harbor Drive, PO Box C700, West Conshohocken, PA 19428-2959, 1965: pp. 114-114–16. http://www.astm.org/doiLink.cgi?STP26587S (accessed April 13, 2016).

[76] A.S. Kobayashi, S. Mall, Dynamic fracture toughness of Homalite-100, Exp. Mech. 18 (1978) 11–18. doi:10.1007/BF02326552.

[77] W. Zhou, D. Liu, N. Liu, Analyzing dynamic fracture process in fiber-reinforced composite materials with a peridynamic model, Eng. Fract. Mech. 178 (2017) 60–76. doi:10.1016/j.engfracmech.2017.04.022.

[78] W. Zhou, and D. Liu, A Peridynamic Model for Analyzing Crack Propagation in Unidirectional Composite Lamina, Proc. Am. Soc. Compos. Thirty-First Tech. Conf. (2016).

[79] D. Hartman, M.E. Greenwood, D.M. Miller, High Strength Glass Fibers, agy, 2006.

[80] K. Rosario, D. Liu, Assessment of Quasi-Three-Dimensional Composites - with Discussions on Fiber Straining and Weaving Effectiveness, J. Compos. Mater. 44 (2010) 2953–2973. doi:10.1177/0021998310371538.

[81] C. Atas, D. Liu, Impact response of woven composites with small weaving angles, Int. J. Impact Eng. 35 (2008) 80–97. doi:10.1016/j.ijimpeng.2006.12.004.

[82] R. Jensen, A. Forster, C. Copeland, J. Dibelka, Cure Schedule Evaluation of SC15 and SC79 Low-Viscosity Epoxy VARTM Resins, Army Research Laboratory, 2005.

[83] Standard Test Method for Tensile Properties of Polymer Matrix Composite Materials, ASTM D3039, 17.

[84] H. Schreier, J.-J. Orteu, M.A. Sutton, Image Correlation for Shape, Motion and Deformation Measurements, Springer US, n.d. doi:10.1007/978-0-387-78747-3.